2021-08-20

The Electrochemistry of Ferrocenyl-thiolate Self-Assembled Monolayers for use in a Toll-like Receptor 4-based sensor

Singh, Raunak

UNIVERSITY OF CALGARY

The Electrochemistry of Ferrocenyl-thiolate Self-Assembled Monolayers for use in a Toll-like Receptor 4-based biosensor

by

Raunak Singh

A THESIS

SUBMITTED TO THE FACULTY OF GRADUATE STUDIES

IN PARTIAL FULFILMENT OF THE REQUIREMENTS FOR THE

DEGREE OF MASTER OF SCIENCE

GRADUATE PROGRAM IN CHEMISTRY

CALGARY, ALBERTA

AUGUST, 2021

Abstract

Detection of biological agents by traditional bench-top instrumentation is insufficient for purposes of real time on-site analysis, which is imperative for biodefense applications. Unlike radiological and chemical warfare agents, sophisticated detection systems have not yet been designed for immediate sensing of biological agents. Development of field-deployable biosensors is a response to fulfill this gap, specifically, the demand for immediate recognition of samples of unknown origin requiring broad-based detection capabilities. Our research group has been pursuing this venture by creating an electrochemical biosensor that is able to detect the bacterial endotoxin, lipopolysaccharide (LPS), produced by gram negative bacteria. Our biosensor utilizes Toll-like Receptor 4 (TLR4) immunoproteins as the biorecognition element. These immunoproteins are surface immobilized via ternary alkanethiolate self-assembled monolayers (SAMs) deposited on polycrystalline Au surfaces. These SAMs possess a uniquely low interfacial resistance (≤ 1 kΩ) due to the presence of a Ferrocenyl-thiolate component, which mediates electron transfer from dissolved $Fe(CN)_6^{4-}$ to the underlying Au substrate.

The work presented in this thesis focuses on the problem, and its subsequent solution, encountered with the SAM electrochemistry portion of the TLR4 sensor assembly. The issue was initially detected by false positive responses of the sensor in the absence of LPS-containing bacterial lysate, exhibiting an increase in resistance of similar intensity in both the absence and presence of heat-killed Salmonella typhimurium (HKST) bacterial lysate. The primary cause of the TLR4 sensor drift was determined here to be the instability of the Fc^+ group, which is generated repeatedly during the mediation of the $Fe(CN)_6^{4-}$ oxidation process. This is consistent with past literature that alluded to the irreversible redox deactivation of the Fc^+ group under non-optimal conditions. This problem was remedied in this work by replacing phosphate ions from the buffer

solution by perchlorate, but as proteins such as TLR4 should be kept in neutral conditions, another solution was sought. This involved replacing the original Fc-thiol molecule (i.e., 11-mercaptodecyl-ferrocenylcarboxamide (Fc-amide)) with 11-(ferrocenyl)undecanethiol (FcC_{11}).

These novel ternary SAMs containing the stable FcC_{11} component were then used to prepare a new generation of TLR4-based sensors, which showed negligible drift and were able to reliably detect LPS from 0.0128 to 5000 µg/mL. This demonstrates that utilizing Fc-thiolate SAMs is now a viable method to prepare low-resistance biosensors for use as field-deployable systems.

Acknowledgments

Foremostly, I would like to acknowledge my supervisor, Dr. Viola Birss. I am grateful to Dr. Birss for providing me the opportunity to participate in this research project and be a part of her research group. Dr. Birss has mentored me not only in the principles of electrochemistry but also mentored me into becoming a more fully-rounded scientist than I was previously. Thank you for your contribution to my scientific development

I would also like to acknowledge my supervisory committee, Dr. Justin MacCallum and Dr. Todd Sutherland, who provided unique insight during annual meetings. I would also add to this list my thesis examiner, Dr. Roland Roesler, and thesis chair, Dr. Hans Osthoff.

I would like to express my exceptional gratitude to a former post-doctoral fellow of the Birss group, Dr. Armando Marenco, as he assisted me the most through all of my thesis work. Moreover, he was instrumental in pushing me to be truthful and professional during my graduate studies and thesis work.

The experiments and data interpretation included in the appendix of this thesis were done in collaboration with Dr. Justin MacCallum and Dr. Margaret Renaud-Young. I appreciate the encouragement and patience that was shown by the aforementioned despite the fact that those experiments were not considered a success. Two other collaborators that deserve recognition are Dr. Stephen Creager from Clemson University and Dr. Nora Chan from Defense Research and Development Canada. The former provided a valuable reagent that was utilized heavily in this work, and provided insights into electrochemical mediation and stability of Fc/Fc^{+}, whereas the latter provided both the impetus and inspiration for one of the potential applications of this work. I would also like to acknowledge Dr. Robert Mayall whose research was the major inspiration behind my own work.

There are numerous former and current members of the Birss group that I want to thank for their help. This list of names includes Dr. Tao Wang, April Woods, Dr. Lin Qi, Christine Li, Dr. Marwa Atwa, Milad Shamsi, Dr. Manila Valappil and Samantha Luong. I would especially like to thank Scott Paulson, as I have always appreciated his insights on this project and critical thinking ability in general. I would also like to thank Vladimir Kabanov from the Heyne group, as he is a close friend and confidant.

Some additional people I would like to acknowledge are certain undergraduate professors. Dr. Thomas G. Back and Dr. Arvi Rauk gave me my first position in research despite my subpar GPA, which helped me change the trajectory of my future grades. Dr. Simon Trudel supervised me through my first major research project to fulfill the requirements for my undergraduate degree and initially taught me much of what I now know about alkanethiolate SAMs. Dr. Wenyuan Liao and Dr. Thi Dinh made me appreciate and realize the utility of mathematics in research.

Financial assistance was provided from the Natural Sciences and Engineering Research Council of Canada (NSERC) through a Discovery Grant to Dr. Birss, as well as from the Defense Research and Development Council of Canada (DRDC). I also wanted to thank Mark Toonen (Glass shop), Janice Crawford and Jackie Hunt, along with the rest of the Chemistry Department support staff members, for their help and support over the years.

Finally, I would like to thank the Alberta Cerebral Palsy Sports Association and the East Memorial Football Club, as I believe that my work with these organizations have been the most meaningful and impactful work in my life as of yet, which helped to keep me mentally and emotionally focused during the second half of my thesis work. Members of the aforementioned community have been nothing but kind and inspiring. I want to also acknowledge the person I emulate and have aspired to be like the most, Cus D'Amato, who despite being a high school

dropout, is the most intelligent person whose ideas I have come across. The strongest forces in my life have been my mother and father, and God, whose contributions are immeasurable and any words to describe their contributions are insufficient.

Table of Contents

Abstract ii
Acknowledgments iv
Table of Contents vii
List of Tables x
List of Figures xi
List of Schemes xvi
List of Greek Symbols xvii
List of Symbols xviii
List of Abbreviations and Nomenclature xx

1 Introduction 1
1.1 The use of biosensors for biodefense applications 1
1.2 Research Objectives 4
1.3 Outline of thesis 5

2 Relevant Background 7
2.1 Biosensors 7
2.2 Lipopolysaccharides and its binding interaction with Toll-like Receptor 4 immunoprotein 9
2.2.1 Gram-negative bacteria and lipopolysaccharide 9
2.2.2 Toll-like Receptor 4 and its interaction with lipopolysaccharide 10
2.3 Electrochemical biosensor design 12
2.3.1 Alkanethiolate self-assembled monolayers 12
2.3.2 Protein immobilization methods 15
2.4 Electrochemical Toll-like Receptor-based biosensors using SAMs 17
2.4.1 TLR3-based biosensors 18
2.4.2 TLR5-based biosensors 19
2.4.3 TLR2-, TLR2/1-, TLR2/6-based biosensors 20
2.4.4 TLR4-based biosensors 21
2.5 Electrochemistry of alkanethiolate SAMs containing Ferrocenyl-thiolates 23
2.5.1 Effects of various Fc populations and interactions during SAM formation on CV response 24
2.5.2 Standard heterogeneous electron-transfer kinetics of Fc-thiolate SAMs 27
2.5.3 Effect of terminal group of diluent thiolates on the thermodynamics and kinetics of Fc-based SAM electrochemistry 28
2.6 Electrochemical Techniques 30
2.6.1 Cyclic voltammetry 30
2.6.2 Electrochemical impedance spectroscopy 33

3 Experimental Methods 37
3.1 Chemicals 37
3.2 Preparation and cleaning of electrodes 38
3.2.1 Au working electrodes 38
3.2.2 Pt mesh counter electrodes 40
3.2.3 Reference electrodes 40

3.3 Deposition of self-assembled monolayers (SAMs) 40
3.4 Sensor construction 41
3.4.1 Sensors prepared using carboxylic-acid containing SAMs 41
3.4.2 Sensors prepared using nitrilotriacetic-acid containing SAMs 42
3.5 Electrochemical methods 43
3.5.1 Electrodes 43
3.5.2 Electrochemical cell 44
3.5.3 Electrochemical instrumentation 44
3.5.4 Experimental conditions 45
3.5.4.1 EIS studies of the WE 45
3.5.4.2 Exposure of sensors to biological species 46
3.5.4.3 Electrochemistry of Ferrocenyl-thiolate self-assembled monolayers 46
3.5.4.4 Electrochemical mediation CV experiments 46
3.6 Error Analysis 47

4 Sensor construction, testing protocols and characteristics of sensor drift 48
4.1 Introduction to TLR-based sensors constructed from Ferrocenyl-thiolate self-assembled monolayers 48
4.1.1 Composition of ternary SAMs 48
4.1.2 Electrochemical testing protocol 50
4.2 Comparison of magnitude of electrochemical response to HKST lysate cells and magnitude of drift of TLR4-based sensors using EIS and mediated CV 57
4.3 Relationship between CV charge and double layer capacitance of Ferrocenyl-thiolate SAMs and signal drift 60
4.3.1 Drift of Ferrocenyl-thiolate SAM electrochemistry in $Fe(CN)_6^{4-}$ solution 60
4.3.2 Drift of Ferrocenyl-thiolate SAM electrochemistry in PB solution 62
4.4 Effect of TCEP on electrochemistry of ternary Fc-amide SAM prepared from fresh vs. aged thiol solutions 66
4.5 Effect of Fc-amide thiol content within the SAM on drift of ternary Ferrocenyl-thiolate SAM electrochemistry 70
4.6 Effect of ferro/ferricyanide on drift of ternary Ferrocenyl-thiolate SAM electrochemistry 75
4.7 Effect of time of open-circuit exposure of the ternary Ferrocenyl-thiolate SAMs to the testing solution 78
4.8 Summary 80

5 Overcoming loss of Ferrocenyl-thiolate SAM electrochemistry 82
5.1 Strategies employed to curtail Fc/Fc^+ redox deactivation 82
5.2 Stabilization of Fc/Fc^+ CV activity in $NaClO_4$ solutions 87
5.3 Fc/Fc^+ activity of Fc-amide binary thiolate SAMs 90
5.3.1 First few cycles of CV response of Fc-amide binary SAMs in perchlorate solutions 90
5.3.2 First few cycles of CV response of Fc-amide binary SAMs in PB solution 95
5.3.3 Stability of EIS response of binary Fc-amide SAMs 98
5.4 Stability of immobilized-Fc of ternary Fc-amide vs. ternary FcC_{11} SAMs in PB solution 101
5.5 TLR4-based sensor prepared using ternary FcC_{11} SAMs 106

5.6 Summary.....108

6 Conclusions and future directions.....110
6.1 Conclusions.....110
6.2 Future directions.....112

References.....115

List of Tables

Table 4.1: Magnitude of EIS and CV signal change of a fully assembled TLR4 sensor when exposed to 10^5 HKST cells/mL from literature data (1st column [1]) and from the current work (2nd column). The 3rd and 4th columns show the magnitude of signal drift over 120 min for the TLR-4 sensor in 0 HKST cells/ml and for the ternary Fc-amide SAMs alone, respectively. 60

Table 4.2: Change in Fc surface coverage and double layer capacitance obtained for ternary Fc-amide SAMs (N = 3) in 0.2 M PB (pH 7.0) solution, before and after electrochemical testing (EIS and CV) in 5 mM $K_4Fe(CN)_6$ + 0.2 M PB (pH 7.0). Example CVs from which these values are obtained are shown in Figure 4.9. 65

Table 4.3: Composition of ethanolic thiol solutions used to prepared Fc-amide SAMs electrochemically tested in Section 4.5. 70

Table 4.4: The $\%\Delta R_{CT}$ measured from Nyquist plots shown in Figure 4.13, and the $\%\Delta C$ and $\Delta\Gamma_{Fc}$ values measured from the CVs shown in Figure 4.12 and Figure 4.14, for ternary SAMs with increasing surface coverage of Fc-amide. 75

Table 4.5: Electrochemical testing regime of SAMs in 5 mM $Fe(CN)_6^{4-}$ + 0.2 M PB (pH 7.00) (see Figure 4.17). 79

Table 5.1: Peak potential (1st data column), peak width (2nd data column), and double-layer capacitance (3rd data column) of ternary Fc-amide SAMs measured using CVs obtained at 500 mV/s in different solutions. 89

Table 5.2: Typical composition of ethanolic thiol solutions used to prepare binary Fc-amide SAMs tested electrochemically in Section 5.3. 92

Table 5.3: Fc surface coverage (Γ_{Fc}, 1st column), CV peak width (ΔE_{fwhm}, 2nd column), CV peak potential (E_p, 3rd column) and double layer capacitance values (C_{dl}, 4th column) obtained at 0.1 V for MUO/Fc-amide, MUA/Fc-amide, and DDT/Fc-amide binary SAMs from a single (early) CV scan. 94

Table 5.4: CV peak potential (E_p, 1st column) obtained for MUO/Fc-amide, MUA/Fc-amide, and DDT/Fc-amide binary SAMs and respective potential at which EIS data are collected (E_{EIS}) from a single (early) CV scan .* 98

Table 5.5: Charge-transfer resistance and its drift of Fc-amide binary and ternary SAMs in 120 min in PB solution 100

Table 5.6: Fc surface coverage (1st column), peak width (2nd column), double-layer capacitance measured at -0.1 V (3rd column) and peak potential (4th column) of ternary Fc-amide and FcC_{11} SAMs in 0.2 M PB (pH 7.0) solutions.* 104

Table A.1: Dissociation constants obtained from sigmoidal curve fits of the data shown in Figure A.1. Experimental conditions are given in the figure caption. 132

List of Figures

Figure 2.1: Two components of a typical biosensor, the biological element interacting with the analyte (red star) and the transducer to generate an electrical signal (gold sphere). 7

Figure 2.2: (a) Cartoon of SAMs defined by their head group (blue sphere) that forms a bond with the substrate (black rectangle), and the alkyl chain (grey line) that connects it with the terminal group (red sphere) at the interface. (b) Diagram of thiolate SAMs where the all-trans alkane chains are tilted at a certain angle from the normal of the substrate. 14

Figure 2.3: Representative schematic of electrochemical biosensors prepared by the immobilization of TLR4 (black horseshoe shape) on thiolate SAMs. This sensor operates using a blocking mechanism, as in the presence of LPS (red sphere), TLR4 dimerizes and restricts access of electrolyte ions (R) to the Au substrate. 18

Figure 2.4: Cartoons showing the measurable characteristics from a CV of a Fc-thiolate SAM. In panel a, grey areas represent the Faradaic charge of the oxidation/reduction of Fc/Fc^{+}, with the blue markers showing the respective peak potentials. Panel b shows a close-up of the anodic scan from panel a, where the blue double-sided arrow gives the maximum current of the Faradaic peaks, and the green double-side arrow is the full width at half-maximum (i.e., peak width)..... 24

Figure 2.5: Binary SAMs composed of $HS(CH_2)_{12}Fc$ and $HS(CH_2)_9CH_3$ distributed as a) partially clustered domains and b) mixed SAMs. 26

Figure 2.6***:*** Typical reversible surface-confined and mediation CVs, and Tafel plot shown in panels a, b, and c, respectively. The WE was sputtered Au, coated with a Fc-containing thiolate SAM. The CVs in panel a and b were collected in 0.2 M PB (pH 7.0) and 5 mM $K_4[Fe(CN)_6]$ + 0.2 M PB (pH 7.0), respectively. The Tafel plot in panel c was extracted from the anodic scan of the mediation CV in panel b and the Tafel slope was obtained from the linear fit of the plot. More details are provided in captions of Figure 4.2a, Figure 4.3a and b, respectively. 31

Figure 2.7: A simplified schematic of electrochemical rectification between immobilized Ferrocenyl-thiolate SAMs and ferrocyanide in solution under anodic bias (on the left) and cathodic bias (on the right). The dotted line represents the substrate-solution interface..... 32

Figure 2.8: Panel (a) shows the out-of-phase sinusoidal waves of the applied potential and the resulting current response, where φ is the phase shift between them. Panel (b) shows the in-phase sinusoidal waves of applied potential and current response, and the corresponding impedance calculated using Ohm's law. Panel (c) shows the impedance plotted as a two-dimensional vector with the length of the vector corresponding to its magnitude and the angle from the x-axis corresponding to the phase angle. The x-axis and y-axis projections of impedance are the real and imaginary impedance, respectively. . 35

Figure 2.9: Panel (a) shows a cartoon of a Nyquist plot containing a single arc and a Warburg impedance element, showing how the solution (R_s) and charge-transfer resistance (R_{CT}) are obtained from the Z' values, and the double-layer capacitance (C_{dl}) from the frequency (f) at the top of the arc, assuming that the electrochemical process occurring at the WE interface is modeled as a Randles circuit. The Randles circuit is shown in panel (b). In this circuit, the Warburg element (W) accounts for the 45^o linear portion of the Nyquist plot encountered at low frequencies. 35

Figure 3.1: Schematic of the sensor construction process used for TLR4 immunoprotein immobilization on ternary SAMs (5 % (v/v) 1 mM Fc-amide, 30 % (v/v) 1 mM MUA, and 65 % (v/v) 1 mM MUO) in Chapter 4. In this process, carbodiimide activated carboxylic acid was used to covalently attach an NHS leaving group, which departed in the presence of NTA-lysine that chelated Ni^{2+}, which, in turn, formed an ionic bond with the poly-Histidine Tag of the protein. Charge-compensating anions in the proximity of Ni^{2+} are not shown for sake of simplicity. 42

Figure 3.2: Schematic of the sensor construction process used for TLR4 immunoprotein immobilization on ternary SAMs (5 % (v/v) 1 mM FcC_{11}, 30 % (v/v) NTA-thiol and 65 % (v/v) 1 mM MUO) in Chapter 5. In this process, the terminal NTA group chelated Ni^{2+}, which formed an ionic bond with the poly-Histidine Tag of the protein. Charge-compensating anions in the proximity of Ni^{2+} are not shown for sake of simplicity. 43

Figure 3.3: The two-compartment cell used for electrochemical cleaning of electrodes is shown in panel (a) and the single compartment electrochemical cell used for sensor testing is shown in panel (b). 45

Figure 4.1: Cartoon of ternary Fc-amide SAMs composed of 11-mercaptoundecanoic (MUA), 11-mercaptoundecanol (MUO), and (10-mercapto-N-decyl)ferrocenecarboxamide (Fc-amide). 49

Figure 4.2: (a) CV scan of ternary Fc-amide SAMs in 0.2 M PB (pH 7.0) at 100 mV/s. The horizontal grey line from 0.2 – 0.6 V is the anodic and cathodic baseline (generated artificially using graphing software Origin) used to calculate the integrated Faradaic charge (black area) of the oxidation of Fc to Fc^+ (Q_{an}) and the reverse reduction reaction, respectively. The red lines at ~ 0.4 V are the anodic ($E_{p,\ anodic}$) and cathodic ($E_{p,\ cathodic}$) peak potentials of the oxidation and reduction reactions, respectively. The green arrow at 0.300 V is the polarization potential at which EIS is performed (E_{EIS}). The blue arrow at 0.100 V indicates the potential at which the double-layer current of the SAMs was measured before oxidation of Fc. In (b), a close up of the anodic peak of the sample CV in (a) is shown. 52

Figure 4.3**:** Mediation electrochemistry of ternary Fc-amide SAMs. In (a), a sample CV of the SAM in 5 mM $K_4[Fe(CN)_6]$ and 0.2 M PB (pH 7.0) at 100 mV/s is shown, where the mediation CV peak potential ($E_{p,a}$, ~0.4 V) and peak current density ($j_{p,a}$) is shown using the black arrow. EIS is performed negatively of the peak potential at the "foot" of the mediation CV at 0.300 V. In (b), the Tafel plot (black) extracted from the sample CV in (a) and the slope of its linear fit (grey) are shown. 54

Figure 4.4: Nyquist plot of ternary Fc-amide SAMs with data collected at 0.300 V and frequencies ranging from 1 MHz to 0.1 Hz in 5 mM $K_4[Fe(CN)_6]$ + 0.2 M PB solution (pH 7.0). The diameter of the semicircle at high frequencies gives R_{CT} (red) and the 45° line (blue box) at low frequencies is due to the Warburg impedance. 55

Figure 4.5: Electrochemical signal response of a TLR4-based sensor baseline (black) to 10^0-10^4 HKST cells/mL (grey) and 10^5 HKST (red) lysate cells/mL. Increasing concentrations of HKST were added every 20 min for 120 min to the solution containing 5 mM $K_4[Fe(CN)_6]$ + 0.2 M PB (pH 7.0). In (a), the Nyquist plots were collected at 0.300 V at frequencies ranging from 1 MHz to 0.1 Hz. In (b), the mediation CVs wave collected at 100 mV/s following EIS testing. 58

Figure 4.6: Electrochemical drift of a TLR4-based sensor at t = 0 min (black), 20 – 100 min (grey) and 120 min (red). Aliquots of the PB solution (i.e., solutions not containing HKST lysate cells) were added as a control test every 20 min for 120 min to the solution containing 5 mM $K_4[Fe(CN)_6]$ + 0.2 M PB (pH 7.0). In (a), the Nyquist plots were collected at 0.300 V at frequencies ranging from 1 MHz to 0.1 Hz. In (b), the mediation CVs were collected at 100 mV/s following each EIS experiment shown in (a). 59

Figure 4.7: Electrochemical drift of ternary Fc-amide SAMs (no TLR-4 attached), where the black, grey, and red traces are at 0, 20-100 min, and 120 min, respectively, in 5 mM $Fe(CN)_6^{4-}$ + 0.2 M PB (pH 7.0). (a) Nyquist plots were collected at 0.300 V from 1 MHz to 0.1 Hz and (b) shows the mediation CVs (100 mV/s) that followed each EIS test in (a). 61

Figure 4.8: (a) CVs of Fc-amide ternary SAMs collected in 0.2 M PB (pH 7.0) before the collection of EIS and CV data in $K_4Fe(CN)_6$ + 0.2 M PB (pH 7.0). These CVs were collected at 100 (black), 250 (grey) and 500 (light grey) mV/s. In (b), the double-layer current measured at 0.1 V from the CVs in (a) is displayed vs. sweep rate. The linear fit and R^2 values are shown in red. 62

Figure 4.9: Typical CVs (500 mV/s) of ternary Fc-amide SAMs in 0.2 M PB (pH 7.0), collected before (black) and after (red) electrochemical testing in 5 mM $K_4Fe(CN)_6$ + 0.2 M PB (pH 7.0)..... 64

Figure 4.10: Electrochemical response of ternary Fc-amide SAMs in 0.2 M PB (pH 7.0), prepared from thiol solutions that were freshly prepared (black) or stored for 1, 2, 3, 4, 6, 9, (grey) and 19 weeks (red) in a 4 ^{0}C refrigerator. In (a), CVs of an example set of SAMs at 500 mV/s are shown, while (b) gives the capacitance values at 0.1 V (N = 3 , except for storage time of 19 weeks). 68

Figure 4.11: Cyclic voltammograms at 500 mV/s of ternary Fc-amide SAMs, collected in 0.2 M PB (pH 7.0), prepared from freshly prepared thiol ethanolic solutions using regular deposition (black trace) and deposition in the presence of TCEP (blue). 69

Figure 4.12: Cyclic voltammograms of nominally 1 % (black), 2 % (dark grey), 5 % (grey), and 20 % (light grey) Fc-amide SAMs (Table 4.3) at 500 mV/s in 0.2 M PB (pH 7.0), prepared from stored thiol solutions using solutions containing TCEP. 71

Figure 4.13: Electrochemical response of ternary (a) 1 %, (b) 2 %, (c) 5 %, and (d) 20 % Fc-amide SAMs at t = 0 min (black), showing the drift after 20 - 100 min (grey) and after 120 min (red) in 5 mM $K_4[Fe(CN)_6]$ + 0.2 M PB (pH 7.0). Data were collected every 20 min at 0.300 V from 1 MHz to 0.1 Hz. 74

Figure 4.14: Cyclic voltammograms of 1 % (black), 2 % (dark grey), 5 % (grey), and 20 % (light grey) ternary Fc-amide SAMs at 500 mV/s in 0.2 M PB (pH 7.0) after electrochemical testing in 5 mM $K_4Fe(CN)_6$ + 0.2 M PB (pH 7.0). 75

Figure 4.15: Electrochemical response of ternary Fc-amide SAMs at t = 0 min (black), after 20 - 100 min (grey), and after 120 min (red) of testing in 5 mM $K_4[Fe(CN)_6]$ + 0.2 M PB (pH 7.0) + (a) 0 mM, (b) 5 mM, (c) 25 mM, and (d) 50 mM $K_3[Fe(CN)_6]$. The EIS data were collected at 0.300 V from 1 MHz to 0.1 Hz. The $\%\Delta R_{CT}$ experienced by these SAMs is 44 %, 54 %, 62 % and 81 % respectively. 77

Figure 4.16: Mediation CVs of ternary Fc-amide SAMs at t = 0 min collected in 5 mM $K_4[Fe(CN)_6]$ + 0.2 M PB (pH 7.0) + (a) 0 mM, (b) 5 mM, (c) 25 mM, and (d) 50 mM $K_3[Fe(CN)_6]$. at 500 mV/s. 78

Figure 4.17: Electrochemical response of ternary Fc-amide SAMs collected in the 1st (black), in the 2nd - 6th (grey), and in the 7th measurement (red) in 5 mM $K_4[Fe(CN)_6]$ + 0.2 M PB (pH 7.0). EIS data were collected (a) seven times consecutively, (b) every 20 min for 120 min, or (c) every 60 min for 360 min. 80

Figure 5.1: CV responses of ternary Fc-amide SAMs (5 % (v/v) 1 mM Fc-amide, 30 % (v/v) 1 mM MUA and 65 % (v/v) 1 mM MUO) collected at t = 0 min (black), 20, 40, 60, 80, and 100 min (light grey), and at t = 120 min (red) in (a) 0.2 M PB (pH 7.0) and (b) 1 M $NaClO_4$ solutions, all at 500 mV/s. 88

Figure 5.2: Change in Fc/Fc^+ CV peak charge of the same SAMs calculated from CVs collected in different electrolytes over a period of 120 min. The peak charge is assumed to be indicative of the surface coverage of the Fc-amides present in these ternary SAMs. SAMs with a larger negative $\%\Delta\Gamma_{Fc}$ undergo greater drift as compared to SAMs with a smaller $\%\Delta\Gamma_{Fc}$. 89

Figure 5.3: Fc-amide binary SAMs with a) 11-mercaptoundecanol (MUO), b) 11-mercaptoundecanoic acid (MUA), and c) 1-dodecanethiol (DDT) as the diluent SAM. 91

Figure 5.4: A single (early) CV scan of MUO/Fc-amide (black trace), MUA/Fc-amide (red trace) and DDT/Fc-amide (blue trace) binary SAMs collected at 500 mV/s in 1 M $HClO_4$. The Fc thiol surface coverage of these SAMs is estimated as ~1 % (calculated from the CV peak charge). 93

Figure 5.5: A single (early) CV scan of MUO/Fc-amide (black trace), MUA/Fc-amide (red trace) and DDT/Fc-amide (blue trace) binary SAMs collected at 500 mV/s in 0.2 M PB (pH 7.0). These SAMs are prepared using the same respective solution compositions as the Section 5.3.1. 95

Figure 5.6: Peak potential values (N = 3) of MUO/Fc-amide (black) and MUA/Fc-amide binary SAMs taken from the first CV scan collected in 0.2 M PB at pH 6.0, 6.5, 7.0, 7.5 and 8.2. 98

Figure 5.7: EIS response of binary (a) MUO/Fc-amide, (b) MUA/Fc-amide, and (c) DDT/Fc-amide binary SAMs at t = 0 min (black dashed line), drift after 20 - 100 min (grey) and 120 min (black (MUO), red (MUA), and blue (DDT) solid lines) in 5 mM $K_4Fe(CN)_6$ + 0.2 M PB. Data collected every 20 min at 0.375, 0.255, and 0.435 V, respectively, from 1 MHz to 0.1 Hz. 100

Figure 5.8: Ternary Fc-thiolate SAMs composed of (a) MUA, MUO and Fc-amide, and (b) MUA, MUO and FcC_{11} thiols. 101

Figure 5.9: CV comparison of ternary Fc-amide (red) and FcC_{11} (green) SAMs collected at 500 mV/s in 0.2 M PB (pH 7.0). 103

Figure 5.10: Electrochemical response of ternary (a) Fc-amide and (b) FcC_{11} SAMs at t = 0 min (black), 20-100 min (grey), and 120 min (for both Fc-amide (red) and FcC_{11} (green)) collected in 0.2 M PB (pH 7.0) at 500 mV/s. 105

Figure 5.11: Ternary FcC_{11} SAMs composed of 11-(Ferrocenyl)undecanethiol (FcC_{11}), N-[N_α,N_α-Bis(carboxymethyl)-L-lysine]-12-mercaptododecanamide (NTA-thiol) and 11-mercaptoundecanol (MUO). 107

Figure 5.12: Electrochemical signal of a TLR4-based sensor in 5 mM $K_4[Fe(CN)_6]$ + 0.2 M PB (pH 7.0) collected at 0.200 V vs. Ag/AgCl at frequencies ranging from 1 MHz to 0.1 Hz. In (a), drift of this sensor was measured every 20 min from t = 0 (black trace) to 60 min (red trace). In (b), the response is measured prior to the addition of LPS to the surface of the electrode (baseline, black trace) and after the addition of up to a maximum concentration of 5 mg/mL LPS (green trace). 108

Figure A.1: (a) Emission intensity and (b) changes in emission intensity after 20 s IR-Laser irradiation gathered from three independent experiments and the sigmoidal curve fit of the fluorophore-tagged TLR4/MD-2 (black) and fluorophore (blue) interaction with LPS. Measurements were collected after 1 h incubation of LPS with either 10 nM TLR4/MD-2 and 5 nM dye or 5 nM dye at T = 25 ^oC. 131

List of Schemes

Scheme 2.1: Protonation states of chelating agent Nitrilotriacetic acid (NTA). The pK_a values were taken from ref [97]. 17

Scheme 2.2: Protonation states of Histidine amino acid. The pK_a values were taken from ref [98]. 17

Scheme 5.1: Proposed mechanism of (a) acid- and (b) base-catalyzed hydrolysis of Fc-amide.106

List of Greek Symbols

Symbol	Value	Units	Definition
α			Transfer coefficient
α_a			Transfer coefficient of the anodic reaction
α_c			Transfer coefficient of the cathodic reaction
β	0.5		Symmetry factor
ε_0	8.85×10^{-12}	F m^{-1}	Permittivity of free space
ε_r		F m^{-1}	Permittivity of SAMs
Γ_{Fc}		mol cm^{-2}	Fc-thiolate surface coverage
γ			Number of electrons transferred prior to the rate-determining step
η			Overpotential
ν		mV/s	Sweep rate
ν			Stoichiometry of the rate-determining step
φ			Phase angle

List of Symbols

Symbol	Value	Units	Definition
$\%\Delta C_{dl}$			% Change in double-layer capacitance
$\%\Delta E_{p,a}$			% Change in peak anodic potential
$\%\Delta i_{p,a}$			% Change in peak anodic current
$\%\Delta R_{CT}$			% Change in charge-transfer resistance
C_{dl}		$\mu F\ cm^{-2}$	Double layer capacitance
d			Thickness of SAM layer
$E^{0'}$			Formal potential
E_{EIS}		mV	Potential at which Electrochemical impedance spectroscopy data is collected
ΔE_p		mV	Difference between peak anodic and cathodic potential
$\Delta\Gamma_{Fc}$		$mol\ cm^{-2}$	Change in Fc surface coverage
E_p		mV	Average peak anodic and cathodic potential
$E_{p,a}$		mV	Peak anodic potential
$E_{p,c}$		mV	Peak cathodic potential
F	96485	$C\ mol^{-1}$	Faraday constant
i_{dl}			Double layer current
i_{net}			Net
i_0			Exchange current
i_p		µA	Peak current
$i_{p,a}$		µA	Peak anodic current
$i_{p.c}$		µA	Peak cathodic current
$j_{p,a}$		$\mu A\ cm^{-2}$	Peak anodic current density
$j_{p,c}$		$\mu A\ cm^{-2}$	Peak cathodic current density
K_a			Acid dissociation constant
N			Number of samples tested
pH			Negative base 10 logarithm of H+ activity
pK_a			Negative base 10 logarithm of acid dissociation constant
r			Number of electrons transferred during the rate-determining step
R	8.314	$J\ K^{-1}\ mol^{-1}$	Universal gas constant
R_{CT}		Ω	Charge transfer resistance
R_s		Ω	Solution resistance
S			Sulfur
t			Time
T		K	Temperature
Q		C	Integrated Faradaic charge
Q_{an}		C	Anodic integrated Faradaic charge
Q_{cat}		C	Cathodic integrated Faradaic charge
W			Warburg diffusion element

Z	Impedance
Z’	Real impedance
Z’’	Imaginary impedance

List of Abbreviations and Nomenclature

Symbol	Definition
AC	Alternating current
Ag/AgCl	Silver/Silver chloride electrode
bp	Base pairs
BWA	Biowarfare agents
CD14	Cluster of Differentiation 14
CE	Counter electrode
DDT	1-dodecanethiol
DMF	Dimethylformamide
DMSO	Dimethylsulfoxide
ECSA	Electrochemically active surface area
EDC	1-Ethyl-3-(3-dimethylaminopropyl)carbodiimide
EIS	Electrochemical impedance spectroscopy
EtOH	Ethanol
Fc	Ferrocene
Fc^+	Ferrocenium
Fc-amide	11-mercaptodecyl-ferrocenylcarboxamide
FcC_{11}	11-(ferrocenyl)undecanethiol
GLAD	Glancing angle deposition
H_{ab}	Electronic coupling of donor-acceptor systems
His	Histidine amino acid
HKST	Heat-killed *salmonella typhimurium*
IUPAC	International Union of Pure and Applied Chemistry
k^0	Standard rate constant of electron transfer
KCl	Potassium chloride
λ	Reorganization energy
LBP	Lipopolysaccharide-binding protein
LIDAR	Light Detection and Ranging
Lip-NHS	Lipoic N-hydroxysuccinimide ester
LOD	Limit of detection
LPS	Lipopolysaccharide
MD-2	Myeloid Differentiation Factor-2
MES	2-(N-morpholino) ethanesulfonic acid
MPA	3-mercaptopropionic acid
MPCs	Monolayer Protected Clusters
MUA	11-mercaptoundecanoic acid
MUO	11-mercaptoundecanol
NATO	North Atlantic Treaty Organization
NHS	N-hydroxysuccinimide ester
NTA	Nitrilotriacetic acid
OCP	Open circuit potential
Pam2CSK4	Synthetic diacylated lipopeptide

Pam3CSK4	Synthetic triacylated lipopeptide
PAMPs	Pathogen-Associated Molecular Patterns
PB	Phosphate buffer
PEG	Poly(ethylene glycol)
poly I:C	Polyinosinic-polycytidylic acid
PRRs	Pattern Recognition Receptors
R&D	Research and Development
RDS	Rate-determining step
RHE	Reversible hydrogen electrode
RE	Reference electrode
SAM	Self-Assembled Monolayer
TCEP	Tris(2-carboxyethyl)phosphine
TEG	Tri(ethylene glycol)
TLR	Toll-like Receptor
T.S.	Tafel slope
UVAPS	Ultraviolet Aerodynamic Particle Size Spectrometry
vdW	van der Waals
WE	Working electrode

Chapter One: Introduction

1.1 The use of biosensors for biodefense applications

The potential applications of biosensors span the fields of medicine (*in vivo* and *in vitro*), agriculture and biodefense [1]. The overall purpose of this project, pursued by the Birss group, was to design a biosensor for biodefense applications. Biowarfare agents (BWA) are one of four hazards that comprise a subset of military threats, referred to as non-conventional, with the remaining hazards being chemical, radiological, and nuclear [2]. Conventional threats (such as hijackings, bombings etc.) were considered non-conventional a few decades ago, and defense experts pre-emptively fear that current non-conventional threats may follow a similar path as in becoming more prevalent in the near future.

Despite signing of the Biological Weapons Convention (that prohibits development, production, and stockpiling of BWA) by 183 countries, defense experts forecast biological threats being at the forefront of non-conventional threats for three primary reasons. Firstly, countries such as Iran, Iraq, Israel, Libya, Syria, China, North Korea and Taiwan have undeclared offensive biological warfare programs [3]. Secondly, experts from the North Atlantic Treaty Organization report that the estimated cost of an attack normalized to civilian population area affected is $ 1 /km^2, $ 600 /km^2, and $ 800 /km^2, respectively for biological, chemical, and nuclear weapons, making biological threats the least expensive to dispense [4]. Thirdly, BWAs are invisible, odorless, tasteless, and have an incubation period (time prior to appearance of symptoms) that allows the multiplication and subsequent spread of pathogens to victims not present at the original site of attack/BWAs dispersal [3,5,6]. Thus, the main impetus of this project, funded by the Department of Defense, has been to design a biosensor for this application.

The dispersal of either liquid or dry BWA powder aerosols is historically how such attacks are carried out [7,8]. This is partly because 1-10 μm sized aerosolized particles penetrate the nasal cavity and deposit within the lungs, with the onset of infection requiring deposition of small quantities of microbes (1-10000) [5,9]. The biological effect and detection of bioaerosols are both a function of factors other than the microorganism itself, including the physical characteristics of the aerosol (e.g., electric charge, size distribution, etc.), environmental conditions (e.g., temperature, humidity, etc.) and exposure (e.g., airborne concentration, volume inhaled, etc.) [7].

To combat this threat, the overall biodefense strategy for detection and identification of BWAs is typically divided into three 'layers' [6]. The first is the stand-off system with the capability of monitoring large areas for aerosols at long distances [6]. For example, Light Detection and Ranging (LIDAR) detects small aerosol particles 30-50 km away, but is unable to discriminate between biological and non-biological aerosols [10]. The second involves point detectors that monitor small suspect areas in close proximity and is where biosensors contribute to the overall biodefense strategy. The third layer requires epidemiological data that monitor the occurrence of infectious disease in certain populations [6].

Point detectors are categorized as either specific or broad. Specific detectors require *a priori* knowledge of BWAs, whereas broad detectors do not, making the latter significantly more useful for analyzing unknown samples. Techniques and/or instruments, such as polymerase chain reaction, mass spectrometry, flow cytometers, and immunoassays, are used for specific point detection. Similarly, cell cultures and particle sizers are used for broad point detection [6]. Cell cultures (in conjunction with an aerosol sampler) are currently the best method for BWA identification and comprise of growing the unknown biological sample in a controlled environment and then observing qualitative and quantitative properties via an optical microscope, thereby

enabling trained personnel to identify the BWA [9]. This process requires at least a few days, which is a longer time than is required for timely identification of certain BWAs. For example, *Bacillus anthracis*, a Gram-positive bacteria, is a known BWA that causes septic shock, respiratory distress, and eventual death within 24 h [11].

Ultraviolet Aerodynamic Particle Size Spectrometry (UVAPS), another broad detection method, counts aerosols with sizes ranging from 0.5 – 15 μm in real-time, but only discriminates between biological and non-biological material. However, UVAPS is unable to distinguish between intrinsic fluorescence emission of cells and organic interferents [12]. Biosensors potentially provide an alternative as broad detectors that detect rapidly but without responding to non-biological interferents. Biosensors, a subset of point detectors, can achieve this by utilizing an appropriate biomolecule that broadly detects a class of potential BWAs in an unknown sample using a sensitive technique that generates a signal rapidly. The primary merit of the use of biosensors (see Section 2.1) is the utilization of low-cost instrumentation that is both commercially available and miniaturized, giving ease of use and deployability, respectively. The primary limitation is that biosensors, compared to UVAPS and cell cultures, may require more elaborate sample preparation prior to use [6].

According to the Centers for Disease Control and Prevention, two of the seven highest priority BWAs and ten of the twenty second highest priority BWAs belong to a class of microorganisms called Gram-negative bacteria [13]. The Birss group has developed an electrochemical biosensor that detects Gram-negative bacteria (i.e., bacteria that does not retain the Gram stain) using Toll-like Receptor 4 immunoprotein [14,15]. The first iteration of the TLR4-based sensor developed by our group involved depositing organized alkanethiolate Self-Assembled Monolayers (SAMs) on planar polycrystalline Au, resulting in high interfacial

resistances (i.e., ~ 1 MΩ) [16]. At such low currents, noise, generated by static charge build up due to vibrations, electrostatic coupling to wires etc., becomes significant. This problem can be overcome by enclosing the electrochemical cell in a Faraday cage (i.e., grounded metal box that shields the materials inside from stray electromagnetic fields) [17], but this renders the sensor incapable of being field-deployable. Our group circumvented this issue by introducing a Ferrocenyl-thiolate component into the underlying monolayer, which amplifies the flow of current, causing the resistance of the sensor to decrease ≤ 1 kΩ. This amplification occurs by the oxidation of Fc to Fc^{+}, which subsequently catalyzes the oxidation of $Fe(CN)_6^{4-}$ present in the electrolyte. High currents allow for use of low cost potentiostats, open-source software, and field-deployable systems [18]. However, it was observed in this most recent generation of Fc-thiolate based TLR4 sensors that they were susceptible to drift, for reasons that were initially unclear. Thus, this thesis is focused on understanding and overcoming the electrochemical sensor drift, while continuing to use the Fc-thiolate system.

1.2 Research Objectives

The main objectives of the research presented in this thesis are as follows:

- To quantify the drift of Fc-thiolate SAM-based TLR-4 sensors to determine if the drift is sufficiently large that it would result in false positives (i.e., if the magnitude of the drift is comparable to that of signal generated in the presence of the desired ligand).
- To determine the source of the signal drift and understand its cause by varying the electrochemical testing parameters.

- To modify the sensor testing methods and/or construction/composition in order to minimize sensor drift, while also retaining the biological activity of the TLR4 immunoprotein attached to the surface.

1.3 Outline of thesis

This thesis is comprised of six chapters. In Chapter 1, the use of biosensors for biodefense applications is discussed along with the objectives of this thesis. Chapter two provides relevant background information, including on immunobiology, thiolate SAMs, TLR-based electrochemical biosensors, and electrochemical methods. Chapter three discusses the experimental details related to this thesis.

In Chapter four, TLR4-based sensors, prepared using Fc-thiolate SAMs, designed primarily by Dr. Robert Mayall, an earlier PhD student in the Birss group, were prepared and their response to heat-killed *Salmonella typhimurium* (HKST) lysate cells was replicated. It was determined that the sensor response to blank samples (i.e., sensor signal drift) and HKST lysate cells are comparable in magnitude, thus indicating a serious problem with sensor drift. With input from Dr. Armando Marenco, a recent PDF in the Birss group, sensor drift was found to correlate with the properties of the Fc-thiol component of the SAM, more specifically, with the loss of the electrochemical signal of the Fc group with time, caused when Fc is in its oxidized form (i.e., Fc^+), thus resulting in the gradual loss of its redox chemistry.

In Chapter five, three strategies were utilized to stabilize the electrochemical response of the surface-bound Fc/Fc^+ couple. In the first direction, the SAM electrochemistry was carried out in perchlorate solutions, rather than phosphate buffer, as the perchlorate anion is known to minimize the deactivation of Fc^+, although its ability to denature proteins remained a concern [19], with the phosphate ion being preferable. A second effort involved modulating the thiol SAM

terminal groups by altering the diluent thiols that surround the Fc terminal groups. However, this approach was not successful. A solution to the problem of drift was achieved by substituting the Fc-thiolate molecule, which contained an electron-withdrawing amide group, with one containing the electron-donating methyl group. At the end of Chapter five, preliminary successful sensor results, obtained with a TLR4-based sensor using this new ternary SAM, are shown, with these experiments carried out in collaboration with Dr. Armando Marenco.

In Chapter six, the conclusions of this thesis and recommended future directions for this project are summarized. This is followed by the references and an appendix that summarizes the attempts made as part of this thesis work to characterize the biophysical interactions between TLR4 and Lipopolysaccharides (LPS) using thermophoresis in the laboratory of Dr. Justin MacCallum.

Chapter Two: Relevant Background

2.1 Biosensors

The International Union of Pure and Applied Chemistry (IUPAC) defines biosensors as a subset of chemical sensors that operate via a biological mechanism to detect an analyte (also referred to as the ligand) in a sample [20]. In general, biosensors are composed of two components: the biological element and the transducer. The biological element interacts with the desired ligand to generate a physico-chemical response, which the transducer converts to an electrical signal. The electrical signal is then processed and displayed in a user-friendly interface by an analytical instrument [1,20,21]. The operating principle of a biosensor, and its components, are shown in Figure 2.1.

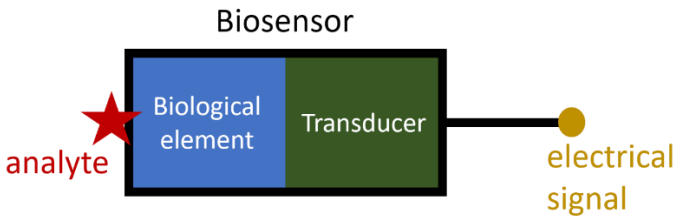

Figure 2.1: Two components of a typical biosensor, the biological element interacting with the analyte (red star) and the transducer to generate an electrical signal (gold sphere).

Biosensors can be broadly divided into four categories, based on the transducer component: mass, calorimetric, optical, and electrochemical biosensors. For example, mass biosensors monitor binding interactions between the ligand and its biological element, occurring on a piezoelectric substrate, as a change in the crystal's fundamental frequency [22]. This value is then used to calculate mass gained on the crystal substrate from the decrease in its frequency [23]. Comparatively, calorimetric biosensors monitor biological interactions as a change in heat of the system [1]. Calorimetric biosensors are niche because most enzyme catalyzed reactions and ligand-binding interactions are exothermic (i.e., they release heat proportionally to the molar enthalpy of

reaction and concentration of ligand). Likewise, optical sensors are broadly classified as labelled and label-free. The former method requires fluorophore-tagging and is typically more specific. The latter method is comprised of several techniques that monitor changes in the refractive index of interfaces where the biological interactions occur, and is considered more appealing due to the simplicity afforded by the lack of fluorophore-tagging [22,24]. Finally, electrochemical biosensors are the main topic of this work and will be discussed further below. Thus far, mass and calorimetric biosensors have had no practical impact on the commercial biosensor field; conversely, optical biosensors have shown significant progress in Research and Development (R&D), and electrochemical biosensors dominate in commercial distribution [1,22,24].

Electrochemical biosensors are broadly classified as potentiometric, conductometric, and amperometric, corresponding to measuring changes in potential, solution conductivity, and current, respectively [1,20]. Electrochemical impedance spectroscopy is a technique utilized to measure these changes. The most commercially successful biosensor is the portable mediated blood glucose sensor for diabetes management, which contributes to ~85 % of the world's commercial biosensors market [24]. The blood glucose meter operates by detecting current generated by the enzymatic oxidation of glucose to gluconic acid via glucose oxidase (GO_x) enzyme [25]. Our group has previously successfully studied blood glucose sensors using the GO_x enzyme [26] by either entrapping it in anodically-formed porous iridium oxide (IrO_x) on polycrystalline Ir substrates, or by co-depositing it with Nafion and IrO_x nanoparticles on Au substrates [27,28]. The combination of commercial success and great potential for device miniaturization of electrochemical biosensors led our group to develop biosensors that detect lipopolysaccharides (LPS) bacterial toxins using Toll-like Receptor 4 immunoproteins (TLR4) as the biological element.

2.2 Lipopolysaccharides and its binding interaction with Toll-like Receptor 4 immunoprotein

2.2.1 Gram-negative bacteria and lipopolysaccharide

Empirically, non-encapsulated bacteria in their vegetative state can be classified into two broad categories based on the retention of Gram stain [29]. In the early days of bacteriology and microscopy, Gram stain (devised by Hans Christian Gram [30]) was developed as an inexpensive, fast and easy staining method to differentiate bacteria species based on their cell wall. Bacteria with a relatively thicker cell wall layer that restricts departure of the dye after its absorption are referred to as Gram-positive bacteria, whereas the rest are called Gram-negative bacteria [31]. The latter possess an additional layer surrounding their cell walls, called the outer membrane, with ~75 % covered by (LPS) [32]. Therefore, LPS is a key cell surface marker indicative of Gram-negative bacteria. These molecules are endotoxins, which are characterized by heat stability in boiling water for up to 30 min [33], and remain cell wall-bound until cell division or bacterial death occurs. However, once released inside a person, LPS cause sepsis at blood concentrations from 0.1-1 ng/mL [33,34]. Sepsis is characterized as an overzealous inflammatory response (i.e., flulike symptoms, fever and tachycardia [35]) that damage the host [36].

The LPS molecular structure is divided into three domains, the O-antigen (composed of repeating oligosaccharide units), the core (composed of polysaccharides), and Lipid A (composed of a phosphorylated disaccharide substituted with fatty acids). Lipid A is embedded into the outer membrane and is determined to be the toxic component of LPS. This means that monomeric LPS, once released from the outer membrane, interacts with host cells via its Lipid A component to induce an overzealous inflammatory response that defines sepsis [33,37–40]. Under physiological conditions (i.e., pH ~ 7), all three domains of LPS possess a net negative charge due to the presence

of either certain sugars (pK_a ~3-4), or phosphate groups (pK_a < 3) [41], which are neutralized by divalent cations, such as Ca^{2+} and Mg^{2+} [42].

Due to its amphiphilic nature, LPS forms micellar aggregates in aqueous solutions, causing molecular weights to vary from 10^4 g/mol (monomeric state) to 10^6 g/mol in the aggregate state [43,44]. The critical micelle concentration (cmc, concentration of ligand above which aggregates begin to form) of LPS is 1-6 μM, which shifts to 1 nM in the presence of divalent cations, due to a decrease in electrostatic repulsion between the negatively charged sites of LPS [40].

2.2.2 Toll-like Receptor 4 and its interaction with lipopolysaccharide

The immune system of vertebrates is activated upon the breach of foreign microorganisms through the skin and/or mucosal epithelial layer of the respiratory, gastrointestinal or urogenital systems (i.e., ports of entry) [31,45]. The vertebrate immune system employs two strategies, the adaptive and innate immune systems, to fight off infections [31,46,47]. Adaptive immunity, compared to the innate system, targets specific pathogens and thus requires a longer time to be activated [31,46]. The innate immune response is typically activated by cells (i.e., macrophages and dendritic cells [48]) at these entry sites via triggering of Pattern Recognition Receptors (PRRs) that recognize pathogen-associated molecular patterns (PAMPs) [48–50]. PAMPs are molecules produced only by pathogens that remain relatively invariant within a class of microbes and are mutation resistant due to the utility they provide to the microorganism (as it has been noted that mutations to PAMPs are fatal to the microorganism) [47].

TLR immunoproteins are transmembrane protein receptors (i.e., they have domains that exist on both sides of the membrane) that belong to one of five families of PRRs expressed by mammalian cells [46,51,52]. To date, 10 TLR proteins have been identified in mice and humans,

appropriately labeled TLR1 – TLR10 [46]. Each of these uniquely discriminates and binds to certain PAMPs, although TLR ligands are not exclusively PAMPs [47]. For example, monomeric LPS are PAMPs that bind to TLR4, but TLR4 is also known to respond to Taxol, syncytial virus respiratory protein F, and heat shock protein 60, among other exogenous compounds and endogenous proteins [40,53].

The cellular mechanism of the TLR4-LPS binding interaction occurs with the assistance of three accessory proteins that are either present in the serum (i.e., the fluid component of blood) or are membrane-bound (i.e., immobilized on the outer membrane of the cell in a manner such that they are exposed to the serum). Once LPS molecules enter a host, LPS-binding protein (LBP, serum protein) extracts monomeric LPS from aggregates and delivers it to the cluster of differentiation 14 protein (CD14, present both in its serum and membrane-bound form) [38], which transfers LPS to Myeloid Differentiation Factor-2 (MD-2), a protein bound to and associated with TLR4 [40,51,54].

The dissociation constant of TLR4/MD-2 with the monomeric LPS-CD14 complex was determined to be 130 pM (considered to be a high affinity interaction) [55]. Crystallographic data show that the hydrophobic interface between TLR4 and MD-2 accommodates the fatty acid groups of the Lipid A domain of LPS. Micellar aggregates of LPS would not be detected by TLR4/MD-2 because the hydrophobic Lipid A portion of LPS would be present inside the aggregate structure [56,57] and thus be unavailable for its interaction with TLR4/MD-2. Formation of the TLR4/MD-2/LPS complex causes TLR4 dimerization (i.e., $(TLR4/MD\text{-}2/LPS)_2$), which initiates downstream immune signaling responsible for the overall inflammatory response [40]. A recent study has shown that, in the absence of LPS, 48 % of TLR4 is dimerized on cells that express MD-2 and CD14, whereas TLR4 remains monomeric on cells that do not express these accessory proteins.

The amount of dimerized TLR4 increases from 48 % to 74 % and 73 % in the presence of LPS from *Escherichia coli* and *Salmonella minnesota,* respectively, but decreases from 48 % to 0 % in the presence of LPS from *Rhodobacter sphaerodis*. This was attributed to the varying acylation patterns altering the conformation required for binding of TLR4/MD-2 with LPS [58].

2.3 Electrochemical biosensor design

2.3.1 Alkanethiolate self-assembled monolayers

Self-assembled monolayers (SAMs) are highly ordered monolayers formed by the spontaneous reaction of a molecule with the substrate. Molecules used to prepare SAMs are typically composed of a head group (that forms a bond with the substrate), a terminal group (that interfaces with the medium) and an alkyl chain that connects the two, as is shown by the cartoon in Figure 2.2a. Thiolate SAMs on metals are ordered monolayers that have a thiol head group, most commonly saturated alkyl chain and varying terminal groups [59]. The most common metal substrate used for this purpose is Au, due to the strong Au-S bond (as demonstrated by a computational study) [60], and its inert characteristic as it does not react with atmospheric O_2 (unlike other precious metals Ag and Cu), making it easier to handle and simpler to prepare [61,62]. The Au-S bond strength is estimated to be ~45 kcal/mol [63].

Adsorption of thiolate SAMs on Au occurs in three steps. The first step is physisorption of the thiol on the Au substrate, followed by release of its mercaptan hydrogen atom and electron transfer from Au to S, culminating in chemisorption of the thiolate [61,64]. Typically, after the completion of this step, which requires a few minutes, 80-90 % of the substrate is saturated [65]. The second step consists of the formation of interchain van der Waals (vdW) interactions, causing straightening of alkane chains, which requires 3-4 times longer than the first step to completion

[65]. The vdW interactions stabilize SAMs by 1-2 kcal/mol per each methylene group of the alkane chain [66]. The third and final step involves the reorientation of terminal groups in a timeframe requiring 35-70 times longer than the second step [65]. The straightening of alkane chains and reorientation of the terminal group refers to adoption of the all-trans conformation shown in Figure 2.2b.The completion of these steps culminates in the formation of crystalline SAMs, which, in the case of deposition on polycrystalline Au substrates (predominately Au(111) texture), means that SAMs have a $(\sqrt{3}x\sqrt{3})R30^{o}$ lattice structure [61,65,67]. Alkanethiolate molecules in crystalline SAMs on single-crystal Au(111) substrates are tilted ~32^{o} from the normal of the substrate plane [65].

In theory, SAM formation is crystalline in nature; however, defects are a major challenge in this research field. Defects in SAMs are defined as formations that deviate from an organized crystalline structure. They are undesirable because they alter the interfacial properties of the deposited layer and affect the overall stability of SAMs. There are four broad types of defects, missing rows, molecular defects, vacancy islands and domain boundaries [66]. Missing rows are typically found in short-chain alkanethiolate SAMs (alkane length < 8) due to the weak vdW forces that are unable to stabilize SAMs sufficiently, resulting in visible rows of Au that do not contain adsorbed thiolates when analyzed by scanning tunneling microscopy [66]. Molecular defects are present within well-organized domains of SAMs in several forms, such as vacancies (i.e., when an alkanethiolate is desorbed) [68] and gauche defects (when an alkanethiolate is not in the all-trans conformation) [69–73], etc. Domain boundaries are defects that exist between domains of SAMs, in instances such as boundaries between SAMs either organized in differing lattice structures or in identical lattices with alkanethiolates tilted in different directions [74,75]. These SAM defects are formed within a domain of the underlying single-crystal Au(111) [74]. Other causes of defects,

such as substrate domain boundaries and steps of single-crystal surfaces, inter-grain boundaries of polycrystalline films, and roughened surfaces caused by certain Au cleaning procedures, are not discussed in this section [66]. The literature indicates that, despite the use of single-crystal Au(111), the formation of ideal crystalline defect-less SAMs is difficult.

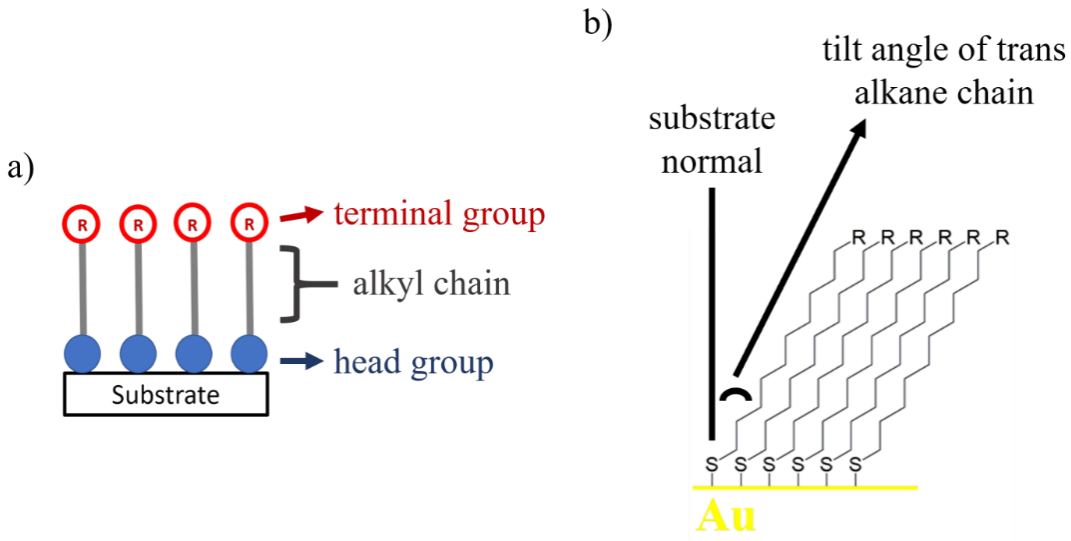

Figure 2.2: (a) Cartoon of SAMs defined by their head group (blue sphere) that forms a bond with the substrate (black rectangle), and the alkyl chain (grey line) that connects it with the terminal group (red sphere) at the interface. (b) Diagram of thiolate SAMs where the all-trans alkane chains are tilted at a certain angle from the normal of the substrate.

SAM defects have important ramifications for biosensing and protein adsorption. Whitesides *et al.* have established four criteria for the terminal groups of SAMs to resist non-specific protein adsorption: i) hydrophilicity, ii) H-bond accepting, iii) not H-bond donors, and iv) possessing a neutral charge [76,77]. This is why poly(ethylene glycol) (PEG)-terminated SAMs are observed to be the most effective functional group for inhibiting non-specific protein adsorption [78–81]. However, it has been demonstrated that, despite the use of PEG-terminated SAMs [82], the presence of defects introduce hydrophobic sites, which can increase non-specific protein adsorption [78].

2.3.2 Protein immobilization methods

In order to develop robust biosensors, our goal is to immobilize TLR to a substrate and therefore protein immobilization is highly important to this work. There are four criteria required for ideal protein immobilization, the strength and irreversibility of immobilization, retention of protein function [83], uniform and optimal orientation [84], and the ability to control protein loading (defined as the amount of immobilized molecule) [84–86]. There are numerous methods employed for this purpose that involve the deposition of an additional layer on the substrate, which then immobilizes the protein either via the biotin-streptavidin interaction [87–90], covalent-bond formation [83,84,89,91–93], or coordination chemistry [94].

Biotin-functionalized surfaces bind to the strept(avidin) protein (with the ability to bind up to four biotin molecules), which then allows for the immobilization of biotinylated protein. The advantage of this method is that the protein is strongly and irreversibly immobilized to the substrate [87–90]. The limitation of this method is that it requires modification of the amine, carboxyl, and sulfhydryl groups of the protein with biotin, which means that biotin-functionalization occurs at multiple sites of the protein, causing it to be immobilized in a non-uniform manner [95].

Antibodies (i.e., a type of protein that binds to antigens) have been covalently attached to substrates primarily by utilizing the aldehyde-hydrazide condensation reaction. In this method, the carbohydrate portion of the antibody, that does not participate in the binding interaction with antigens, is oxidized to aldehyde, which then reacts with hydrazide-functionalized substrates [83,86,89,96]. The advantage of this method is that the antibody is immobilized in a strong and irreversible manner such that the orientation is uniform and optimal (i.e., the antigen-binding domain of the antibody remains available to perform its function). The limitation of this method

is that the periodate reaction, used to oxidize carbohydrates, is harsh because it damages the antigen-binding domain of antibodies [83,94].

Whitesides *et al.* [94] utilized coordination chemistry to immobilize proteins, deposited two-component alkanethiolate SAMs, composed of thiol molecules with nitrilotriacetic acid (NTA)- and tri(ethylene glycol) (TEG)-terminal groups, on Au. The role of the NTA moiety is to tetravalently chelate Ni^{2+} (which maximally coordinates octahedrally), leaving two available coordinate sites which are satisfied with imidazole residues found on the poly-Histidine-Tag of the recombinant protein of interest. This His-Tag is included in the amino acid sequence of some commercial recombinant proteins and thus is consistently present in the same location, which means that further user modification is unnecessary, resulting in uniformly oriented immobilization. The utilization of two component thiolate SAMs allows for variation of receptor loading by manipulating the ratio of the two thiolate components. Experimentally, it was determined that the same bioreceptor has a greater binding affinity when immobilized using the His-Tag NTA SAM technique, compared to the covalent-modification method, which was partially attributed to immobilization of the antibody in a manner that ensures that its antigen-binding domain remains available and unaffected [94]. This satisfies three of four criteria for ideally immobilized proteins (i.e., retention of protein function, ability to control protein loading on the substrate, and uniform and optimal orientation of the protein).

The minor drawback to this method is that the protein immobilization is reversible and dependent on electrolyte conditions. This is because NTA coordinates Ni^{2+} via an available nitrogen lone pair and three carboxylate anions, which are pH dependent, as seen by the deprotonation states shown in Scheme 2.1. Furthermore, the strength of the chelation bonds between the carboxylate anion and Ni^{2+} is ionic strength dependent [97]. Similarly, the Histidine

amino acid forms coordination bonds with Ni^{2+} via the nitrogen lone pair of the imidazole ring, which is only available at pH > 6, as shown by the deprotonation states of Histidine in Scheme 2.2 [98]. It is important to note that the pK_a values in Schemes 2.1 and 2.2 may not perfectly correspond to those of their NTA-SAM and His-Tag counterparts. This suggests that biosensors utilizing this immobilization technique would ideally operate in neutral buffered solutions. This Ni^{2+}-His-Tag interaction is commonly utilized during protein purification via metal chelate affinity chromatography, which also shows pH dependent elution of poly-Histidine Tagged proteins [99,100].

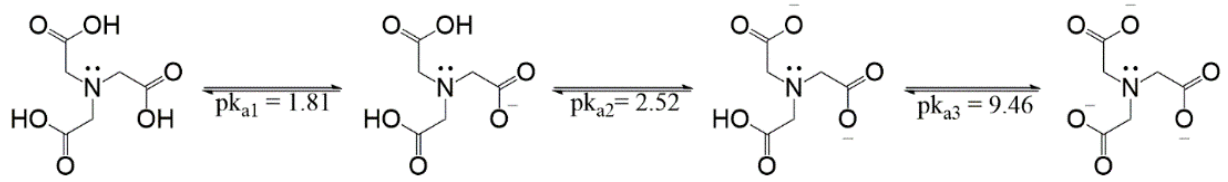

Scheme 2.1: Protonation states of chelating agent Nitrilotriacetic acid (NTA). The pK_a values were taken from ref [97].

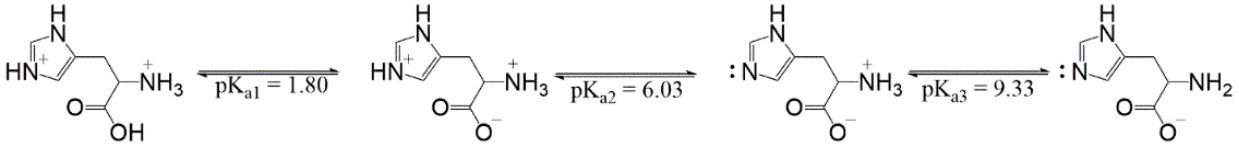

Scheme 2.2: Protonation states of Histidine amino acid. The pK_a values were taken from ref [98].

2.4 Electrochemical Toll-like Receptor-based biosensors using SAMs

As discussed in Section 2.2.2, TLR immunoproteins belong to a class of PRRs that broadly recognize PAMPs. Currently, there are 10 TLR proteins that have been identified, labelled as TLR1-10, each of which uniquely binds to its respective PAMP. TLR-based electrochemical biosensors are believed to operate via a blocking mechanism as the immunoproteins dimerize when binding to their respective PAMP, restricting access of electroactive ions to the underlying substrate. This typically manifests itself as a decrease in current, which is measured using

electrochemical impedance spectroscopy (EIS) and cyclic voltammetry (CV). Figure 2.3 displays a cartoon demonstration of an ideal TLR4-based sensor in the presence of LPS. This section discusses sensors prepared using TLR3 (to detect double-stranded RNA), TLR5 (to detect flagella), TLR2, TLR2/1, and TLR2/6 (to detect lipopeptides), and TLR4 (to detect LPS). It is important to note that dimerization of TLR may not be necessary for an increase in R_{CT} to be observed, as binding of the large LPS molecule to the surface would be sufficient to block the pathway of solution ions to the underlying Au electrode.

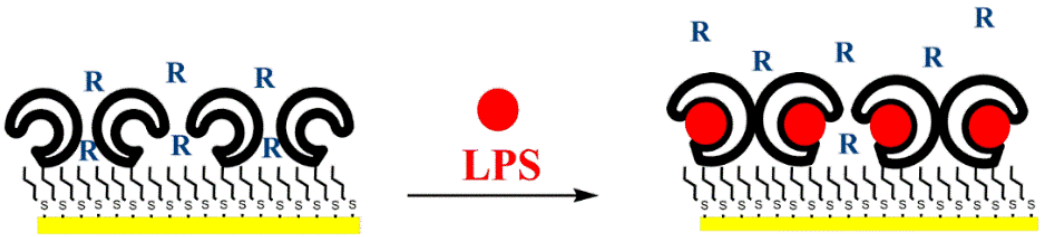

Figure 2.3: Representative schematic of electrochemical biosensors prepared by the immobilization of TLR4 (black horseshoe shape) on thiolate SAMs. This sensor is hypothesized to operate via a blocking mechanism, as in the presence of LPS (red sphere), TLR4 dimerization is induced. As proposed by the Birss group [15,18], this should restrict access of electrolyte ions (R) to the Au substrate, noting that simple binding of LPS to TLR4 would also predict a resistance increase.

2.4.1 TLR3-based biosensors

To date, there has only been a single study that prepared electrochemical TLR3-based sensors prepared using SAMs [101]. TLR3 are immunoproteins that intracellularly recognize double-stranded RNA (dsRNA), which is a PAMP associated with viral infections [102,103]. It has been demonstrated that TLR3 forms dimers when binding to ~50 base pair dsRNA, and dsRNA greater than 50 bp requires the formation of TLR3 oligomers. Kraatz *et al*. prepared TLR3-based sensors by depositing Lipoic N-hydroxysuccinimide ester (commonly referred to as Lip-NHS) on

Au substrates, which resulted in the formation of di-thiolate SAMs with a terminal NHS-ester group. NHS ester acts as a leaving group and forms a covalent bond with primary amines, which was used to immobilize proteins with random orientation. This TLR3-based sensor was able to detect polyinosinic-polycytidylic acid (poly I:C, a 200-1000 bp dsRNA mimicking molecule) with a Limit of Detection (LOD) of 0.06 µg/mL and a linear dynamic range of 0.2-1.0 µg/mL [101].

2.4.2 TLR5-based biosensors

To date, there have been two studies that prepared electrochemical TLR5-based sensors using SAMs [104,105]. TLR5 is an immunoprotein that recognizes PAMPs called flagellin, which are protein monomers that comprise bacteria flagella (i.e., appendages responsible for movement of the microorganism in an aqueous environment) [106,107]. Kraatz *et al.* assembled a TLR5-based electrochemical sensor by also utilizing Lip-NHS di-thiolate SAMs formed on Au substrates, which are used to establish covalent bonds with the primary amines of proteins. These proteins possessed the ability to detect bacterial flagellin from *Salmonella typhimurium* and *Bacillus subtilis* with concentrations ranging from 0.1-2 µM [104].

Jemere *et al.* designed TLR5-based sensors using silane SAMs prepared from a molecule called 3-glycidoxylpropyldimethoxylmethylsilane (GPDMMS), where an epoxide ring is the terminal group, on bare- and nanostructured-Indium Tin Oxide (ITO) substrates. These nanostructured-ITO substrates were prepared using Glancing Angle Deposition (GLAD). The protein was immobilized by the reaction between the terminal epoxy ring and primary amines of TLR5, resulting in the formation of a covalent bond. Sensors prepared on GLAD-ITO substrates displayed an 80 times lower LOD towards bacterial flagellin from *Salmonella typhimurium* than does bare-ITO [105].

2.4.3 TLR2-, TLR2/1-, TLR2/6-based biosensors

To date, there have been two research groups that have prepared electrochemical sensors using TLR1, 2, and 6 immobilized on SAMs [108]. Depending on the heterodimer formed, TLR2 immunoproteins possess the ability to recognize different lipopeptides. Di- and tri-acylated lipopeptides are PAMPs expressed on cell surfaces of Gram-positive and Gram-negative bacteria, respectively, and correspondingly induce TLR2/6 and TLR2/1 dimerization. Kraatz *et al.* constructed TLR1-based, TLR2-based, and TLR2/1-based sensors by immobilizing proteins, using the identical di-thiolate SAM molecule and protein attachment method discussed above. These sensors responded to a synthetic tri-acylated lipopeptide, Pam3CSK4, exhibiting a 21 ± 7 %, 32 ± 6 %, and 47 ± 17 % increase in charge-transfer resistance (R_{CT}), respectively, when exposed to 10 μM synthetic ligand. Sensors prepared by simultaneous immobilization of both TLR1 and 2 generated a still larger magnitude of response [108].

She *et.al.* developed TLR2/6-based sensors by using di-thiolate SAMs formed using Lip-NHS, which is the identical molecule utilized by Kraatz *et al.*, to prepare their TLR-based sensors. The terminal NHS-ester terminal group allows for covalent bond formation with the primary amines of TLR2 and TLR6. This sensor was able to detect Pam2CSK4 (i.e., a synthetic simulant of diacylated lipopeptide) and distinguish it from LPS at concentrations ≥ 1000 ng/mL (i.e., at concentrations when LPS could potentially form micelles [40]) [109]. This sensor was able to detect live Gram-positive bacteria, such as *Bacillus lichenformis* and *Enterococcus hirae*, and responded minimally to Gram-negative bacteria, such as *Escherichia coli* [109].

2.4.4 TLR4-based biosensors

To date, there have been only a few research groups that prepared electrochemical TLR4-based sensors using SAMs [16,18,110]. As discussed in Section 2.2.2, TLR4 immunoproteins recognize LPS, which is a PAMP endotoxin associated with Gram-negative bacteria. The theoretical dimension of the TLR4/MD-2 complex is 7.7 nm x 7.2 nm x 9.4 nm. This was determined by using the Draw Protein Dimensions Python program [111] on the crystal structure of mouse TLR4 and the associated MD-2 protein complex [112]. Cho *et al.* prepared sensors using the dithiobis(succinimidyl undecanoate) molecule to form alkanethiolate SAMs with a terminal NHS ester group, which allowed for the immobilization of TLR4 via covalent bond formation with their primary amines. These sensors had the ability to detect LPS with an LOD of 2×10^{-5} ng/mL [110]. Similar sensors designed by Kraatz *et al*., using Lip-NHS di-thiolate SAMs with NHS ester terminal groups that immobilize TLR4 via covalent bond formation with primary amines of TLR4, demonstrated LODs of $\sim 1 \times 10^{-5}$ ng/mL for LPS extracted from *Escherichia coli* and *Salmonella* [113]. This sensitivity is consistent with the literature because the critical micelle concentration of LPS is 10-60000 ng/mL, and TLR4/MD-2 is unlikely to interact with LPS aggregates [40]. Jemere *et al.* prepared sensors using GPDMMS SAMs, which contain a terminal epoxide ring, deposited on GLAD-ITO substrates, as also described previously in Section 2.4.2. TLR4/MD-2 was immobilized on the surface via covalent bond formation between their primary amines and terminal epoxide ring of SAMs. These sensors demonstrated LODs of 2 ng/mL [105].

The first iteration of sensors prepared by Birss *et al.* involved the use of alkanethiolate SAMs formed by co-adsorption of two distinct thiol molecules, 3-mercaptopropionic acid (MPA) and 11-mercaptoundecanoic acid (MUA). The purpose of the shorter-chain MPA was to minimize the interfacial resistance, while that of the longer-chain MUA was to have its terminal groups

modified to immobilize TLR4. Carbodiimide chemistry was utilized to replace the terminal carboxylic acid with NHS ester groups, followed by the formation of covalent bonds with the primary amine of Nitrilotriacetic acid-lysine (NTA-lysine), which subsequently chelates Ni^{2+}. This Ni^{2+} further chelates two Histidine-molecules of the 10 His-Tag of the protein, which means up to five surface-bound Ni^{2+} ions can chelate the 10 His-Tag of a single protein, resulting in the immobilization of TLR4. The design of these sensors was superior to the previously described sensors because they immobilized TLR4 in a controlled orientation on the SAM surface. This sensor generated a logarithmic response when exposed to either 1-1000 ng/mL LPS (extracted from *Escherichia coli*) or to LPS in a more complex matrix (i.e., 1-10^5 cells/mL of heat-killed *Salmonella typhimurium* (HKST) lysate cells). As a positive feature, the sensors did not response to heat-killed *Staphylococcus aureus* (Gram-positive bacteria) or UV-inactivated Rhabdovirus [16]. However, this sensor had a high interfacial resistance of roughly one megaohm, likely due to the tight-packing of the long alkane chain SAMs used, and thus sensor testing had to be performed in a Faraday cage, thereby hindering its potential future-use in a portable device.

The second iteration of this sensor eliminated this issue by introducing Ferrocenyl-thiolate (Fc-thiolate) molecules into the monolayer [18]. These sensors were prepared by co-adsorption of three distinct thiol molecules, 11-mercaptoundecanol (MUO), which acts as a spacer thiol and generates a hydrophilic surface to minimize non-specific adsorption of biomolecules, 11-mercaptoundecanoic acid (MUA), which serves the identical purpose as it did in the previously discussed Birss sensor, and 11-mercaptodecyl-ferrocenylcarboxamide (Fc-amide), which mediates and amplifies flow of current from solution $Fe(CN)_6^{4-}$ to the Au electrode, thereby decreasing interfacial resistance to ≤ 1 kΩ. This low resistance is similar to what was observed for the TLR3-[101] and TLR5-based sensors discussed above [104], although ,in their case, this likely arose

from the use of Lip-NHS SAMs that are suspected to be less tightly-packed than alkanethiolate SAMs due to the bulky di-thiolate group that adsorbs Lip-NHS to the Au surface. The Fc-based sensor [18] also responded to HKST lysate cells (in the same concentration range as the previously discussed Birss group sensor), but not to *S. aureus* lysate cells and UV-inactivated Rhabdovirus.

2.5 Electrochemistry of alkanethiolate SAMs containing Ferrocenyl-thiolates

Alkanethiolate SAMs that contain thiolates with terminal Fc-moieties are commonly referred to as Ferrocenyl-thiolate SAMs. Their electrochemical properties are typically studied using cyclic voltammetry (CV) scans collected in aqueous solutions containing non-electroactive ions. CV scans are collected beginning at low potentials at which no Faradaic current passes. The linear increase in potential (anodic scan) initially shows charging currents (i.e., non-Faradaic) until an anodic peak is seen when the potential for the oxidation of the surface-bound Fc to Fc^+ is reached. The Faradaic current then drops back to just the charging current due to the complete oxidation of the Fc moieties, forming Fc^+, with the reverse scan showing the same trends as Fc^+ is reduced to Fc [114]. A cartoon of a single CV scan of a Fc-thiolate SAM is shown in Figure 2.4a, with Figure 2.4b showing how the baseline corrected Faradaic charge (Q), peak current (i_p), peak potentials (E_p) and the full width at half maximum (ΔE_{fwhm}) of the peaks are obtained. This is a characteristic electrochemical representation of any redox active molecule bound to the surface and is not specific to the Fc/Fc^+ redox couple.

CV peak characteristics are used in the literature to either determine certain properties of Fc-SAMs or assess the electrochemistry of Fc. For example, the integrated charge values, when divided by Faraday's constant (96485 C mol^{-1}) and real surface area of the underlying Au electrode, gives the Fc surface coverage in units of mol cm^{-2}. Furthermore, the surface-confined

Fc is typically studied using binary SAMs because the second component (commonly referred to as the diluent SAM) isolates the Fc groups from each other, which minimizes lateral repulsive interactions between adjacent Fc^+ groups when oxidized. CVs of surface-confined redox molecules participating in an ideal one electron process have four characteristics: the difference between anodic and cathodic peak potentials is zero (i.e., $\Delta E_p = E_{p,a} - E_{p,c} = 0$), the ratio of anodic peak current to cathodic peak current is one (i.e., $i_{p,a} / i_{p,c} = 1$), both anodic and cathodic peak currents are linearly proportional to the scan rate, and peak width at half-height at 298 K is 90.6 mV [115].

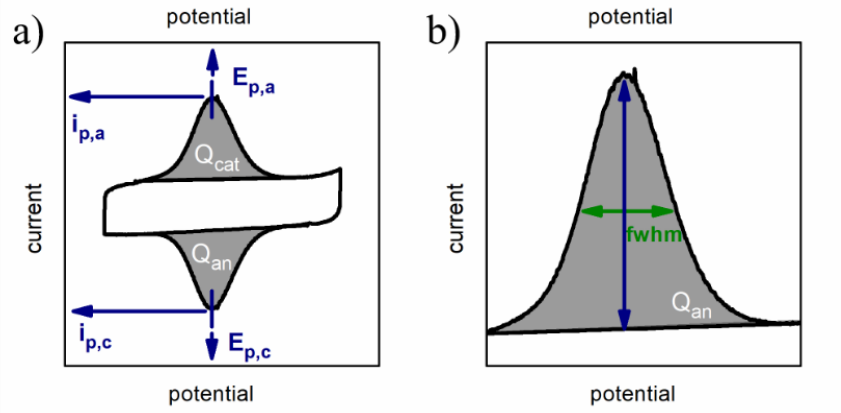

Figure 2.4: Cartoons showing the measurable characteristics from a CV of a Fc-thiolate SAM. In panel a, grey areas represent the Faradaic charge of the oxidation/reduction of Fc/Fc^+, with the blue markers showing the respective peak potentials. Panel b shows a close-up of the anodic scan from panel a, where the blue double-sided arrow gives the maximum current of the Faradaic peaks, and the green double-side arrow is the full width at half-maximum (i.e., peak width).

2.5.1 Effects of various Fc populations and interactions during SAM formation on CV response

Although this thesis focusses primarily on ternary SAMs, the literature primarily describes the properties of binary SAMs, with ternary SAMs expected to be influenced by the same interactions. Binary Fc-thiolate SAMs are monolayers consisting of two different thiolate

molecules and could be deposited either as mixed monolayers (i.e., components that are distributed uniformly) or both contained mixed and macroscopic monolayers (i.e., components that remain segregated forming "islands"). Macroscopic domains, in this instance, are approximately a few nm in diameter, dimensions estimated to be sufficiently large so that the properties of the microenvironment are indistinguishable from a pure monolayer (i.e., monolayer composed of a singular component) [116]. The distribution of each thiolate molecule within binary SAMs is dependent on the enthalpy and entropy of the system. Enthalpy favors maximizing intermolecular interactions between adsorbed thiolates, causing phase-segregation, whereas entropy favors disorder, causing mixing of SAM components [116–120]. Based on calculations and empirical data, Whitesides *et. al.* [116–120] have claimed that it is "nearly impossible" for SAMs, immersed in their precursor solution, to form domains during assembly when at equilibrium with their precursor solutions, because in the presence of excess dissolved thiols, the entropic contributions outweigh enthalpy. The reverse is observed in the presence of strong interactions between alkanethiolates, causing their lateral movement [116–120].

As an example of the electrochemical effects of SAMs containing domain-formation or dispersed thiols, binary SAMs consisting of co-adsorbed $HS(CH_2)_9CH_3$ and $HS(CH_2)_{12}Fc$ are reviewed. These thiols can deposit as either ideal uniformly-distributed monolayers (i.e., SAMs in which Fc-thiolates are isolated from each other) or consist of populations of two types of distributions of Fc-thiolates, both isolated and clustered, as shown in Figure 2.5 [121]. In the former case, Fc experiences a homogeneous microenvironment, resulting in formal potentials that reflect the interfacial dielectric constant, giving peak widths of 90.6 mV. In the latter case, Fc experiences two different microenvironments, the first being where Fc-moieties are isolated from the others, and the second being governed by neighboring charge effects of Fc^+ generated at

positive potentials, where Fc-moieties are clustered. The two populations of Fc will each exhibit unique electrochemistry and exhibit slightly different formal potentials, resulting in the generation of broader CV peaks. Lennox *et al.* prepared these binary SAMs and deconvoluted the CV peak into its two components using Gaussian-Lorentzian fittings [121].

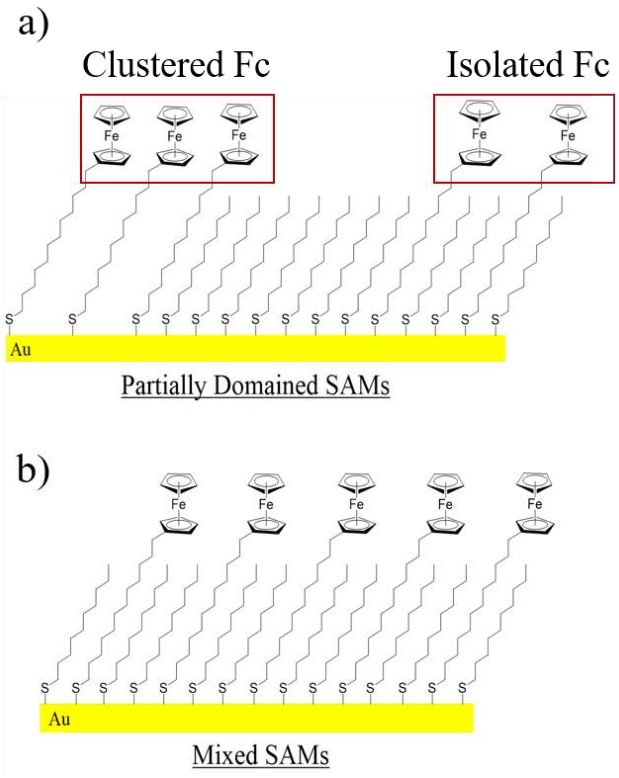

Figure 2.5: Binary SAMs composed of $HS(CH_2)_{12}Fc$ and $HS(CH_2)_9CH_3$ distributed as a) partially clustered domains and b) mixed SAMs.

Moreover, binary SAMs prepared from ethanolic thiol solutions containing 10 % $HS(CH_2)_{12}Fc$ and 90 % $HS(CH_2)_9CH_3$ resulted in 25% of the deposited Fc-thiolate in domains, based on CV peak deconvolution [121]. Similarly, SAMs deposited from a 60 % Fc-thiol solution after a 5 s immersion time showed that Fc-thiolates display a greater propensity to be isolated, as opposed to clustered, when compared to SAMs formed after 24 h of immersion, seen from CV

peak deconvolution studies [121]. This demonstrates that Fc-moieties can self-associate to a limited degree, especially with longer immersion times.

Lennox *et al.* utilized identical CV peak deconvolution to label defects of alkanethiolate SAMs [122] and monitor their presence during the reduction desorption process [123]. In the former study, the authors assigned two specific CV peaks to single-site and domain defects and utilized that assignment to determine that longer-chain SAMs have a higher ratio of single-site to domain defects than shorter-chain SAMs [122]. In the latter study, using the same peak assignment to categorize defects, it was determined that, at increasingly negative potentials, the ratio of domains to single-site defects becomes larger, indicating that domains of SAMs desorb, instead of single thiolate molecules [123].

2.5.2 Standard heterogeneous electron-transfer kinetics of Fc-thiolate SAMs

The heterogeneous electron-transfer characteristics of Fc-thiolate SAMs have been studied to better understand donor-acceptor systems [114]. The primary mechanism of charge-transport between Fc/Fc^+ and the underlying Au substrate is quantum tunneling. Nijhius *et al.* utilized tunneling junctions, showing that electrons tunnel more efficiently "through-SAMs" than "through-space" due to a phenomenon known as super-exchange tunneling. It is important to note that "through-SAMs' tunneling does not mean that electrons are physically flowing through the alkane chains.

The standard rate constant of electron-transfer (k^0) through Fc-thiolate SAMs is dependent on both the reorganization energy (λ) of Fc and the electronic coupling factor between Fc and the underlying Au substrate (H_{ab}) [114,124]. The reorganization energy is related to the energetics of nuclear movement of the atoms from the initial complex (i.e., Fc) to the final product (i.e., Fc^+)

[114,125]. According to electron-transfer theory, the electronic-coupling factor exponentially decays with distance between the acceptor-donor system [126]. In these studies of heterogeneous electron-transfer kinetics, it was important to ensure that Fc experiences a homogeneous environment, as clustered Fc domains or defect-sites result in the inaccurate determination of λ and k^0 [127–131]. In this section, discussion will be restricted to k^0 of Fc-thiolate SAMs.

CVs of $HS(CH_2)_nNHCOFc$ and $HS(CH_2)_{n+1}OH$ binary SAMs collected in 1 M $HClO_4$ at room temperature of n = 7, 10, and 15 SAMs were used to determine k^0, giving values of 6.6 x 10^4, 1.2 x 10^3, and 6.6 s^{-1}, respectively, suggesting that k^0 decreases for longer-chain alkanethiolate SAMs. This trend is attributed to a decrease in the electronic coupling between the Fc and Au substrate caused by longer tunneling distances. The tunneling constant determined from these SAMs was calculated to be 0.85 $Å^{-1}$ [124], which is diagnostic of "through-SAM" tunneling [132,133]. The effect of the linkage group that covalently attaches the Fc group to the SAMs on k^0 was examined by preparing two binary SAMs, $HS(CH_2)_nCH_2OH$ and $HS(CH_2)_nNHCOFc$ (carboxamide linkage), and $HS(CH_2)_nCH_2CH_3$ and $HS(CH_2)_nCH_2CH_2Fc$ (methylene linkage). For n = 7-10 SAMs, no trends in k^0 were observed between Fc linked using two different functional groups [134].

2.5.3 Effect of terminal group of diluent thiolates on the thermodynamics and kinetics of Fc-based SAM electrochemistry

The terminal groups of SAM components play an important role on both the thermodynamics and kinetics of Fc-thiolate SAMs, even though these components are redox inactive. For example, binary SAMs composed of $HS(CH_2)_6Fc$ and diluent SAMs of identical carbon chain length with terminal groups such as $-CH_3$, -COOH, -OH, -CN, and -Br, were

examined by collecting CVs in aqueous solutions of 0.1 M methane sulfonate [135]. The data suggest that, the greater the polarity of the terminal group, the lower the formal potential, with the difference between the most positive (i.e., of -CH_3 terminated SAMs) and least positive (-COOH terminated SAMs) potentials being 0.20 V [135]. The authors proposed [135] that these variations are due to differences in the interfacial dielectric constants. The Born equation states that any difference in the formal potentials of a redox-couple in two solvents can be attributed to the difference in the Gibbs free energy of transfer. This energy is proportional to the difference in the dielectric constants, which means the lower the dielectric constant (i.e., the lower the polarity), the greater the energy required for an oxidation reaction to occur. When applying it to this system, this means that non-polar interfaces cause a positive shift in the formal potential values of Fc/Fc^+. This is the simplified version of the theory behind the interfacial ion solvation model [135,136]. This model can predict the 0.25 V increase in the oxidation potential of $HS(CH_2)_6Fc$ when the alkane chain length of the -CH_3 terminated diluent thiol increases from 4 to 10. This is because, in an increasingly alkane-like environment, a greater thermodynamic price is required to oxidize Fc to its cationic form [135,137].

In another study, it was shown that binary SAMs composed of $HS(CH_2)_{12}Fc$ and diluent molecules that are either $HS(CH_2)_{11}CH_3$ or $HS(CH_2)_{21}CH_3$, colloquially referred to as exposed and buried SAMs, respectively, affect the kinetics of the Fc/Fc^+ reaction. The standard electron-transfer rate constant, derived from alternating current voltammetry data in 1.0 M $HClO_4$, was calculated to be 1700 and 200 s^{-1} for the exposed and buried SAMs, respectively. This shows that burying the terminal Fc groups in a non-polar environment affects the kinetics of Fc electrochemistry when part of a thiolate SAM [138].

The microenvironment of the terminal Fc groups of Ferrocenyl-thiolate SAMs was further modulated by incorporating acidic or basic diluent SAMs (of similar alkane chain length) and also by varying the pH of the electrolyte [121]. Fc-thiolate SAMs, diluted with $HS(CH_2)_{11}COOH$ or $HS(CH_2)_{11}NH_2$, were used to determine the effect of adjacent acidic or basic groups on Fc electrochemistry. CVs of acidic binary SAMs experienced a 120 mV cathodic shift as the electrolyte pH increased from 2.5 to 7.5 [121]. Similarly, basic binary SAMs experienced a 130 mV cathodic shift with the same increase in electrolyte pH. Meanwhile, no shift in the redox peak potential was observed when $HS(CH_2)_{11}CH_3$ was utilized as a diluent. The authors attributed these trends to deprotonation of -COOH and $-NH_3^+$ at higher pH, creating a more negatively-charged and neutral terminal groups surrounding Fc^+, respectively. This phenomenon is commonly referred to as neighboring charge effects [121].

2.6 Electrochemical Techniques

2.6.1 Cyclic voltammetry

Cyclic Voltammetry (CV) is a common method used in electrochemistry, where the current flow at a working electrode (WE) is monitored vs a reference electrode, and the rate of potential change (sweep rate, v) is usually changed. CV peak area integrated with respect to time gives the charge passed in the oxidation and/or reduction reaction [17]. Experimental sample CVs of surface-confined and mediation CVs, along with a respective Tafel plot, are shown in Figure 2.6a, b, and c, respectively. In panel a of this figure, CVs of redox-active SAMs display characteristics of reversible surface-confined electrochemistry, giving symmetrical anodic and cathodic peaks. Also, is it observed that double layer charging currents (i_{dl}) flow on either side of the Faradaic

peaks [17], with the double-layer capacitance (C_{dl}) [114] given by Equation 2.1 and discussed in more detail in Chapter 4.

The electrochemistry of redox-active species in solution is dependent on factors such as convection, sweep rate, concentrations, rate constants, and applied potential. In mediation electrochemistry, where two redox active species are present, the surface-confined electroactive molecule catalyzes the charge-transfer of the redox-active molecule in solution. In Figure 2.6b, the increase in current observed at larger anodic potentials is due to an increase in the number of charge-transfer reactions of the redox-active species in solution catalyzed by the surface-confined electroactive species, which will be discussed in greater detail in Section 4.1.2 [139]. When the peak current is reached, the redox chemistry of the redox-active species is fully diffusion controlled, with a $t^{-1/2}$ drop-off in current seen after the peak [17].

$$C_{dl} = \frac{i_{dl}}{\nu} \qquad \text{Equation 2.1}$$

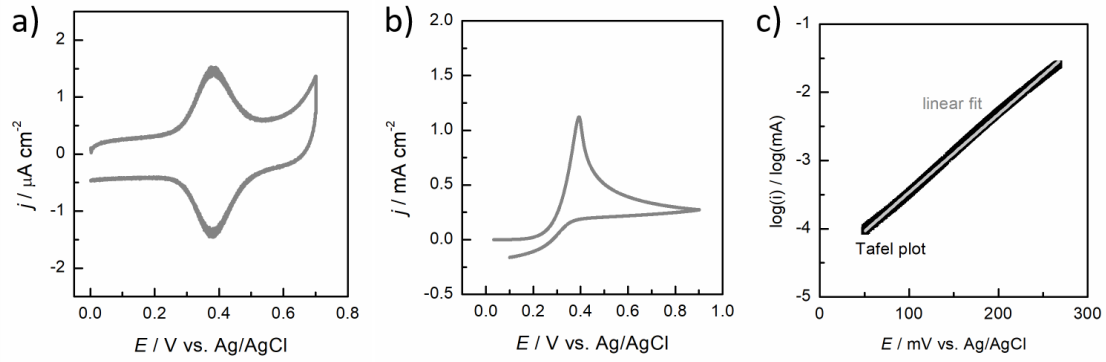

Figure 2.6*:* Typical reversible surface-confined and mediation CVs, and Tafel plot shown in panels a, b, and c, respectively. The WE consisted of a sputtered 100 nm Au layer, coated with a Fc-containing thiolate SAM. The CVs in panel a and b were collected in 0.2 M PB (pH 7.0) and 5 mM $K_4[Fe(CN)_6]$ + 0.2 M PB (pH 7.0), respectively. The Tafel plot in panel c was extracted from the anodic scan of the mediation CV in panel b and the Tafel slope was obtained from the linear fit of the plot. More details are provided in captions of Figure 4.2a, Figure 4.3a and b, respectively.

Mediation electrochemistry observed in this thesis work occurs between Ferrocenyl-thiolate immobilized on Au and $Fe(CN)_6^{4-}$ present in solution [140]. In this system, thermodynamically, the oxidation of $Fe(CN)_6^{4-}$ ($E^{o'}$ = 0.24 V vs. Ag/AgCl) can occur prior to the oxidation of Fc (E_p = 0.38 V vs. Ag/AgCl). However, due to the insulating nature of the rest of the thiolate SAM [141,142], no current flows until the oxidation of Fc occurs, with Fc^+ then mediating or catalyzing the oxidation of $Fe(CN)_6^{4-}$. This results in the reduction of Fc^+ back to Fc, but due to the presence of an anodic overpotential, Fc is rapidly oxidized again, thus giving an amplification effect [18,140]. This also explains the lack of a cathodic peak in the mediation CV, as it is thermodynamically unfavorable for Fc to reduce $Fe(CN)_6^{3-}$ at potentials positive of 0.24 V and the insulating nature of the rest of the thiolate-based monolayer blocks the reduction of $Fe(CN)_6^{3-}$ [139,140,143]. A schematic of the thermodynamics of electrochemical mediation of $Fe(CN)_6^{4-}$ oxidation by the immobilized-Fc^+ is shown in Figure 2.7 [143].

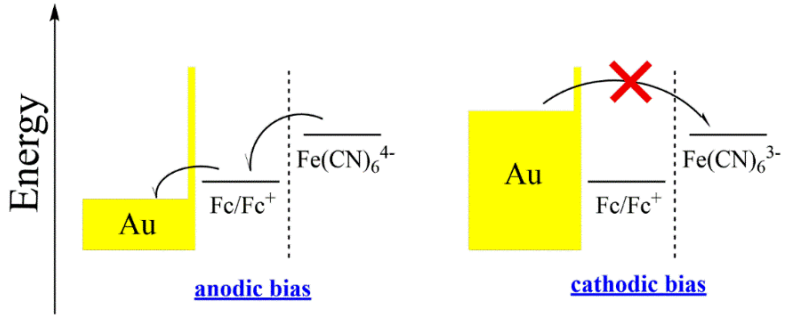

Figure 2.7: A simplified schematic of electrochemical rectification between immobilized Ferrocenyl-thiolate SAMs and ferrocyanide in solution under anodic bias (on the left) and cathodic bias (on the right). The dotted line represents the substrate-solution interface.

The mediation electrochemistry presented in this work is represented by Reactions 2.1 and 2.2 below (i.e., the 'cross-reaction' [18,140]). In Chapters 4 and 5, the RDS (either Reaction 2.1 or 2.2) is determined from the Tafel slope values, where the Tafel slope is obtained from the Butler-

Volmer equation (Equation 2.2), which defines the kinetics of irreversible charge-transfer controlled electrochemistry by describing the relationship between net current (i_{net}) and applied overpotential (η). In this equation, i_0 is the exchange current, α_a and α_c are the transfer coefficient of the anodic and cathodic reactions, respectively, T is temperature in units of Kelvin, F is the Faraday constant (F = 96485 C mol^{-1}), R is the universal gas constant (8.314 J K^{-1} mol^{-1}) [17], and the Tafel slope is given by Equation 2.3.

$$Fc \rightleftharpoons Fc^+ + e^- \qquad \text{Reaction 2.1}$$

$$Fc^+ + Fe(CN)_6^{4-} \rightleftharpoons Fc + Fe(CN)_6^{3-} \qquad \text{Reaction 2.2}$$

$$i_{net} = i_0 \left(e^{\frac{\alpha_a F \eta}{RT}} - e^{\frac{\alpha_c F \eta}{RT}} \right) \qquad \text{Equation 2.2}$$

$$T.S. = \frac{2.3RT}{\alpha F} = \frac{59\ mV/decade}{\alpha} \qquad \text{Equation 2.3}$$

2.6.2 Electrochemical impedance spectroscopy

Electrochemical Impedance Spectroscopy (EIS) is a technique where an alternating potential is applied to the WE, and the current response is measured and analyzed. The data are typically then fitted to an equivalent electric circuit that models the electrochemical processes occurring at the WE [144]. According to Ohm's law, applying an alternating potential with a sinusoidal waveform across a resistor generates an in-phase sinusoidal current, where the waveform mimics the periodicity of the alternating potential, and the resistance remains constant [145]. Introducing a capacitor in parallel to the resistor generates a sinusoidal current that is out-of-phase with the alternating potential waveform, giving a resistance that changes with time (and is now called impedance, Z).

Figure 2.8a shows the out-of-phase applied potential and current response, and Figure 2.8b shows the in-phase sinusoidal waves and corresponding magnitude of impedance (i.e., absolute value of Z (abs(Z)) calculated using Ohm's law. Impedance is commonly conceived of as a two-dimensional vector where the length corresponds to the magnitude of the impedance (abs(Z)) and the phase angle is φ. Figure 2.8c shows this two-dimensional Z plotted on Cartesian coordinates, where the x-projection and y-projection of the Z vector corresponds to the real (Z') and imaginary impedance (Z''), respectively [144,145].

This technique is called spectroscopy because data are collected over a range of alternating current (AC) frequencies. Both the abs(Z) and φ are dependent on the AC frequency. Nyquist plots are a collection of Z vectors, such as the singular one shown in Figure 2.8c, over the entire range of frequencies used [144,145]. In the case of biosensors and SAMs, Nyquist plots typically resemble a semicircular arc, where the number of arcs can correspond to unique electrochemical processes occurring at the WE [143].

Typical Nyquist plots encountered in this work were comprised of a single semicircular arc in the high frequency range (close to the origin) and a straight 45^{o} line in the low frequency range, as shown in Figure 2.9a. These data can be fit to the Randles equivalent circuit (shown in Figure 2.9b) as established by prior biosensor literature [144,145], including the work from the Birss group [16,18]. According to this fitting, the solution resistance (R_s) is determined from the resistance at high frequencies and the charge-transfer resistance (R_{CT}) is determined from the diameter of the semicircle. In this work, EIS data were collected at a potential at which the charge-transfer reaction rate is kinetically controlled. Specifically, the magnitude of R_{CT} is monitored during addition of LPS to the TLR4 sensor system. As previously described, TLR4 dimerizes in the presence of LPS, thus limiting access of solution phase $Fe(CN)_6^{4-}$ to surface bound Fc/Fc^+

[16,18]. Hence, the charge-transfer resistance, in this work, reflects the resistance of the rate determining step in a series of individual reaction steps and is inversely proportional to i_{net} from Equation 2.2 (i.e., the Butler-Volmer Equation).

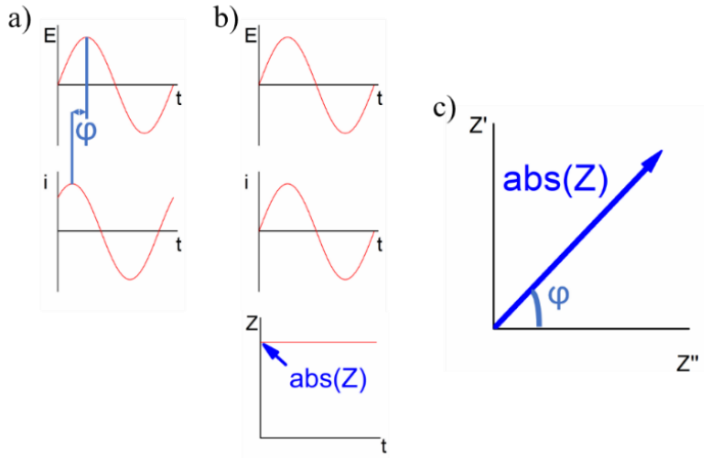

Figure 2.8: Panel (a) shows the out-of-phase sinusoidal waves of the applied potential and the resulting current response, where φ is the phase shift between them. Panel (b) shows the in-phase sinusoidal waves of applied potential and current response, and the corresponding impedance calculated using Ohm's law. Panel (c) shows the impedance plotted as a two-dimensional vector with the length of the vector corresponding to its magnitude and the angle from the x-axis corresponding to the phase angle. The x-axis and y-axis projections of impedance are the real and imaginary impedance, respectively.

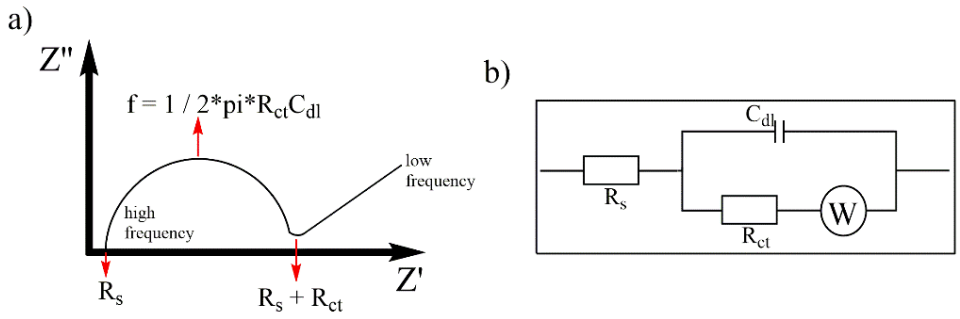

Figure 2.9: Panel (a) shows a cartoon of a Nyquist plot containing a single arc and a Warburg impedance element, showing how the solution (R_s) and charge-transfer resistance (R_{CT}) are obtained from the Z' values, and the double-layer capacitance (C_{dl}) from the frequency (f) at the top of the arc, assuming that the electrochemical process occurring at the WE interface is modeled as a Randles circuit. The Randles circuit is shown in panel (b). In this circuit, the Warburg element (W) accounts for the 45° linear portion of the Nyquist plot encountered at low frequencies.

The double-layer capacitance is commonly modeled as a parallel-plate capacitor, as seen in Equation 2.4, where ε_0 and ε_r are the permittivity of free space and the SAM, respectively, and d is the thickness of the SAM layer. The double-layer capacitance value can predict the insulating nature of the SAM, as a thinner and more polar SAM, as well as a lower coverage on the underlying metal surface, all increase the capacitance values. In Equation 2.4, the capacitance value is in units of F/m^2 (i.e., if ε_0 and d are in the units of F m^{-1} and m, respectively).The double-layer capacitance was determined in this thesis work from the CV results, as discussed in Section 4.3.2 [17], while the charge-transfer resistance was considered to be due to the magnitude of the mediation current flowing from $Fe(CN)_6^{4-}$ to the Au substrate via the immobilized-Fc thiol.

$$C = \frac{\varepsilon_0 \varepsilon_r}{d} \qquad \text{Equation 2.4}$$

Chapter Three: Experimental Methods

3.1 Chemicals

1-Ethyl-3-(3-dimethylaminopropyl carbodiimide hydrochloride (EDC hydrochloride, 98 %), N-hydroxysuccinimide (NHS, 98 %), N-[N_{α},N_{α}-Bis(carboxymethyl)-L-lysine]-12-mercaptododecanamide (NTA (Nitrilotriacetic acid)-thiol, ≥ 90.0%), 11-mercaptoundecanol (MUO, 99 %), 11-mercaptoundecanoic acid (MUA, 95 %), 11-(ferrocenyl)undecanethiol (FcC_{11}, 95 %), and 1-dodecanethiol (DDT, ≥ 98 %) were purchased from MilliporeSigma, while 10-mercaptodecyl-ferrocenylcarboxamide (Fc-amide) was provided by Dr. Stephen Creager from Clemson University. EDC hydrochloride, NHS, MUO, MUA, and Fc-amide were stored at 4 ^{o}C, while NTA-thiol was stored at -20 ^{o}C, and DDT at room temperature.

Sodium phosphate monobasic (NaH_2PO_4, ≥ 99.0 %) and dibasic ($NaHPO_4$, ≥ 99.0 %) salts were used to prepare the phosphate buffer (PB, with the pH adjusted by the dropwise addition of concentrated NaOH solution). NaOH solutions were prepared by dropwise addition of H_2O to NaOH pellets (anhydrous pellets, ≥ 98 %) until the complete dissolution of the pellets was observed. Sodium perchlorate ($NaClO_4$, ≥ 98.0 %), 2-(N-morpholino)ethanesulfonic acid (MES buffer, ≥ 99 %), perchloric acid ($HClO_4$, 70 %, ρ = 1.664 g/mL), potassium ferrocyanide trihydrate ($K_4[Fe(CN)_6].3H_2O$, 98.5 – 102.0 %), and potassium ferricyanide ($K_3[Fe(CN)_6]$) were purchased from MilliporeSigma. MES was stored at 4 ^{o}C, while the remaining chemicals were stored at room temperature.

Biological materials, such as Lipopolysaccharide (LPS, phenol extraction), were purchased from MilliporeSigma, while Toll-like Receptor 4/Myeloid Differentiation Factor-2 (TLR4/MD-2, ≥ 95 %) was purchased from R & D Systems. Heat-killed *Salmonella typhimurium* (HKST) lysate

cells was purchased from Invitrogen. Lyophilized LPS and TLR4/MD-2 were stored at -20 and -80 ^{o}C, respectively. Reconstituted TRL4(MD-2) and HKST lysate cells were stored at -20 ^{o}C. Epoxy resin, used to fix the working area of Au coated slides, was prepared using Epon 828 (Technical Grade) from Toronto Research Chemicals and m-phenylenediamine (99 %) obtained from MilliporeSigma, both stored at room temperature in the dark.

3.2 Preparation and cleaning of electrodes

3.2.1 Au working electrodes

Thiolate SAMs were prepared on commercially available sputtered Au substrates. (Deposition Research Labs Inc.) by sputtering on clear Borosilicate Float Glass Microscope Slides (with the following dimensions: 25.4 mm x 76.2 mm x 1.1 mm) by first depositing a 40 nm Ti adhesion layer followed by a 100 nm Au layer. The literature suggests that such Au films are polycrystalline in nature, with a dominant (111) orientation [61], although this was never confirmed here. Each Au slide was cut into ~10 smaller pieces (with the following dimensions: 25.4 mm x ~5 mm x 1.1 mm) using a wet saw and immediately placed in H_2O (Ultrapure Type II, MilliQ) to wash away residue produced by grinding of the wet saw blade against the Au slide. These pieces (i.e., electrodes) were subsequently rinsed with absolute EtOH (100 %, Sigma-Aldrich) and acetone (ACS grade, Sigma-Aldrich), and then air dried. Approximately 10 µL of epoxy resin was applied on top of the flat Au surface to control the working area (i.e., where the SAMs were immobilized) of each Au electrode, giving an area of ca. 0.25 cm^2.

The epoxy resin was prepared with a 100:14 weight ratio of Epon 828 to m-phenylenediamine hardening agent, respectively. Epon 828 was dissolved by heating the mixture at ~40^{o}C in a water bath [146]. After its application, the epoxy resin was cured by heating at 80 ^{o}C

for 2 h, followed by heating at 120 ^{o}C for another 2 h, after which the Au electrodes were stored at room temperature in air.

Prior to use, the Au electrodes were sequentially rinsed with acetone, isopropanol (ACS grade, MilliporeSigma), absolute EtOH and H_2O. Cyclic voltammetry was used to determine the quality and the area of the working Au electrodes by collecting CVs in 0.5 M H_2SO_4 (reagent grade, MilliporeSigma) between 0.05 – 1.7 V vs. Reversible hydrogen electrode (RHE) at 100-500 mV/s, until the CVs overlayed each other, indicative of a clean electrode. The electrodes were then sequentially rinsed thoroughly with MilliQ H_2O and absolute EtOH, followed by drying with N_2(g), and then immersed in an ethanolic thiol solution. The electrochemically active surface area (ECSA) of Au was determined by dividing the integrated Au oxide CV reduction peak area by a 390 μC/cm^2 conversion factor [147] after a scan to 0.05 V vs. RHE

In this thesis work, two different versions of the electrochemical cleaning protocol described above were used. For most of Chapter 4, experiments were performed in a manner that minimally deviated from our earlier procedures [16,18], for reasons explained in Section 4.2. This method involved the re-use of the H_2SO_4 solution until a brown coloration was noticed (typically requiring up to a few weeks), probably indicative of organic material, most likely from the cleaning process of Au electrodes. When using this method, the Pt mesh counter electrodes were not cleaned often. In contrast, in most of Chapter 5, an alternative method for the electrochemical cleaning of the sputtered Au electrodes was devised, where fresh H_2SO_4 solution was used for each new experiment and the Pt mesh electrodes were also electrochemically cleaned prior to use.

3.2.2 Pt mesh counter electrodes

Pt mesh electrodes were cleaned by applying a constant potential of 1.7 V vs. RHE for 2 min, subsequently followed by collecting CVs between 0.1-1.4 V vs. RHE in 0.5 M H_2SO_4 at 100 mV/s for 20 cycles. The overlaying CV traces between cycles were considered indicative of a clean Pt mesh.

3.2.3 Reference electrodes

In this thesis, two different reference electrodes were utilized, RHE for electrochemical cleaning, and an Ag/AgCl double junction (MilliporeSigma) for the remaining electrochemical work. The RHE consisted of a Pt black electrode (i.e., Pt mesh electrodes that were platinized using a Yellow Springs Instrument platinizing kit (Model 3139)) immersed in H_2(g)-saturated 0.5 M H_2SO_4, connected to the electrochemical cell via a Luggin capillary. The Ag/AgCl reference electrodes were filled with and stored in saturated KCl solution.

3.3 Deposition of self-assembled monolayers (SAMs)

SAMs were prepared by submerging the working area of cleaned Au electrodes in 1 mM ethanolic thiol solutions for 24 h, where the SAM composition was presumed to mimic the dissolved thiol molar composition. For example, ethanolic solutions containing 5 % (v/v) 1 mM Fc-amide, 30 % (v/v), 1 mM MUA and 65 % (v/v) 1 mM MUO were anticipated to form 5 % Fc-amide / 30 % MUA / 65 % MUO SAMs [61]. It was also assumed that these multi-component SAMs were distributed homogeneously on the Au surface.

The preparation and usage of ethanolic thiol solutions varied between Chapters 4 (minimal deviation from our prior procedure [16,18]) and 5 (newer procedure). The earlier procedure

involved storing a stock 1 mM ethanolic thiol solutions at 4 ^{o}C after preparation and using it until it was depleted (which could take up to a few months). The newer procedure utilized fresh 1 mM ethanolic thiol solutions, prepared immediately prior to SAM deposition.

3.4 Sensor construction

3.4.1 Sensors prepared using carboxylic-acid containing SAMs

In Chapter 4, TLR4-based sensors were prepared by modification of ternary SAMs prepared using ethanolic solutions containing 5 % (v/v) 1 mM Fc-amide, 30 % (v/v) 1 mM MUO and 65 % (v/v) 1 mM MUA. The carboxylic acid terminated component (i.e., MUA) was activated via carbodiimide chemistry, followed by amide bond formation that results in the attachment of a terminal NHS leaving group. This was done by immersing the SAMs in a freshly prepared mixture containing 2 mg EDC, 5.5 mg NHS, and 108 mg MES in 5 mL MilliQ H_2O. The NTA groups were covalently attached to the SAMs by immersion of NHS-terminated SAMs in a freshly prepared 1 mM NTA-lysine solution for 20 h at 4 ^{o}C in the dark. The resultant SAMs chelate Ni^{2+} after a 20 min immersion in 0.1 M $NiSO_4$, prepared immediately prior to use.

TLR4 immunoproteins were immobilized via formation of coordination bonds between the 10-Histidine Tag of the protein and Ni^{2+}, achieved by immersion of Ni^{2+}-terminated SAMs in a recently thawed 5 µg/mL TLR4/MD-2 solution. Each TLR4/MD-2 aliquot of reconstituted solution was used for a maximum of five freeze-thaw cycles. Every modification step was performed in 1.7 mL polypropylene microcentrifuge tubes, a procedure taken from previous Birss group papers [16,18]. These steps are also shown in Figure 3.1.

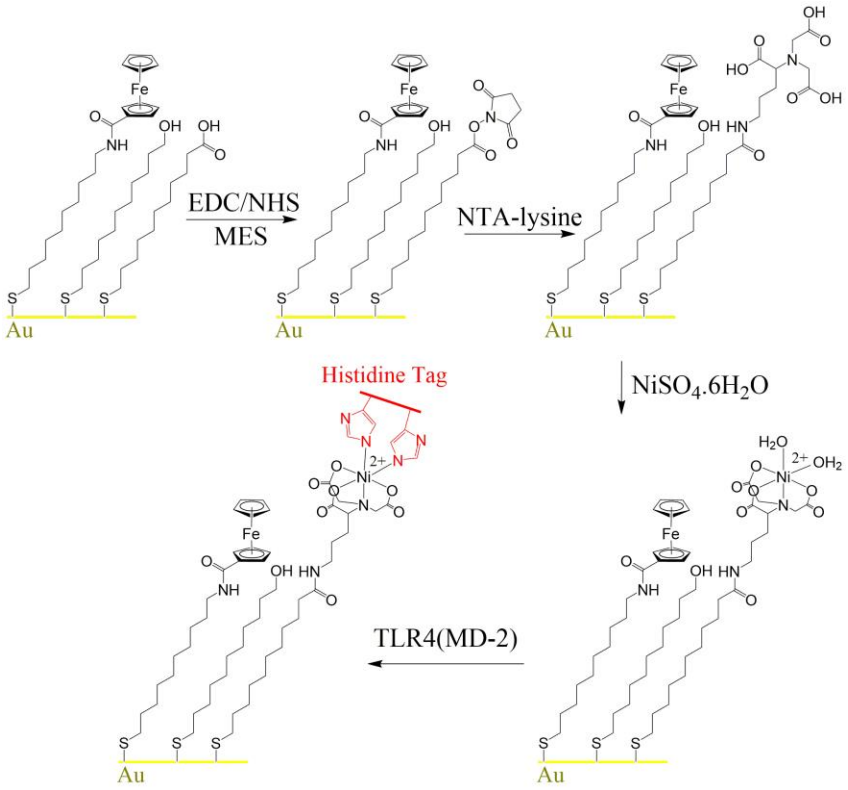

Figure 3.1: Schematic of the sensor construction process used for TLR4 immunoprotein immobilization on ternary SAMs (5 % (v/v) 1 mM Fc-amide, 30 % (v/v) 1 mM MUA, and 65 % (v/v) 1 mM MUO) in Chapter 4. In this process, carbodiimide activated carboxylic acid was used to covalently attach an NHS leaving group, which departed in the presence of NTA-lysine that chelated Ni^{2+}, which, in turn, formed an ionic bond with the poly-Histidine Tag of the protein. Charge-compensating anions in the proximity of Ni^{2+} were not included for sake of simplicity.

3.4.2 Sensors prepared using nitrilotriacetic-acid containing SAMs

In Chapter 5, TLR4-based sensors were constructed by modification of ternary SAMs prepared using ethanolic solutions containing 5 % (v/v) 1 mM FcC_{11}, 30 % (v/v) 1 mM NTA-thiols and 65 % (v/v) 1 mM MUO. Ni^{2+} was chelated by immersion of the NTA-terminated SAMs in 1 mM NaOH for 5 min (to ensure deprotonation of its carboxylic acid groups), then immersing the SAMs in 0.2 M $NiSO_4$ for 1 h. TLR4/MD-2 immunoprotein was immobilized by immersion of the Ni^{2+}-terminated SAMs in recently thawed TLR4/MD-2 solutions for 24 h. Each protein

aliquot was never reused after a single freeze-thaw cycle. Every modification step was performed in a 1.7 mL polypropylene microcentrifuge tube. These steps are also shown in Figure 3.2.

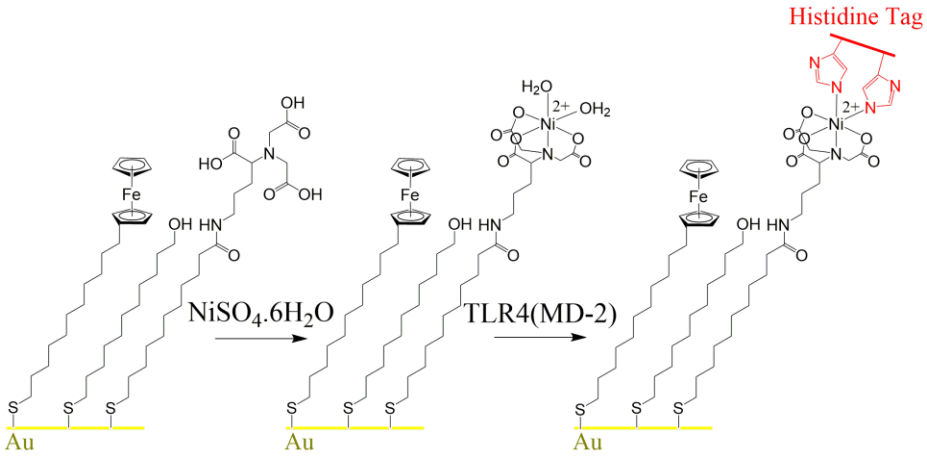

Figure 3.2: Schematic of the sensor construction process used for TLR4 immunoprotein immobilization on ternary SAMs (5 % (v/v) 1 mM FcC_{11}, 30 % (v/v) NTA-thiol and 65 % (v/v) 1 mM MUO) in Chapter 5. In this process, the terminal NTA group chelated Ni^{2+}, which formed an ionic bond with the poly-Histidine Tag of the protein. Charge-compensating anions in the proximity of Ni^{2+} were not included for sake of simplicity.

3.5 Electrochemical methods

3.5.1 Electrodes

In this thesis, three electrode electrochemical cells were comprised of a working electrode (WE), counter electrode (CE) and reference electrode (RE, against which the potential of the WE is measured). Au electrodes were always utilized as the WE (except when Pt mesh electrodes were cleaned) and were connected to the potentiostat using crocodile clips in a manner such that the clip was not in contact with the electrolyte solution. The working area of the Au WE was controlled at ca. 0.25 cm^2 with the application of epoxy resin on top of the Au deposited surface of the planar electrodes. Pt mesh (99.9 % pure, Alfa-Aesar) with an area of 4 cm^2 was used as the CE throughout this thesis work.

A Reversible Hydrogen Electrode, consisting of a Pt black electrode placed in H_2(g)-saturated 0.5 M H_2SO_4, was the RE used during Au WE and Pt mesh electrochemical cleaning in the same solution composition. The remaining electrochemical testing in this thesis work utilized a double-junction Ag/AgCl (MilliporeSigma, filled and stored with saturated KCl solution) as the RE.

3.5.2 Electrochemical cell

Au and Pt mesh electrode cleaning was performed in a two-compartment cell, as shown in Figure 3.3a. The RHE was connected to the primary cleaning cell containing either the Au or Pt mesh WE and the Pt mesh CE. Electrochemical testing was performed in a single compartment cell with three necks (one for each electrode), where the middle neck held the Au WE, and the two side necks held the Ag/AgCl RE and Pt mesh CE, as shown in Figure 3.3b. The electrolyte solution was bubbled with N_2(g) for 20 min prior to electrochemical cleaning and testing to minimize the presence of O_2(g). Inert atmosphere was maintained within the electrochemical cell by passing N_2(g) continuously over the solution surface in the electrochemical cell throughout the duration of the experiment. Solutions were never stirred during or prior to experiments.

3.5.3 Electrochemical instrumentation

Electrochemical experiments in this thesis work were performed using a SP-300 BioLogic potentiostat. The EC-Lab software, also provided by BioLogic, was used to instruct the potentiostat to conduct experiments using techniques such as cyclic voltammetry (CV) and electrochemical impedance spectroscopy (EIS) and perform data analysis (i.e., integration of CV

peaks). The raw data were often converted to spreadsheet format and transported to OriginPro 8.5 plotting software.

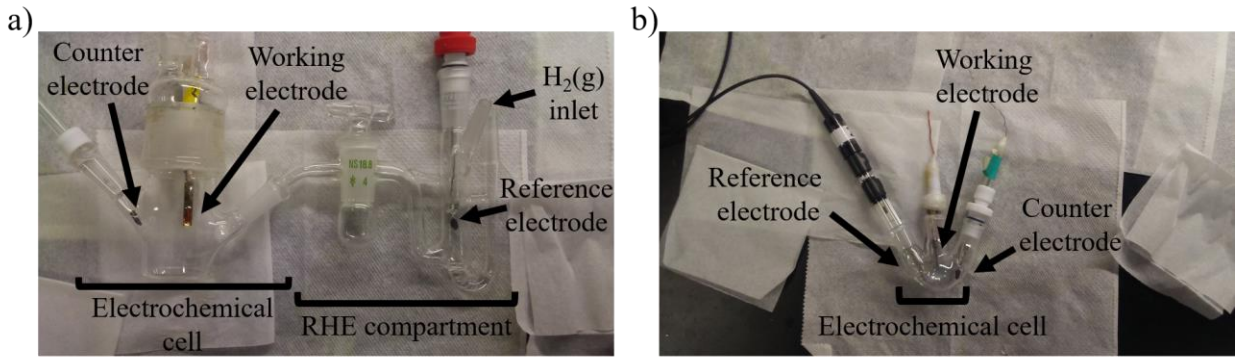

Figure 3.3: The two-compartment cell used for electrochemical cleaning of electrodes is shown in panel (a) and the single compartment electrochemical cell used for sensor testing is shown in panel (b).

3.5.4 Experimental conditions

3.5.4.1 EIS studies of the WE

The current passed at the WE/electrolyte interface was measured using EIS. In most of Chapter 4, the EIS data were collected in 5 mM $K_4[Fe(CN)_6]$ + 0.2 M PB (pH 7.0) at 0.3 V vs. Ag/AgCl, chosen because this is approximately in the 'foot of the voltammetric wave' region (refer to Section 4.1.2), using frequencies of 10^5 to 10^{-1} Hz with an AC perturbation of 10 mV root-mean squared (rms). In Section 4.6, EIS data were collected in electrolyte solutions containing increasing concentrations of $K_3[Fe(CN)_6]$ along with 5 mM $K_4[Fe(CN)_6]$ + 0.2 M PB (pH 7.0). In Chapter 5, EIS data were collected at various potentials that were all also approximately in the 'foot of the voltammetric wave' region. A cartoon version of a typical impedance spectrum collected in this present work is shown in Figure 2.9.

3.5.4.2 Exposure of sensors to biological species

In Chapter 4, sensors were exposed to HKST lysate cells, which was added to the 10 mL electrolyte solution within the single compartment cell, with volumes ranging from 1-10 µL of stock microorganism concentrations of 10^4-10^{10} cells/mL. This was immediately followed by mixing with a micropipette and bubbling with N_2(g) for 20 min prior to, but not during, testing. In Chapter 5, sensors were exposed to LPS by dropwise addition of 0.32-5000 µg/mL solutions, using a 100 µL micropipette, to the working area surface of the Au WE. The drop was incubated on this electrode for 20 min, and then the electrode was transferred to the electrochemical cell for testing.

3.5.4.3 Electrochemistry of Ferrocenyl-thiolate self-assembled monolayers

In Chapter 4, CVs of Fc-thiolate SAMs were collected in 0.2 M PB (pH 7.0) from 0.1-0.7 V vs. Ag/AgCl at sweep rates of 100-500 mV/s. In Chapter 5, CVs were collected in 0.2 M PB (pH 7.0) containing varying concentrations of $NaClO_4$, and 1 M $HClO_4$ from 0-0.7 V vs. Ag/AgCl at sweep rates of 100-2000 mV/s. A typical Fc-thiolate SAM CV collected in this present work is shown in Figure 2.6, along with the discussion of associated redox reactions in Section 2.6.1.

3.5.4.4 Electrochemical mediation CV experiments

In Chapters 4 and 5, CVs of Fc-thiolate SAMs were collected in 5 mM $K_4[Fe(CN)_6]$ + 0.2 M PB (pH 7.0) from 0.1-0.7 V vs. Ag/AgCl at sweep rates of 100-500 mV/s. A typical mediation CV collected in this present work is shown in Figure 2.6b, along with the discussion of the associated redox reactions in Section 2.6.1.

3.6 Error Analysis

The most consistent and prevalent sources of error in this work is expected to be the lab glassware and equipment, electrochemical instrumentation, and the precision between batches of biological material. Stock solutions of 0.2 M PB (pH 7.0), and 1 M $NaClO_4$ and $HClO_4$ were prepared using 100-500 mL volumetric flasks (with error values ranging from 0.15-0.80 mL). The bench-top pH meters (SevenCompact Duo purchased from Mettler Toledo), used to adjust the pH of buffered solutions, had an accuracy of ± 0.001 pH unit. The analytical balance (Jewelry Balances from Optika Italy), used to measure the masses of Na_2HPO_4, NaH_2PO_4, and $NaClO_4$, had an error of ± 0.10 mg. Electrolyte solutions of 5 mM $K_4[Fe(CN)_6]$ and varying concentrations of $K_3[Fe(CN)_6]$ were prepared using a 25 mL graduated cylinder, with an error of ± 0.06 mL [148].

In the range of the measured current values, the SP-300 potentiostat has an error of < ± 0.1 %. The error in potential control is < ± 1 mV. According to the EIS contour plot, in the range of resistance values measured, the error is ± 0.3 % at both low (1 Hz) and high frequencies (10^5 Hz) for the range of resistance values encountered in this work [149].

Differences in the activity of biological material between batches were unaccounted for. The addition of HKST lysate cells to the electrochemical cell and LPS to the surface of the Au WEs was done using micropipettes that typically have an error of ± 1 % [148].

Chapter four: Sensor construction, testing protocols and characteristics of sensor drift

4.1 Introduction to TLR-based sensors constructed from Ferrocenyl-thiolate self-assembled monolayers

In previous work [16,18], the Birss group has designed a series of electrochemical Toll-like Receptor 4 (TLR4)-based biosensors that were shown to respond sensitively and selectively to the lipopolysaccharides (LPS) endotoxin component of Gram-negative bacteria, such as heat-killed *Salmonella typhimurium* (HKST). These sensors were constructed by the bonding of Ferrocene-modified alkanethiolate Self-assembled Monolayers (SAMs), composed of three distinct alkanethiolate molecules, on Au electrodes. This was followed by carbodiimide coupling in order to attach the nitrilotriacetic acid (NTA) group, with one of the thiols having a terminal redox-active Ferrocene (Figure 4.1), typically deposited at ~5 % surface coverage. The NTA group was then coordinated to Ni^{2+}, which can further coordinate with the polyhistidine-tag of the recombinant human TLR4 immunoprotein. The full fabrication of this biosensor is shown in Figure 3.1.

4.1.1 Composition of ternary SAMs

The alkanethiolate molecules used to prepare the three-component SAMs (ternary SAMs) for this TLR4 sensor were (10-mercapto-N-decyl)ferrocenecarboxamide (Fc-amide), 11-mercaptoundecanoic acid (MUA), and 11-mercaptoundecanol (MUO), as displayed in Figure 4.1 [18]. These ternary Fc-amide SAMs were prepared by immersing an electrochemically cleaned, polycrystalline, sputtered (on glass) Au electrode in an ethanolic thiol solution containing 5% (v/v) 1 mM Fc-amide, 30% (v/v) 1 mM MUA and 65% (v/v) 1 mM MUO, resulting in a thiol mixture composed of 0.05 mM Fc-amide, 0.30 mM MUA and 0.65 mM MUO [18,143]. It was assumed

that the SAM composition on the Au surface will reflect the relative concentrations of the three thiols in the deposition solution and that the thiols would distribute themselves uniformly on the Au surface, rather than forming domains of each thiol, although these hypotheses have not been verified as yet. The projected area occupied by the TLR4/MD-2 complex is 55 nm^2 (calculated using the dimensions mentioned in Section 2.4.4, specifically 7.7 nm x 7.2 nm). This protein area, when compared to the footprint of a single alkanethiol in well-packed alkanethiolate SAMs (i.e., 0.2 nm^2 [65]), indicates that ~2 % of the monolayer should be capable of chelating Ni^{2+} for purposes of immobilizing proteins with a 10 His-Tag (assuming five Ni^{2+} ions chelate to each 10 His-Tag on the TLR4 protein).

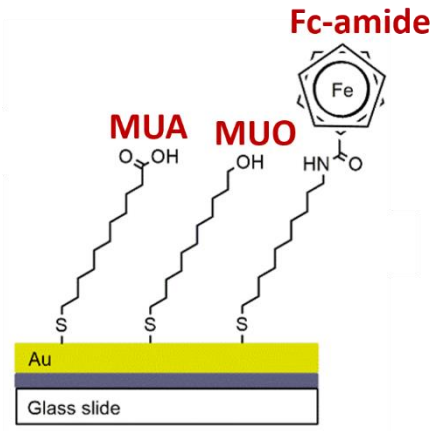

Figure 4.1: Cartoon of ternary Fc-amide SAMs composed of 11-mercaptoundecanoic (MUA), 11-mercaptoundecanol (MUO), and (10-mercapto-N-decyl)ferrocenecarboxamide (Fc-amide).

The purpose of the Fc-amide thiol was to serve as a redox mediator when its terminal Fc-moiety was oxidized (Reaction 4.1), as ferrocenium (Fc^+) mediates the oxidation of solution-based redox species, converting $Fe(CN)_6^{4-}$ to $Fe(CN)_6^{3-}$ (Reaction 4.2), with this producing a mediation current during electrochemical testing, as was previously described in Section 2.6.1. The overall reaction during redox mediation is shown below:

$$Fc \rightleftharpoons Fc^{+} + e^{-} \qquad \text{Reaction 4.1}$$

$$Fc^{+} + Fe(CN)_6^{4-} \rightleftharpoons Fc + Fe(CN)_6^{3-} \qquad \text{Reaction 4.2}$$

The second thiol, MUA, contains a terminal carboxyl (-COOH) group, which was further chemically modified to allow the immobilization of the TLR4 immunoprotein, as mentioned above and shown in Figure 3.1. The third thiol is MUO, which serves as a spacer, with its main purpose being to minimize Fc-Fc lateral interactions, avoiding these interactions should produce better immobilized-Fc electrochemistry, and also should prevent fouling caused by non-specific interactions, which are deleterious to the specificity of biosensors [18,143].

4.1.2 Electrochemical testing protocol

The detection of HKST bacterial lysates by the TLR4-based sensor was typically carried out by adding various concentrations of HKST to a solution containing 5 mM $K_4[Fe(CN)_6]$ and 0.2 M PB (pH 7.0), with the mechanism of detection proposed to be due to the dimerization of immobilized TLR4 after interaction with the LPS molecules released by HKST lysates. This was proposed to cause a small degree of blocking of the underlying Fc moieties, resulting in inhibited access of the $Fe(CN)_6^{4-}$ species to the Au and an increase in sensor resistance, as is commonly observed in the literature [14,18,105,150]. The proposed blocking of the underlying Au/SAM to solution-phase redox-active ions is measured using electrochemical techniques, including electrochemical impedance spectroscopy (EIS) and cyclic voltammetry (CV), where EIS gives the charge transfer resistance (R_{CT}). As a result of TLR4 dimerization, an increase in R_{CT} was expected and is indeed observed, resulting in an increase in R_{CT} as a function of increasing HKST lysate concentration. It is important to note that the potential of the working electrode is reported vs. the Ag/AgCl (saturated KCl) reference electrode throughout this chapter.

In this work, the sensor response was always first examined electrochemically in 0.2 M PB (pH 7.0) to track the electrochemical characteristics of the Fc-containing SAMs, such as double-layer capacitance (C_{dl}), the Fc redox peak potential (E_p), and the charge in the Fc redox peaks, which is assumed to give surface coverage of the redox-active Fc-containing thiol (Γ_{Fc}), as shown in Figure 4.2a. These characteristics were obtained from CVs collected sequentially at 100, 250, and 500 mV/s, with 3 cycles at each sweep rate (scan rates outside of this range produced noisy and/or poorly-defined CV peaks). Figure 4.2a displays an example of the second CV cycles and the parameters that were tracked, as well as the potential that was used for the EIS studies (E_{EIS}).

In Figure 4.2, Faradaic current is observed to flow from 0.2 - 0.55 V, where the anodic and cathodic peaks are due to the oxidation and reduction of Fc to Fc^+ and Fc^+ to Fc, respectively. Subtracting the baseline current (using EC lab software) gives the anodic (Q_{an}) and cathodic (Q_{cat}) Fc peak charges, which should be identical (Q). Dividing by the Faraday constant and the true Au electrode surface area, obtained from the Au oxide CV reduction charge [147], is assumed to equate to the amount of Γ_{Fc} on the surface in moles/cm^2 [114]. The average peak potential (E_p) was taken as the mid-point between the anodic ($E_{p,a}$) and cathodic ($E_{p,c}$) peak potential values [114].

Non-Faradaic double-layer charging currents are also observed in Figure 4.2, with the interfacial capacitance typically calculated in our work from the current passed at 0.1 V, as this is roughly in the middle of a potential range that contains no interferences from any redox reactions. The double layer current (i_{dl}) is known to be linear with sweep rate [114], and depends on the thickness and orientation of the SAMs [114,141,151,152]. It is notable that the charging currents are larger at potentials positive of the Fc redox peaks (0.55-0.7 V), likely due to the presence of

cationic Fc^+ and potential-induced defects. This will lead to a larger population of anions in the double layer, increasing the magnitude of the charging current [151].

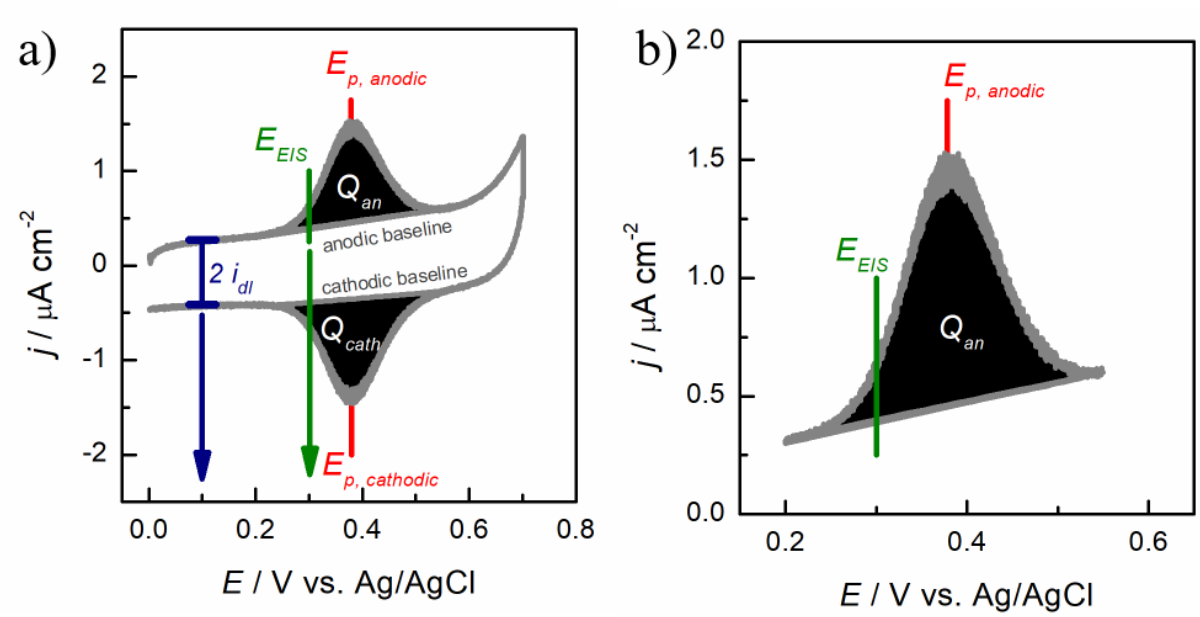

Figure 4.2: (a) CV scan of ternary Fc-amide SAMs in 0.2 M PB (pH 7.0) at 100 mV/s. The horizontal grey line from 0.2 – 0.6 V is the anodic and cathodic baseline (generated artificially using graphing software Origin) used to calculate the integrated Faradaic charge (black area) of the oxidation of Fc to Fc^+ (Q_{an}) and the reverse reduction reaction, respectively. The red lines at ~ 0.4 V are the anodic ($E_{p,\ anodic}$) and cathodic ($E_{p,\ cathodic}$) peak potentials of the oxidation and reduction reactions, respectively. The green arrow at 0.300 V is the polarization potential at which EIS is performed (E_{EIS}). The blue arrow at 0.100 V indicates the potential at which the double-layer current of the SAMs was measured before oxidation of Fc. In (b), a close up of the anodic peak of the sample CV in (a) is shown.

Following these CV studies in 0.2 M PB (pH 7.0), electrochemical mediation studies of the SAMs were carried out in 0.2 M PB (pH 7.0) containing 5 mM $Fe(CN)_6^{4-}$, as shown in Figure 4.3a. These CVs were performed at the same sweep rate and approximately over the same potential range as in the PB solution alone (Figure 4.2). As explained in Section 2.6.1, the more positive potential of the immobilized Fc/Fc^+ (~0.4 V) vs. that of $Fe(CN)_6^{4-}/Fe(CN)_6^{3-}$ (~0.23 V) results in the 'mediation CV' displayed in Figure 4.2. Under these conditions, the rising anodic current, starting at ~0.2 V, is due to the oxidation of $Fe(CN)_6^{4-}$ to $Fe(CN)_6^{3-}$, mediated by Fc^+ (Reaction

4.2) [139,143], with the reaction initially kinetically controlled and then diffusion controlled at > 0.4 V [17,139,143].

At the 'foot of the voltametric wave', the $Fe(CN)_6^{4-}$ oxidation reaction is fully kinetically controlled [18,140] and thus the Butler-Volmer equation should apply. Figure 4.3b shows a Tafel plot (black trace) generated in this region (~0.05 to 0.275 V, where the currents are < 10 % of the current peak). The Tafel slope, calculated from the inverse of the slope of this plot, is 89 ± 4 mV/decade (N = 3). Electrochemical mediation investigated by Creager *et al*. showed that Tafel slopes of binary Fc-amide SAMs should vary from 59 to 118 mV/decade as a function of $Fe(CN)_6^{4-}$ concentration and applied potential [139]. The theoretical transfer coefficient from the Butler-Volmer equation is calculated using Equation 4.1, where γ is the number of electrons transferred prior to the rate-determining step (RDS), ν is the stoichiometry of the RDS, r is the number of electrons transferred during the RDS, and β is the symmetry factor (which is typically equal to 0.5) [143].

$$\alpha = \frac{\gamma}{\nu} + r\beta \qquad \text{Equation 4.1}$$

When the transfer coefficient values are equal to 0.5 and 1.0, then T.S. values are equal to 118 and 59 mV/decade, respectively, which corresponds to either Reaction 4.1 (i.e., the oxidation of Fc to Fc^+) or Reaction 4.2 (i.e., the cross-reaction between $Fe(CN)_6^{4-}$ and Fc^+) being the RDS [17]. Comparing these calculated T.S. values with experimental T.S. values helps to identify the RDS. When the Tafel slope is between the two values, this indicates that the (RDS) is transitioning between the second chemical step, i.e., the cross-reaction between $Fe(CN)_6^{4-}$ and Fc^+ (Reaction 4.2), to the first electron transfer step, i.e., the oxidation of Fc (Reaction 4.1) [139,143]. Our Tafel slope value of ca. 90 mV indicates that, at this sweep rate, the kinetics are moving from being

controlled by Reaction 4.2 to Reaction 4.1, similar to what was obtained by Creager *et al.* [139,143].

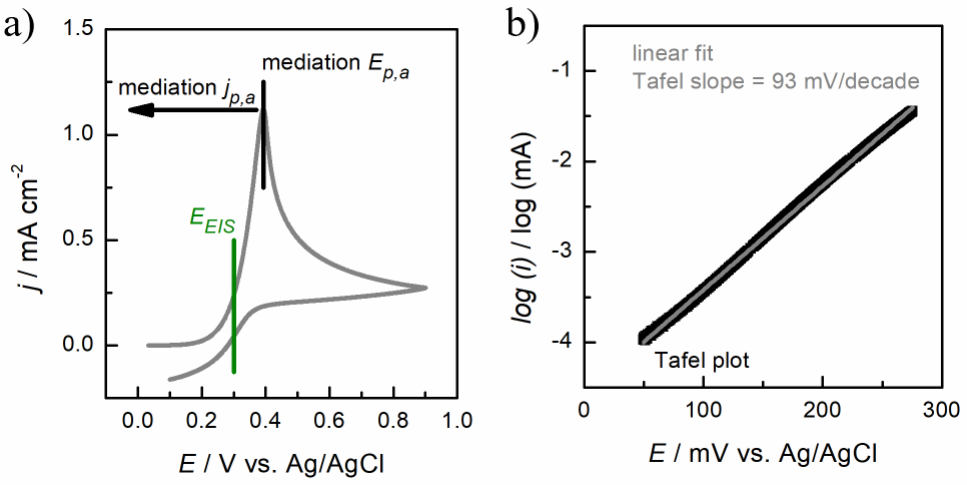

Figure 4.3: Mediation electrochemistry of ternary Fc-amide SAMs. In (a), a sample CV of the SAM in 5 mM $K_4[Fe(CN)_6]$ and 0.2 M PB (pH 7.0) at 100 mV/s is shown, where the mediation CV peak potential ($E_{p,a}$, ~0.4 V) and peak current density ($j_{p,a}$) is shown using the black arrow. EIS is performed negatively of the peak potential at the "foot" of the mediation CV at 0.300 V. In (b), the Tafel plot (black) extracted from the sample CV in (a) and the slope of its linear fit (grey) are shown.

In our prior work and in the results shown in the next section, an important electrochemical technique used to assess sensor performance is shown to be EIS. This technique works best if electrochemistry is kinetically controlled and thus the potential in our EIS work was set at 0.3 V, as this is in the range of the foot of the voltammetric wave (Figure 4.3a) [18,139]. A sample Nyquist plot obtained at 0.3 V over a frequency range from 1 MHz to 0.1 Hz, performed in the solution used for the mediation studies (Figure 4.3a), is shown in Figure 4.4. A large frequency range was utilized to ensure the completion of the semicircle (the diameter gives the charge transfer resistance, as displayed by the red line), which is followed by a ~45^o line, characteristic of the

Warburg diffusion element at low frequencies (blue box). The diffusion element in this figure is noisy due to trace convection that is irregular.

Monitoring the increase in the charge-transfer resistance of the TLR4-based sensor with exposure to various concentrations of HKST bacteria lysates has been the main analytical approach used to date in our TLR4-based sensor work [18]. The sensor response to HKST lysates is also observable from the mediation CVs, as there is a simultaneous increase in the peak potential and a decrease in peak current [18].

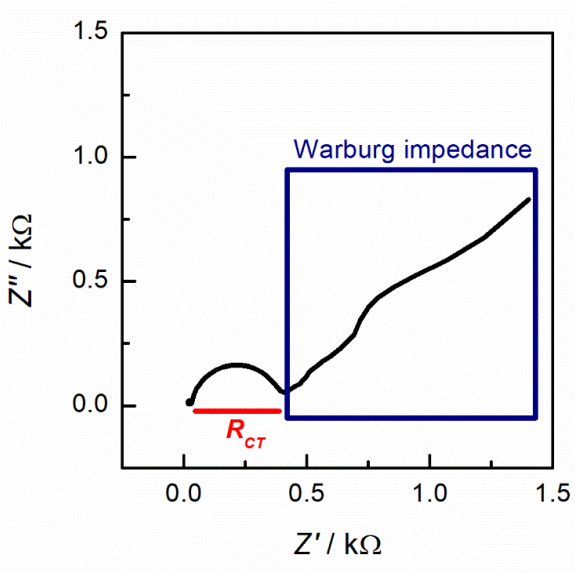

Figure 4.4: Nyquist plot of ternary Fc-amide SAMs with data collected at 0.300 V and frequencies ranging from 1 MHz to 0.1 Hz in 5 mM $K_4[Fe(CN)_6]$ + 0.2 M PB solution (pH 7.0). The diameter of the semicircle at high frequencies gives R_{CT} (red) and the 45° line (blue box) at low frequencies is due to the Warburg impedance.

Our electrochemical testing protocol involved performing EIS, immediately followed by the successive collection of three 'mediation CVs' between 0.1 and 0.7 V at 100, 250, and 500 mV/s, consistent with previous work [18,143]. This was carried out after a 20 min incubation period at the open circuit potential (OCP) following the addition of aliquots of HKST lysate

bacteria to the 5 mM $Fe(CN)_6^{4-}$ + 0.2 M PB (pH 7.0) solution, such that the overall experiment time (including periods during which electrodes were polarized and incubation periods at the OCP) for each sensor was 120 min.

Using these electrochemical evaluation techniques, our sensor has been shown to be responsive to HKST lysates, instead of merely cell wall components of HKST lysates, such as purified lipopolysaccharide (LPS), giving them real-world applicability. Furthermore, the linear dynamic range of our sensor was shown to be 10^0 – 10^5 cells/mL, which is a very relevant concentration range for human health [15,18]. However, there are still a number of challenges with these sensors, including poor sensitivity, as the R_{CT} changes depend only weakly on the log of HKST lysate concentration. Also, the sensors have demonstrated drift issues, i.e., the sensors have shown an increase in charge-transfer resistance (R_{CT}) even in the absence of HKST cell lysates, with the changes in R_{CT} being similar in magnitude to the response of the sensor to HKST cell lysates. Drift is a serious problem for a sensor, especially if the magnitude of the drift is anywhere near that of the change in signal when the analyte concentration is altered, a situation that would make the sensor of little value.

However, it was difficult to know where the drift problem originates because the TLR4 based sensor is quite complex, involving three components in the SAM, two linking layers and the TLR4 immunoprotein itself. Thus, the rest of Chapter 4 is focused on understanding the characteristics of the drift of our sensors and ultimately determining its cause and solving this problem in Chapter 5. To understand the causes of sensor drift in this chapter, multiple variables were altered, including the addition of a reducing agent to the thiol precursor solution to determine whether the problem was related to thiolate oxidation, altering the concentration of Fc-amide in the thiol precursor solution to change the coverage of the Fc thiols in the SAM, and varying the

time of exposure of the SAMs to the 5 mM $Fe(CN)_6^{4-}$ + 0.2 M PB (pH 7.0) electrolyte testing solution and OCP conditions.

4.2 Comparison of magnitude of electrochemical response to HKST lysate cells and magnitude of drift of TLR4-based sensors using EIS and mediated CV

Typical Nyquist plots (EIS) and the second mediation CV (100 mV/s) are shown in Figure 4.5 for a complete sensor exposed to 10^0, 10^1, 10^2, 10^3, 10^4, and 10^5 HKST cells/mL. In Figure 4.5a, the charge-transfer resistance values, extracted first under baseline conditions (i.e., at t = 0 min which is prior to HKST lysate exposure) and then after the addition of various HKST concentrations up to 10^5 lysate cells/mL, are seen to increase from 560 ± 225 initially to 908 ± 351 Ω at the end, with three sensors tested for each HKST concentration and included in these average values (N = 3). While exposure to increasing concentrations of HKST lysate results in a continuous increase in charge-transfer resistance, for simplicity, only the difference in R_{CT} between the baseline (0 lysate cells) and 10^5 lysate cells/mL is reported, given here as $\%\Delta R_{CT}$.

The results shown in Figure 4.5 give a $\%\Delta R_{CT}$ value of 60 ± 18 %. This is very similar to earlier results obtained with the same sensor composition and preparation, which gave an increase in the R_{CT} values from 513 Ω to 903 Ω for 0 and 10^5 HKST lysate cells/mL respectively, showing very good sensor reproducibility and giving a $\%\Delta R_{CT}$ value of 76 % (N = 1) [18,143]. It should be noted that, in much of the rest of this thesis, the $\%\Delta R_{CT}$ values obtained from an analysis of solutions containing 0 to 10^5 lysate cells/mL are typically reported, facilitating a comparison of sensor response under different conditions.

Our group has also shown [18,143] that the sensor response can be monitored by the changes in CV peak current ($i_{p,a}$) and potential ($E_{p,a}$) with the addition of HKST to the cell solution

(Figure 4.5b). Again, considering only the baseline (no HKST, black) and 10^5 HKST lysate cells/mL data (red), these values are 134 ± 18 µA at 339 ± 18 mV and 119 ± 16 µA at 359 ± 12 mV, respectively. The corresponding change obtained is -10 ± 13 and 6 ± 2 % respectively. The mediation CVs were collected after each EIS experiment and hence there is some accumulation of $Fe(CN)_6^{3-}$ near the electrode surface, which explains the differences in CV shape between these mediation CVs and the one shown in Figure 4.3a. The first and second columns of Table 4.1 summarize the changes in the R_{CT} and CV peak parameters of the Birss group's published work [18,143], as well as the results shown here when the HKST concentration was increased from 0 to 10^5 HKST cells/mL.

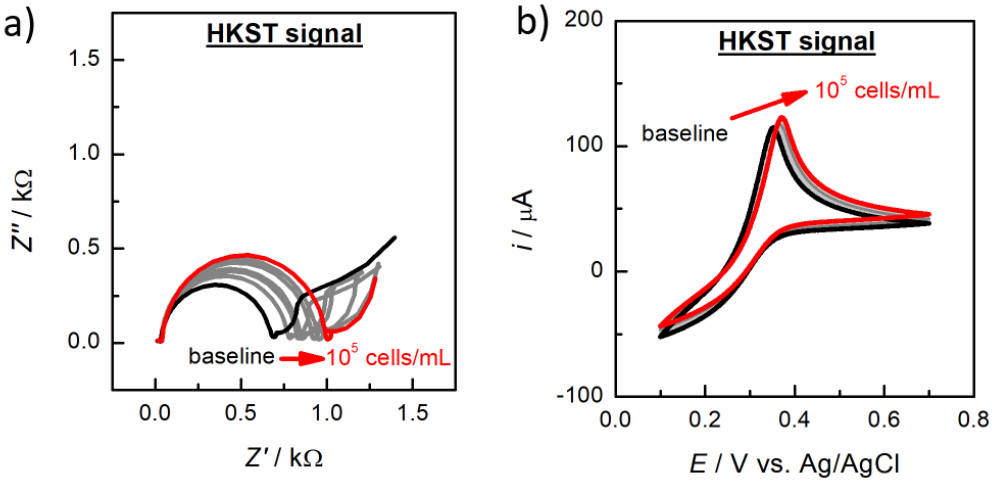

Figure 4.5: Electrochemical signal response of a TLR4-based sensor baseline (black) to 10^0-10^4 HKST cells/mL (grey) and 10^5 HKST (red) lysate cells/mL. Increasing concentrations of HKST were added every 20 min for 120 min to the solution containing 5 mM $K_4[Fe(CN)_6]$ + 0.2 M PB (pH 7.0). In (a), the Nyquist plots were collected at 0.300 V at frequencies ranging from 1 MHz to 0.1 Hz. In (b), the mediation CVs wave collected at 100 mV/s following EIS testing.

To demonstrate why drift of these sensors is a significant problem, even without any HKST lysates present, Figure 4.6 shows a typical set of Nyquist plots (EIS) and mediation CVs (100 mV/s) for a sample sensor exposed to blank PB solutions containing 0 HKST lysate cells/mL for

various times. It is seen that the sensor response changes in a manner very similar to what is shown in Figure 4.5 with increasing HKST concentration. The t = 0 min (baseline) measurement gives an R_{CT} of 597 ± 74, while this has increased dramatically to 1025 ± 22 Ω after 120 minutes, all at the OCP, equating to an $\%\Delta R_{CT}$ of 59 ± 15% (N = 2). Similarly, the mediation CV peak currents and potentials also change, with the peak current dropping from 118 ± 5 µA at 341 ± 16 mV to 103 ± 13 µA at 363 ± 11mV over 120 min, corresponding to $\%\Delta E_{p,a}$ = 6 ± 2 and $\%\Delta i_{p,a}$ = -12 ± 15 % (third column of Table 4.1).

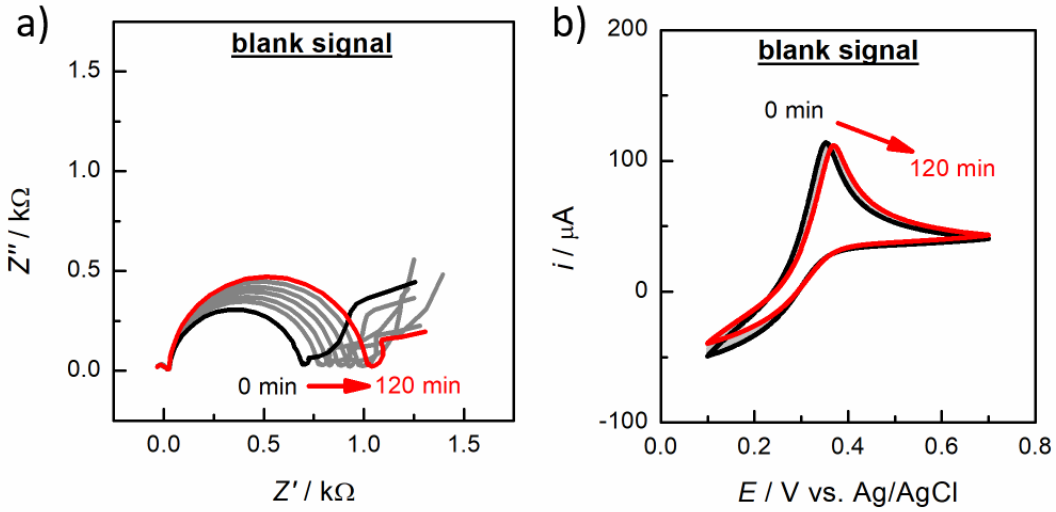

Figure 4.6: Electrochemical drift of a TLR4-based sensor at t = 0 min (black), 20 – 100 min (grey) and 120 min (red). Aliquots of the PB solution (i.e., solutions not containing HKST lysate cells) were added as a control test every 20 min for 120 min to the solution containing 5 mM $K_4[Fe(CN)_6]$ + 0.2 M PB (pH 7.0). In (a), the Nyquist plots were collected at 0.300 V at frequencies ranging from 1 MHz to 0.1 Hz. In (b), the mediation CVs were collected at 100 mV/s following each EIS experiment shown in (a).

Table 4.1 compares the changes in the EIS and mediation CV parameters after increasing the exposure from 0 to 10^5 HKST lysate cells/mL (Figure 4.5), as well as the electrochemical signal drift observed over 120 min in a solution containing 0 cells/mL (Figure 4.6). By comparing the second and third columns, it is seen that the magnitude of change in R_{CT} is similar in both

cases. This raises the question as to whether the changes seen in Figure 4.5 were due to a response to HKST lysates or just due to sensor drift. To determine the origin of the drift problem, the focus was placed first on the stability of the underlying thiol SAMs, due to their known propensity to desorb via oxidation of thiols. For this work, the same type of ternary Fc-amide SAMs was deposited and studied electrochemically, but without further sensor assembly.

Table 4.1: Magnitude of EIS and CV signal change of a fully assembled TLR4 sensor when exposed to 10^5 HKST cells/mL from literature data (1st column [1]) and from the current work (2nd column). The 3rd and 4th columns show the magnitude of signal drift over 120 min for the TLR-4 sensor in 0 HKST cells/ml and for the ternary Fc-amide SAMs alone, respectively.

	Published TLR4-sensor R_{CT} change with HKST lysate exposure (N = 1) [1]	**TLR4-sensor R_{CT} change with HKST lysate exposure (N = 3)[2]**	**TLR4-sensor signal drift (N =2)[3]**	**Ternary Fc-amide SAM signal drift (N=3)[4]**
$\%\Delta R_{CT}$	76 %	60 ± 18 %	59 ± 15 %	43 ± 9 %
$\%\Delta E_{p,a}$	-	6 ± 2 %	6 ± 2 %	1 ± 3 %
$\%\Delta i_{p,a}$	-	-10 ± 13 %	-12 ± 15 %	-9 ± 6 %

1. Results taken from Birss group's published results [18].
2. An example of these results is shown in Figure 4.5.
3. An example of these results is shown in Figure 4.6.
4. An example of these results is shown in Figure 4.7

4.3 Relationship between CV charge and double layer capacitance of Ferrocenyl-thiolate SAMs and signal drift

4.3.1 Drift of Ferrocenyl-thiolate SAM electrochemistry in $Fe(CN)_6^{4-}$ solution

To determine if the cause of the signal drift shown in Figure 4.5 and Table 4.1 (4th data column) arises from the SAM itself, a series of ternary Fc-amide SAMs, prepared from a thiol ethanolic solution composed of v/v 5% Fc-amide, 30% MUA and 65% MUO, were immobilized on polycrystalline Au electrodes. These electrodes were not modified further, as was done in the

study described in Section 4.2. EIS and mediation CVs were then collected every 20 min for a total of 120 min (7 measurements) in 5 mM $Fe(CN)_6^{4-}$ + 0.2 M PB (pH 7.0), as shown in Figure 4.7a and b, respectively, to determine their susceptibility to drift. A change in R_{CT} of 43 ± 9% was observed from t = 0 to 120 min and the peak currents and potentials changed by 1 ± 3, and -9 ± 6 %, respectively (N = 3), as also shown in the 4th column of Table 4.1.

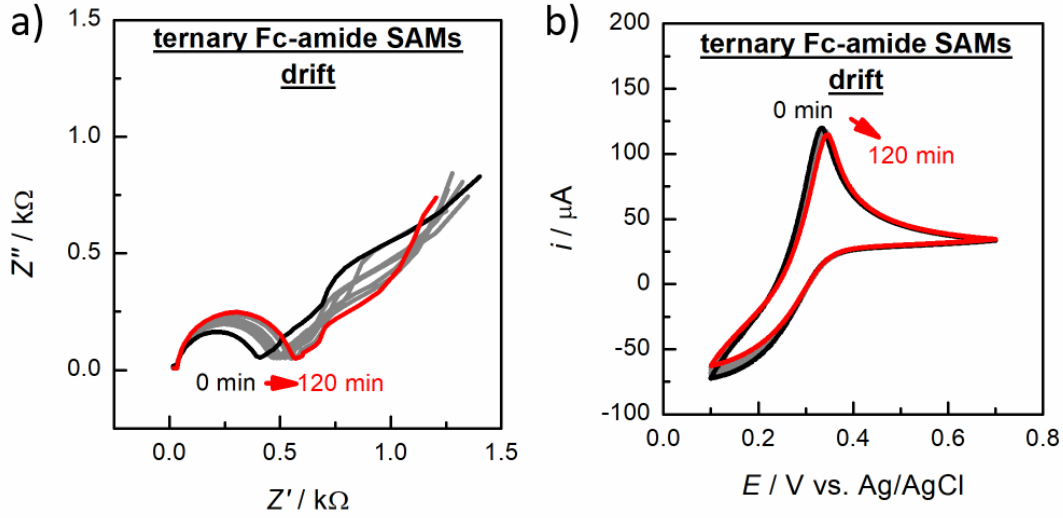

Figure 4.7: Electrochemical drift of ternary Fc-amide SAMs (no TLR-4 attached), where the black, grey, and red traces are at 0, 20-100 min, and 120 min, respectively, in 5 mM $Fe(CN)_6^{4-}$ + 0.2 M PB (pH 7.0). (a) Nyquist plots were collected at 0.300 V from 1 MHz to 0.1 Hz and (b) shows the mediation CVs (100 mV/s) that followed each EIS test in (a).

As seen in the 2nd and 4th data columns of Table 4.1, the drift of the Fc-containing SAM in both the EIS and CV experiments in 5 mM $Fe(CN)_6^{4-}$ + 0.2 M PB (pH 7.0) is of a similar magnitude and in the same direction as was the response of the TLR4 sensor to HKST lysates (Figure 4.5). This suggests that there is already a problem with the SAM that bonds the TLR4 sensing component to the Au electrode. For this reason, Section 4.3.2 is focused on a deeper analysis of changes seen in the amount of electrochemically active Fc (Γ_{Fc}) present on the surface (obtained from the CV peak charges) and the packing quality of the fully immobilized thiolate SAM

(measured from the capacitance at 0.1 V in the double layer region) with time in 0.2 M PB (pH 7.0), before and after collection of EIS and CV data. The primary goal of this work was thus to determine if the drift seen in Figure 4.7 originates from drift in the electrochemistry of the SAM itself.

4.3.2 Drift of Ferrocenyl-thiolate SAM electrochemistry in PB solution

Section 4.3.1 showed that the electrochemistry of the ternary Fc-amide SAMs in a $Fe(CN)_6^{4-}$ + 0.2 M PB (pH 7.0) solution is susceptible to drift, but it remained unclear which of the three thiol components (Fc-amide, MUA or MUO) was responsible for this. For this reason, a rigorous study of the electrochemistry of these SAMs in 0.2 M PB (pH 7.0) was carried out by collecting three CVs at 100, 250, and 500 mV/s, in that order. Figure 4.8a shows the second CV at each of these scan rates before collection of the EIS and CV data in $Fe(CN)_6^{4-}$ + 0.2 M PB.

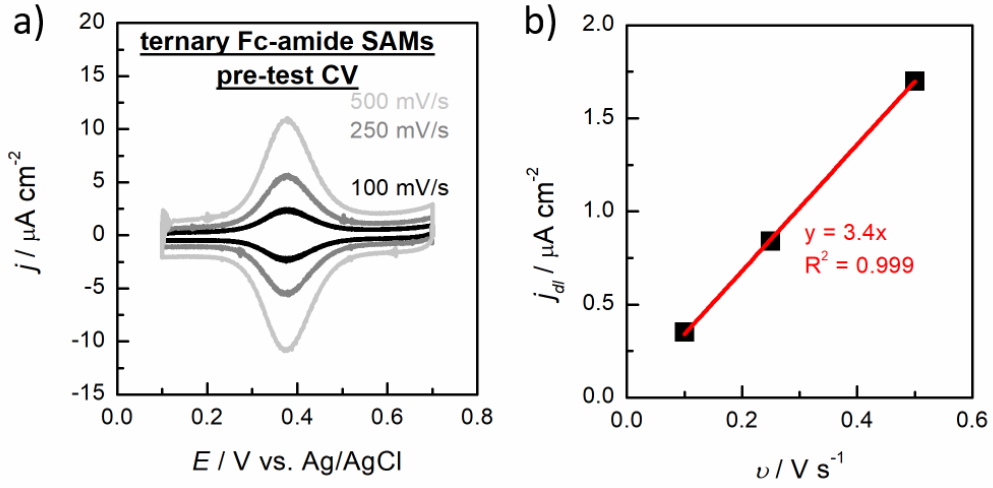

Figure 4.8: (a) CVs of Fc-amide ternary SAMs collected in 0.2 M PB (pH 7.0) before the collection of EIS and CV data in $K_4Fe(CN)_6$ + 0.2 M PB (pH 7.0). These CVs were collected at 100 (black), 250 (grey) and 500 (light grey) mV/s. In (b), the double-layer current measured at 0.1 V from the CVs in (a) is displayed vs. sweep rate. The linear fit and R^2 values are shown in red.

Figure 4.8a shows that Faradaic current flows between 0.2 and 0.55 V, where the anodic and cathodic peaks correspond to the oxidation of Fc to Fc^+ and reduction of Fc^+ to Fc, respectively. Similar to the analysis described in Section 4.1.2, the Faradaic peak charge was calculated, where it is assumed that every surface-bound Fc thiol is electrochemically active and thus that the charge can be translated to Fc coverage. At 500 mV/s, the average Faradaic charge is 5.4×10^{-7} C, and based on a real Au surface area of 0.24 cm^2, this gives a Fc coverage of 2.4×10^{-11} mol cm^{-2} (corresponding to a ~5 % of a full monolayer). As this is also the %v/v solution composition of Fc-amide in the three-component thiol ethanolic solution, this argues that the thiol solution composition translates well to the composition of the ternary SAMs on Au in the present work.

In Figure 4.8a, double layer currents are again seen to pass on either side of the Fc redox peaks in the range of 0.1 – 0.2 V and 0.55 – 0.7 V. Representative capacitance values were calculated from the double layer currents passed at 0.1 V, chosen because of minimal interference from any other redox reactions. The capacitance has been related to the insulating nature of SAMs, as described by Equation 2.4, which shows the direct proportionality of dielectric constant with capacitance [114]. Figure 4.8b displays the linear dependence of the double-layer currents (from Figure 4.8a) on sweep rate, with a capacitance of 3.4 µF cm^{-2} obtained from the slope of the plot for this SAM. These experiments in Figure 4.8 were carried out prior to the collection of EIS and CV data in $Fe(CN)_6^{4-}$ + 0.2 M PB (pH 7.0).

Figure 4.9 compares the CVs collected in 0.2 M PB (pH 7.0) before (black) and after (red) the collection of EIS and CV data in $Fe(CN)_6^{4-}$ + 0.2 M PB (pH 7.0) for 120 min. It is seen that the magnitude of the Fc charge, and hence the Fc surface coverage, has decreased from 2.4 to 1.6 $\times 10^{-11}$ mol cm^{-2}, indicating a loss in Fc redox activity. However, the double-layer currents have

also decreased, from 3.4 to 3.1 µF cm^{-2} (Table 4.2), which is the opposite of what would be expected if the loss in the Fc thiol redox peak was due to the loss of some of the thiolate molecules from the surface. Note that the capacitance of clean bare Au electrodes is approximately one order of magnitude higher than seen for a Au surface modified with a medium chain-length alkanethiolate SAM (n ≥ 8 methylene groups) [141].

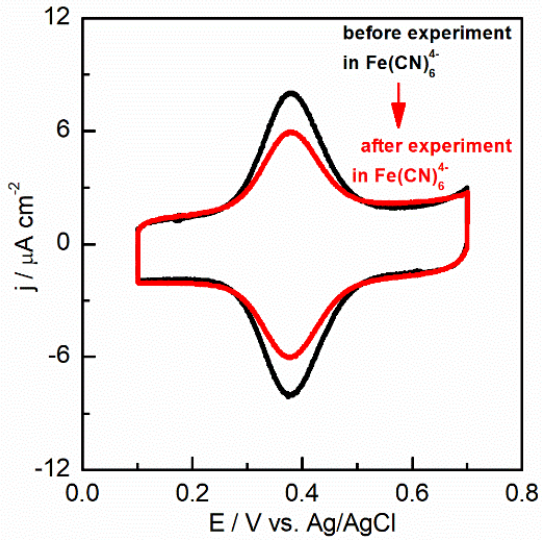

Figure 4.9: Typical CVs (500 mV/s) of ternary Fc-amide SAMs in 0.2 M PB (pH 7.0), collected before (black) and after (red) electrochemical testing in 5 mM $K_4Fe(CN)_6$ + 0.2 M PB (pH 7.0).

In Section 4.3.1, the $\%\Delta R_{CT}$ of the SAMs, tested in 5 mM $Fe(CN)_6^{4-}$ + 0.2 M PB (pH 7.0), was 43 ± 9 %. The first column of Table 4.2 shows that the Fc surface coverage of these same SAMs (N = 3) in PB alone, after these experiments, decreased from 1.9 ± 0.4 to 1.2 ± 0.2 x 10^{-11} mol cm^{-2}, corresponding to a -38 ± 3 % change. However, the capacitance remains relatively constant, changing only from 2.9 ± 0.5 to 2.7 ± 0.4 µF cm^{-2}, corresponding to a -7 ± 2 % decrease after testing in 5 mM $Fe(CN)_6^{4-}$ solutions (Table 4.2). As the double layer charging current hardly changes, while the Fc redox peak drops quite a bit, this suggests that the overall SAM structure

and coverage is retained, but that only a loss of the Fc redox activity occurs. This is because capacitance values are indicative of the packing quality of SAMs, and desorption of immobilized thiolates makes SAMs less well-packed. This would result in an increase in capacitance values, which is the opposite of what is observed here.

Table 4.2: Change in Fc surface coverage and double layer capacitance obtained for ternary Fc-amide SAMs (N = 3) in 0.2 M PB (pH 7.0) solution, before and after electrochemical testing (EIS and CV) in 5 mM $K_4Fe(CN)_6$ + 0.2 M PB (pH 7.0). Example CVs from which these values are obtained are shown in Figure 4.9.

	Γ_{Fc}	C_{dl}
Before electrochemical testing in $Fe(CN)_6^{4-}$	$(1.9 \pm 0.4) \times 10^{-11}$ mol cm^{-2}	2.9 ± 0.5 µF cm^{-2}
After electrochemical testing in $Fe(CN)_6^{4-}$	$(1.2 \pm 0.3) \times 10^{-11}$ mol cm^{-2}	2.7 ± 0.4 µF cm^{-2}
%Δ	-38 ± 3 %	-7 ± 2 %

One option to explain the decrease of the Fc redox-activity is that some of the Fc-amide component of the SAMS (ca 5% initially) has desorbed, while the remaining MUA and MUO units remain immobilized. If this is the case, it may not result in a measurable increase in double-layer capacitance. However, this hypothesis is not reasonable for two reasons. First, the literature on alkanethiolate SAMs has shown that desorption occurs primarily under basic conditions (pH > 11) and only with the application of a cathodic potential [153]. Secondly, desorption of domains of alkanethiolates is known to occur in regions where immobilized molecules are not well-packed [154], which is inconsistent with our hypothesis because our SAMs are strongly suspected to be homogeneously distributed. It is also possible that processes such as conversion of dissolved thiols into disulfides and/or immobilized thiolates into sulfonates [61,155,156] were responsible for selective desorption of the Fc-amide component, thereby causing drift. In Section 4.4, this is tested by attempting to prepare better-packed SAMs that are less likely to oxidize and desorb, achieved

by adding the reducing agent, Tris(2-carboxyethyl)phosphine (TCEP), to the thiol ethanolic solution prior to the deposition process.

4.4 Effect of TCEP on electrochemistry of ternary Fc-amide SAM prepared from fresh vs. aged thiol solutions

In Section 4.3, the drift in the electrochemistry of ternary Fc-containing SAMs was shown to be a problem with this generation of TLR4-based sensors. Analysis of CVs collected in 0.2 M PB (pH 7.0), before and after testing in 5 mM $Fe(CN)_6^{4-}$ + 0.2 M PB, revealed that the source of drift seemed to be the loss of the redox-active Fc thiol, but without significant change in the packing and coverage of the full SAM layer. As stated in the previous section, this could be explained by the desorption of only the Fc-amide thiolates, while the MUA and MUO would then remain immobilized.

It is known that the thiol functional groups of alkanethiols, dissolved in EtOH, are prone to oxidation and decomposition, which could influence their packing and cause a loss in the Fc redox peak changes. These oxidized thiol decomposition by-products, such as disulfides and sulfonates, can build up both in the thiol deposition solution and within the respective SAMs when exposed to O_2 and UV-visible radiation [157]. These oxidized products have a lower desorption energy than thiolate SAMs and hence desorb more readily [155]. It is possible that the Fc-amide thiol, as compared to MUA and MUO, is more likely to form disulfides, therefore resulting in relatively higher desorption rates, although it is hard to prove this electrochemically.

Despite the formation of organized alkanethiolate SAMs from either disulfide or thiol precursor solutions [63,158,159], SAMs prepared from the latter solutions are better packed than those from the former [115]. Furthermore, it has been reported that the presence of just 3% of the disulfide decomposition product in the thiol precursor solution could introduce a significant

number of defects in the resultant SAMs, as observed by the poorer performance of these SAMs as molecular diodes, due to the permeation of contaminants into poorly-packed SAMs [115]. The development of poorly-packed SAMs as a result of disulfide impurities should be detectable by an increase in the capacitance, especially when preparing SAMs using precursor thiol solutions that have been stored for a period of time. This is because it is suspected that accumulation of disulfides at levels large enough to be detectable by monitoring the double layer capacitance requires a few days to occur [61]. Also, the issue of storage of thiol solutions used to prepare SAMs could be an issue, especially relevant to the potential use of these sensors in practice.

To determine if the formation of disulfides is occurring in the thiol deposition solutions to any notable extent and is then linked to the loss of the Fc thiol redox activity with time of testing and, in turn, to sensor signal draft, the packing quality of the ternary SAMs under study here was evaluated. This was done by tracking the double layer capacitance of the Fc-containing ternary SAMs produced using aged vs fresh thiol solutions, as it is well known that well-packed SAMs will have a lower capacitance than defective SAMs [114].

The preparation of TLR4-based sensors [18,143] previously by our group was done in thiol ethanolic solutions that had been stored up to a few months at 4 ^{0}C, while here, the effect of storage of the precursor thiol solutions (up to a few weeks) was examined. In these experiments, ternary Fc-amide SAMs with the same composition as those studied in Section 4.3 were investigated (5% (v/v) 1 mM Fc-amide, 30% (v/v) 1 mM MUA and 65% (v/v) 1 mM MUO), with CVs again collected in 0.2 M PB (pH 7.0) at 100, 250, and 500 mV/s, in that order (Section 4.3). Figure 4.10a displays the standard CV response for Fc thiols (at 500 mV/s) for a freshly prepared SAM (black trace) and for SAMs prepared from thiol solutions that had been stored for 1, 2, 3, 4, 6, 9 (grey traces), and 19 weeks (red trace) at 4 ^{0}C, all without any TCEP added.

The corresponding double layer capacitance values at 0.1 V, which are a good indication of SAM coverage, do not change, as shown in Figure 4.10b for three independent SAMs (N = 3, except for storage time of 19 weeks). These relatively constant capacitance values indicate that the quality of SAM packing, and thus likely their coverage and composition, are unaffected by thiol solution storage time at 4 ^{0}C, even up to 19 weeks. Thus, the formation of disulfide impurities is either not occurring or cannot be observed by monitoring capacitance.

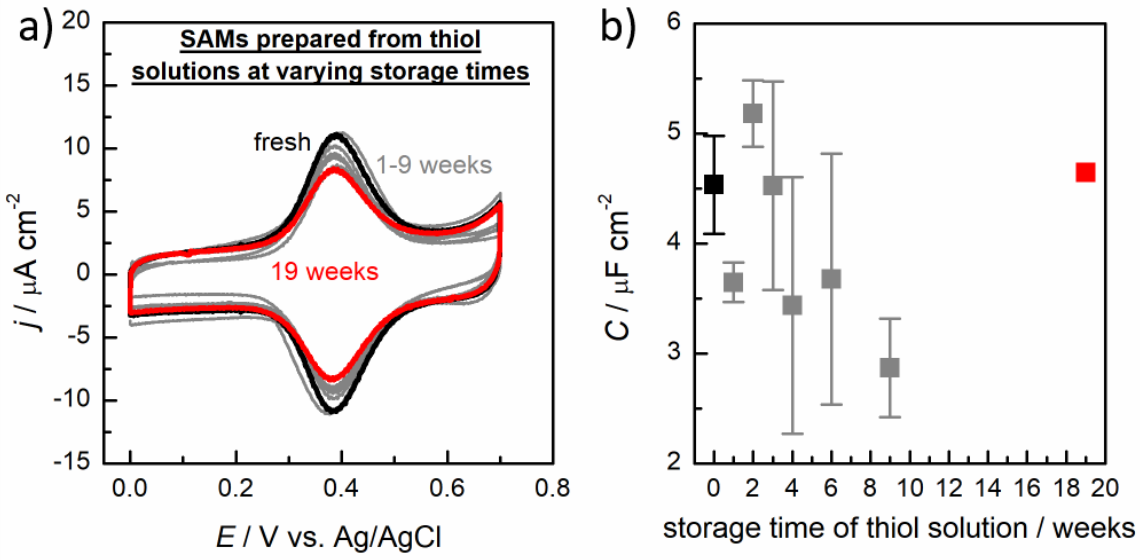

Figure 4.10: Electrochemical response of ternary Fc-amide SAMs in 0.2 M PB (pH 7.0), prepared from thiol solutions that were freshly prepared (black) or stored for 1, 2, 3, 4, 6, 9, (grey) and 19 weeks (red) in a 4 ^{0}C refrigerator. In (a), CVs of an example set of SAMs at 500 mV/s are shown, while (b) gives the capacitance values at 0.1 V (N = 3 , except for storage time of 19 weeks).

In the next part of this work, disulfide formation and its possible effect on the Fc thiol response with time was tracked from the charging current, with and without the addition of Tris (2-carboxyethyl)phosphine. TCEP is known to cleave disulfide bridges of proteins in aqueous conditions [160,161]. This is a common method used to reduce any disulfides present in solution [160,161], although the reduction of disulfides to thiols, via TCEP, is normally carried out in aqueous solutions because H_2O participates in the reaction [160,161], instead of the ethanolic

solutions used here. Note that after the addition of 10 mM TCEP, the solutions were incubated in the dark for 1 h before immersion of the Au electrode in the TCEP-containing thiol solution [162].

The CVs of the Fc-containing ternary SAMs formed from the thiol solutions containing TCEP (3 scans at 100, 250, and 500 mV/s) are shown in Figure 4.11. It is clear that the double layer capacitance has hardly changed (3.4 ± 0.5 and 4.0 ± 1.2 µF cm^{-2} respectively (N = 3)), with no TCEP and TCEP added. This confirms that either decomposition of the thiols to disulfides is not occurring or that TCEP is not effective in reducing the disulfides back to the thiol form in ethanolic solutions. Although it seems likely that disulfide formation is not the problem, as was concluded previously when monitoring the SAMs capacitance as a function of storage time of thiol solutions, these results do not fully rule out that electrochemical drift of the sensor is caused by selective desorption of the Fc-amide thiol from within the ternary SAMs.

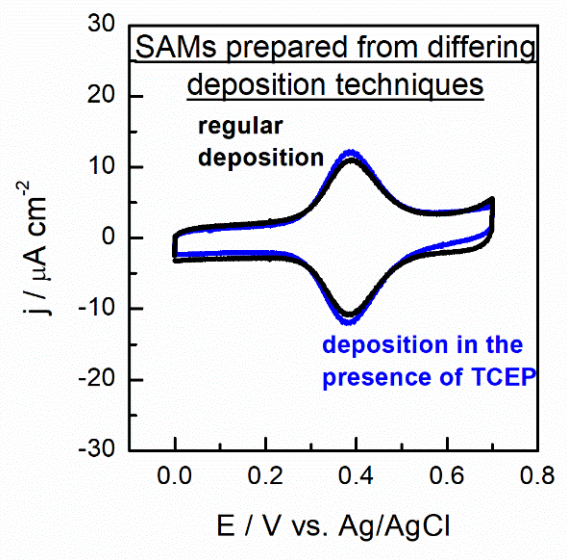

Figure 4.11: Cyclic voltammograms at 500 mV/s of ternary Fc-amide SAMs, collected in 0.2 M PB (pH 7.0), prepared from freshly prepared thiol ethanolic solutions using regular deposition (black trace) and deposition in the presence of TCEP (blue).

4.5 Effect of Fc-amide thiol content within the SAM on drift of ternary Ferrocenyl-thiolate SAM electrochemistry

It was shown in Section 4.4 that the presence of TCEP (prior to the immobilization process) did not alter the quality of the ternary Fc-thiol containing SAM packing, as determined from double layer capacitance measurements. Therefore, it could not be conclusively established if the source of SAM electrochemistry (and sensor) drift is related to the desorption of the Fc-amide thiol, perhaps after its oxidation to disulfides, as disulfides are known to desorb more readily than do thiols. Therefore, the effect of the concentration of the Fc-thiol within the SAM (Table 4.3) on drift was examined here. If the Fc-thiol does desorb, this should be more detectable at higher Fc thiol contents within the SAM, with the SAMs prepared using thiol solutions containing TCEP.

Table 4.3: Composition of ethanolic thiol solutions used to prepared Fc-amide SAMs electrochemically tested in Section 4.5.

	% (v/v) Fc-amide	% (v/v) MUA	% (v/v) MUO
1% Fc-amide	1	30	69
2% Fc-amide	2	30	68
5% Fc-amide	5	30	65
20% Fc-amide	20	15	65

CVs of these SAMs were collected in 0.2 M PB (pH 7.0) at 100, 250, and 500 mV/s (3 scans at each rate and in that order) for the purpose of monitoring the Fc surface coverage and thiol coverage and degree of order from the interfacial capacitance, measured before and after electrochemical testing in 5 mM $Fe(CN)_6^{4-}$ + 0.2 M PB (pH 7.0). Figure 4.12 displays the CV responses of 1 % (black), 2 % (dark grey), 5 % (grey), and 20 % (light grey) Fc-amide SAMs in fresh PB at 500 mV/s, giving Fc coverages of 0.3, 0.7, 2.6, and 4.5 x 10^{-11} mol cm $^{-2}$, respectively, corresponding to ~1 %, 2 %, 5 %, and 13 % of the full monolayer [130]. This indicates that the

electrochemically active Fc content in the SAMs tracks the solution content very well, especially at < 10% Fc, where the standard Fc content in this chapter is 5%. For the highest Fc-amide thiol concentration of 20%, this is not reflected in the peak charge density, giving only 13%. To explain the discrepancy between solution and surface composition of multiple component SAMs it is important to understand the phenomenon governing composition.

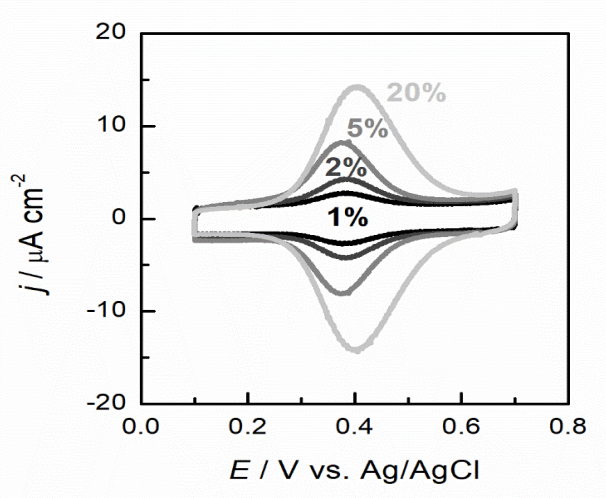

Figure 4.12: Cyclic voltammograms of nominally 1 % (black), 2 % (dark grey), 5 % (grey), and 20 % (light grey) Fc-amide SAMs (Table 4.3) at 500 mV/s in 0.2 M PB (pH 7.0), prepared from stored thiol solutions using solutions containing TCEP.

The mechanism directing the composition of multiple-component SAMs can be broadly classified as kinetically or thermodynamically controlled. The former means that the SAM composition is determined by phenomena such as diffusion of alkanethiol to the substrate, steric hindrance of Au-S bond formation, etc., which occur when equilibrium is not established. The latter means that the SAM composition is determined by its stability, meaning that the SAM composition with the lowest Gibbs free energy would form, which occurs when equilibrium can be established. Experimentally, it was determined that SAMs prepared using a high thiol concentration precursor solution (≥ 1 mM) at 25 ^{o}C by immersion of a Au substrate for 1 day are

either at or near equilibrium [163]. Henceforth, it is assumed that the composition of our ternary SAMs is controlled by thermodynamics rather than kinetics.

Under these conditions, the composition of multiple component SAMs is dependent on the length of the alkane chains [120,137,164] and the terminal groups [116]. Longer-chain alkanethiols are preferentially adsorbed due to the poor solvation of alkane chains in EtOH, thereby generating a greater thermodynamic drive for the longer chains to be removed from the polar protic solvent and placed into the non-polar monolayer [120,137,164]. In the case of our ternary SAMs, the length of the alkane chains is similar, which means that this does not play a factor in contributing to the discrepancy between solution and surface composition. Typically, the stronger the intermolecular interactions between the alkanethiol and EtOH, the less likely the molecules will adsorb. For example, the literature suggests that alkanethiols with a terminal -COOH group almost never preferentially adsorb over other components because they form multiple H-bonds with EtOH. Similarly, alkanethiols with a terminal -OH group preferentially adsorb because their interactions with EtOH are weaker than those between -COOH groups and EtOH [116]. This is consistent with our observations when using ternary Fc-amide SAMs because it is likely that the amide group attached to the Fc increases its solubility, ensuring that it prefers to remain dissolved in EtOH rather than adsorbed into the monolayer.

The double-layer capacitance of these SAMs was again measured at 0.1 V, giving 2.9, 3.3, 3.1 and 2.4 μF cm^{-2}, respectively, as the % Fc-thiol increased. Electrochemical testing of these SAMs was then carried out in 5 mM $Fe(CN)_6$ + 0.2 M PB (pH 7.0), as in Section 4.3.1, collecting EIS data at 0.300 V at frequencies ranging from 1 MHz to 0.1 Hz, followed by three ‘mediation

CVs' 100, 250, and 500 mV/s (in that order). The EIS and mediation CV data were collected every 20 min for 120 min.

Figure 4.13a, b, c, and d display the Nyquist plots of 1 %, 2 %, 5 %, and 20 % ternary Fc-amide SAMs, respectively, showing two important trends. Firstly, R_{CT} at t = 0 min for these four SAMs is 788, 430, 87, and 96 Ω cm^2, respectively, generally consistent with the higher currents expected when more Fc thiol is present. Secondly, the signal drift (%ΔR_{CT} from t = 0 min to 120 min) is 38, 34, 45, and 69 % (Table 4.4), respectively. The 20% Fc thiol containing SAM is an outlier, likely due to the distribution of immobilized Fc-thiolate on the Au surface. This could be confirmed by measuring the CV peak width at half-height in Figure 4.12, which are 100, 102, 113, and 151 mV, respectively, as the % Fc-thiol increases. Lennox *et al.* determined that the presence of both isolated and clustered Fc domains can result in broadened CV peaks due to the two populations having significantly different peak potential values [121–123]. It is hypothesized here that increasing the Fc-thiol solution composition increases the likelihood of formation of domains of Fc clusters, and that the Fc present in clusters may be less stable than is an isolated Fc thiolate.

After electrochemical testing of these SAMs in 5 mM $Fe(CN)_6^{4-}$ + 0.2 M PB (pH 7.0), CVs were collected using the same conditions as previously, with Figure 4.14 showing the results. The change in Fc surface coverage ($\Delta\Gamma_{Fc}$) between the value before (PB, Figure 4.12) and after exposure and electrochemical testing in the $Fe(CN)_6^{4-}$ + 0.2 M PB (pH 7.0) solution (Figure 4.14) is -0.1, -0.2, -0.9, and -3.0 x 10^{-12} mol/cm^2, respectively, increasing with more Fc thiol in the SAM. However, the change in double layer capacitance (%ΔC) of these SAMs is – 12 %, -2 %, -11 % and +6 %, respectively, showing no obvious trend. These ΔΓ and %ΔC values are given in the second and third data column of Table 4.4, respectively.

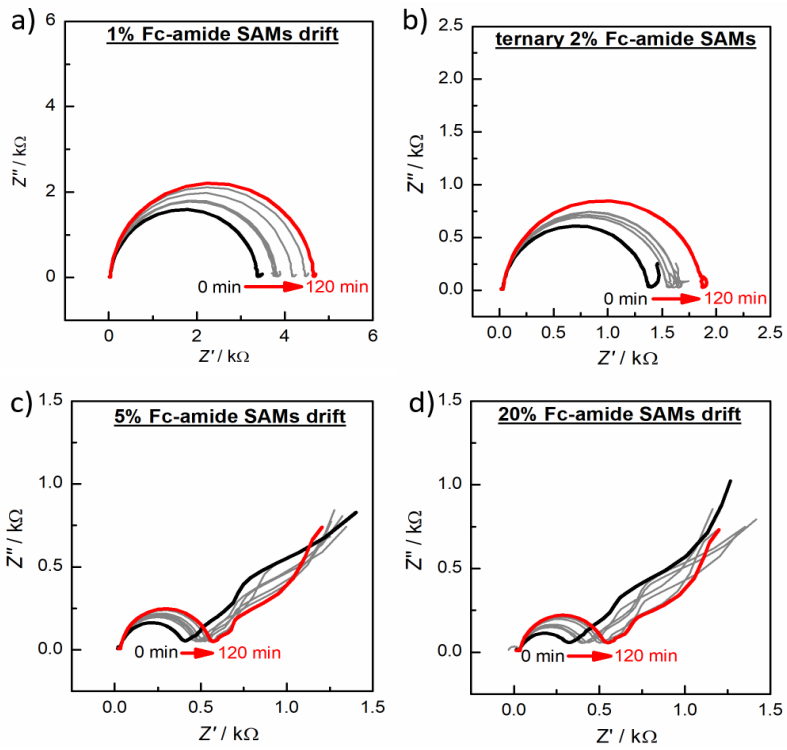

Figure 4.13: Electrochemical response of ternary (a) 1 %, (b) 2 %, (c) 5 %, and (d) 20 % Fc-amide SAMs at t = 0 min (black), showing the drift after 20 - 100 min (grey) and after 120 min (red) in 5 mM $K_4[Fe(CN)_6]$ + 0.2 M PB (pH 7.0). Data were collected every 20 min at 0.300 V from 1 MHz to 0.1 Hz.

There are two trends observed in Table 4.4. Firstly, as expected, the larger the loss in Fc coverage ($\Delta\Gamma_{Fc}$), the larger the $\%\Delta R_{CT}$. Secondly, the double-layer capacitance values remain relatively constant even when a decrease in the amount of redox-active Fc-thiol charge is seen. For example, the 5% Fc-amide SAMs experience a loss of 0.9 μC cm^{-2} (equivalent to 0.9 x 10^{-11} mol of Fc cm^{-2}), which equates to a loss of ~2% of the total immobilized thiolate molecules. Thus, the changes in capacitance may not be detectable. However, it is also possible that the loss of the Fc CV peaks could be explained by the loss of just the Fc group from the Fc-amide-thiols, a situation that would likely not lead to any changes in the double layer capacitance.

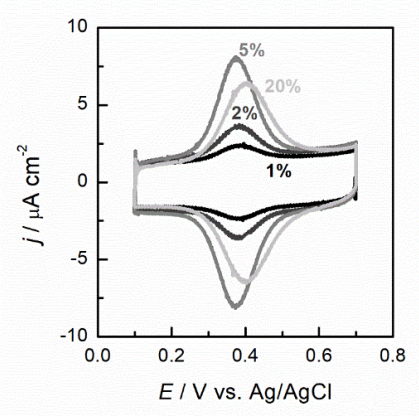

Figure 4.14: Cyclic voltammograms of 1 % (black), 2 % (dark grey), 5 % (grey), and 20 % (light grey) ternary Fc-amide SAMs at 500 mV/s in 0.2 M PB (pH 7.0) after electrochemical testing in 5 mM $K_4Fe(CN)_6$ + 0.2 M PB (pH 7.0).

In Section 4.6, the effect of exposure of the ternary 5 % Fc-amide SAMs to the 5 mM $Fe(CN)_6^{4-}$ + 0.2 M PB (pH 7.0) + various concentrations of the product formed by electrochemical mediation (i.e., $Fe(CN)_6^{3-}$) on the drift in R_{CT} was examined. This was done to determine if the loss of the Fc peak charge is related in some way to the turn-over of the Fc moieties, forming Fc^+, during the electrochemical generation of $Fe(CN)_6^{3-}$ during CV and EIS testing

Table 4.4: The $\%\Delta R_{CT}$ measured from Nyquist plots shown in Figure 4.13, and the $\%\Delta C$ and $\Delta\Gamma_{Fc}$ values measured from the CVs shown in Figure 4.12 and Figure 4.14, for ternary SAMs with increasing surface coverage of Fc-amide.

	$\%\Delta R_{CT}$	$\Delta\Gamma_{Fc}$ / 10^{-11} mol cm^{-2}	$\%\Delta C$
1% Fc-amide SAMs	38 %	-0.1	-12 %
2% Fc-amide SAMs	34 %	-0.2	-2 %
5 % Fc-amide SAMs	45 %	-0.9	-11 %
20 % Fc-amide SAMs	69 %	-3.0	+6 %

4.6 Effect of ferro/ferricyanide on drift of ternary Ferrocenyl-thiolate SAM electrochemistry

In order to examine if there was any effect of time of exposure of the Fc-amide thiolate within the SAMs to the solution based redox couple (i.e., $Fe(CN)_6^{4-}$ and electrochemically

generated $Fe(CN)_6^{3-}$) on the drift of the Fc-amide SAM in PB solution, another series of experiments was carried out. In this work, the SAM used was again composed of 5 % (v/v) Fc-amide, 30 % (v/v) MUA and 65 % (v/v) MUO and was tested in 5 mM $Fe(CN)_6^{4-}$ + 0.2 M PB (pH 7.0) first and then again after the addition of increasing concentrations of $Fe(CN)_6^{3-}$. The same electrochemical protocol was used as described in Section 4.5, gathering data every 20 min for 120 min in these 5 mM $Fe(CN)_6^{4-}$ + 0.2 M PB (pH 7.0) + 0, 5, 25 or 50 mM $Fe(CN)_6^{3-}$.

Figure 4.15 (a-d) shows the Nyquist plots of the ternary SAM in these solutions, with the drift seen to unexpectedly increase quite significantly with increasing $Fe(CN)_6^{3-}$ concentration, i.e., $\%\Delta R_{CT}$ = 44 %, 54 %, 62 % and 81 %, respectively. To better understand this, the mediation CVs in the solutions containing increasing concentrations of $Fe(CN)_6^{3-}$ were examined, with example mediation CVs collected immediately after EIS data collection at t = 0 min shown in Figure 4.16. In these CVs, while primarily only $Fe(CN)_6^{4-}$ oxidation should be seen due to the expected redox mediation offered by the surface-bound Fc groups, the cathodic currents are also seen to increase, likely occurring by the reduction of $Fe(CN)_6^{3-}$ to $Fe(CN)_6^{4-}$ at SAM defect sites (which are described in greater detail in Section 2.3.1). Thus, because of these larger reduction currents and the resulting accumulation of $Fe(CN)_6^{3-}$ at the electrode surface, the oxidation currents increase commensurately, mediated by Fc^+.

Overall, it is clear from Figure 4.16 that the peak redox currents increase as the $Fe(CN)_6^{3-}$ concentration is increased, equivalent to a significantly higher turnover of the redox transitions of the Fc/Fc^+ mediating groups. It is possible that this is equivalent to longer times of EIS testing, even in 5 mM $Fe(CN)_6^{4-}$ concentrations, which means that drift is exacerbated by electrochemical testing under the conditions utilized in our biosensor/SAMs work. As will be discussed in Section 5.1, the Fc-thiolate SAM literature shows that, when Fc is oxidized to Fc^+, the Fc^+ form can

deactivate electrochemically, especially in electrolytes containing certain anions, including phosphate ions (i.e., HPO_4^{2-} and $H_2PO_4^-$) [153,165,166]. Thus, at higher $Fe(CN)_6^{3-}$ concentrations, the Fc terminal groups would spend significantly more time in the Fc^+ state, and thus would likely be more prone to electrochemical deactivation.

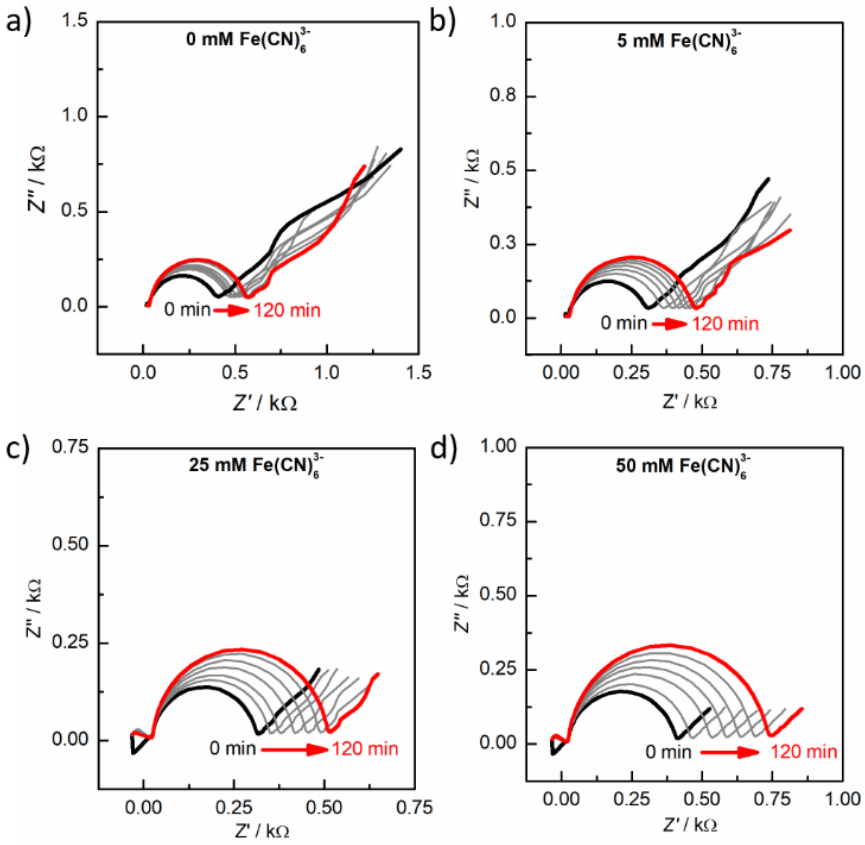

Figure 4.15: Electrochemical response of ternary Fc-amide SAMs at t = 0 min (black), after 20 - 100 min (grey), and after 120 min (red) of testing in 5 mM $K_4[Fe(CN)_6]$ + 0.2 M PB (pH 7.0) + (a) 0 mM, (b) 5 mM, (c) 25 mM, and (d) 50 mM $K_3[Fe(CN)_6]$. The EIS data were collected at 0.300 V from 1 MHz to 0.1 Hz. The $\%\Delta R_{CT}$ experienced by these SAMs is 44 %, 54 %, 62 % and 81 % respectively.

In summary, the drift issues described in this chapter are clearly related to a problem with the stability of the Fc/Fc^+ thiolate electrochemistry. In turn, these may be related to the nature of the solution ions present (specifically anions such as phosphate ions) combined with the length of

time that the Fc terminal group spends in the degradation-prone Fc^+ state. This hypothesis was further confirmed in Section 4.7, where the effect of time of exposure of the ternary 5 % Fc-amide SAMs to the 5 mM $Fe(CN)_6^{4-}$ + 0.2 M PB (pH 7.0) solution on the drift of R_{CT} was examined, all at the open circuit potential.

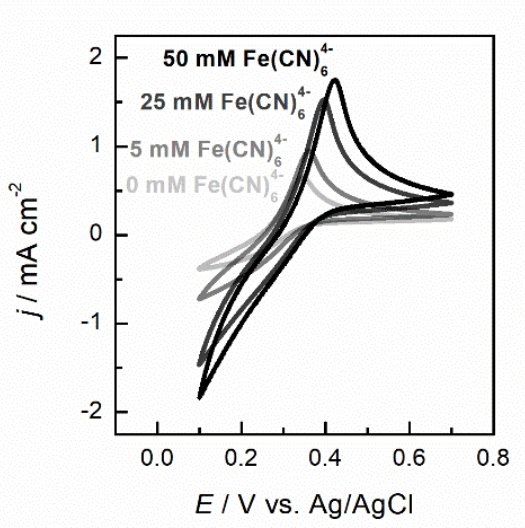

Figure 4.16: Mediation CVs of ternary Fc-amide SAMs at t = 0 min collected in 5 mM $K_4[Fe(CN)_6]$ + 0.2 M PB (pH 7.0) + (a) 0 mM, (b) 5 mM, (c) 25 mM, and (d) 50 mM $K_3[Fe(CN)_6]$. at 500 mV/s.

4.7 Effect of time of open-circuit exposure of the ternary Ferrocenyl-thiolate SAMs to the testing solution

It was shown in Section 4.6, that higher concentrations of $Fe(CN)_6^{3-}$ added to the 5 mM $Fe(CN)_6^{4-}$ + 0.2 M PB (pH 7.0) electrolyte solution resulted in higher Fc to Fc^+ currents and also a more rapid rate of drift of R_{CT}. This was attributed to the increasing concentrations of $Fe(CN)_6^{4-}$, formed by the higher rates of reduction of $Fe(CN)_6^{3-}$ at negative potentials during the collection of the mediation CVs. To test this hypothesis, EIS and mediation CVs were initially collected in 5

mM $Fe(CN)_6^{4-}$ + 0.2 M PB (pH 7.0) to determine the effect of varying amounts of time spent under polarization vs. at open circuit in this medium. In these experiments, three identical SAMs (5 % (v/v) Fc-amide, 30 % (v/v) MUA and 65 % (v/v) MUO) were investigated with the same number of CV and EIS tests experienced by each, but with the total time at the OCP varied (0, 120, and 360 min), as shown in Table 4.5.

Table 4.5: Electrochemical testing regime of SAMs in 5 mM $Fe(CN)_6^{4-}$ + 0.2 M PB (pH 7.00) (see Figure 4.17).

SAM location in Figure 4.17	Time of polarization	Total time in solution / min	Time at OCP between testing	$\%\Delta R_{CT}$
A	7 x ~ 1 min = ~7 min	~7	0 min x 6 = 0 min	137 %
B	7 x ~ 1 min = ~7 min	~127	20 min x 6 = 120 min	44 %
C	7 x ~ 1 min = ~7 min	~367	60 min x 6 = 360 min	26 %

Figure 4.17 (a - c) shows the Nyquist plots obtained for these three SAMs, indicating that there is significantly less drift when the SAM experiences more time in solution at the OCP between EIS and CV perturbations vs under electrochemically polarized conditions (Table 4.5). Because EIS testing takes longer and as the EIS data are collected under positive polarization, namely when the Fc group is predominantly in the Fc^+ state, this argues again that it is the oxidized form of Fc (i.e., Fc^+), and not Fc, that is prone to a process that results in the loss of surface-bound Fc redox activity.

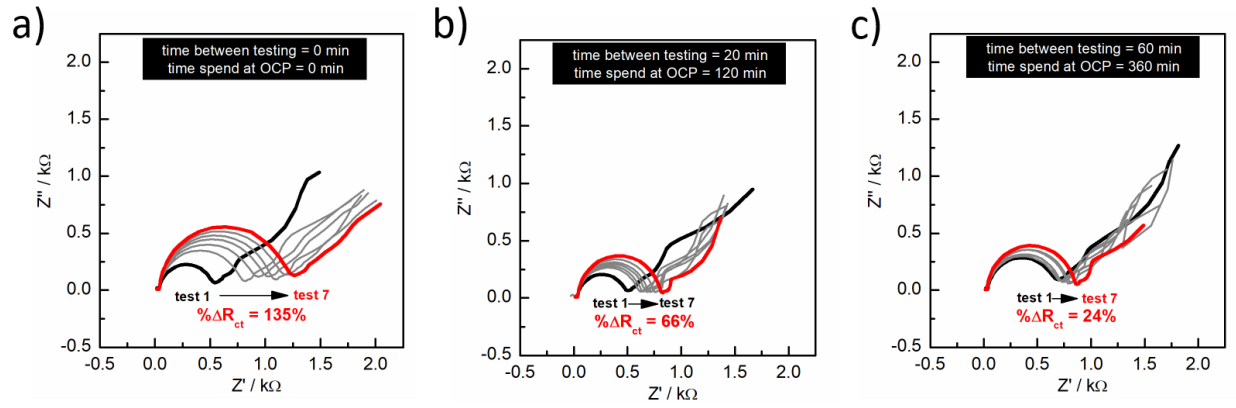

Figure 4.17: Electrochemical response of ternary Fc-amide SAMs collected in the 1st (black), in the 2nd - 6th (grey), and in the 7th measurement (red) in 5 mM $K_4[Fe(CN)_6]$ + 0.2 M PB (pH 7.0). EIS data were collected (a) seven times consecutively, (b) every 20 min for 120 min, or (c) every 60 min for 360 min.

4.8 Summary

In Chapter 4, an overview of sensor fabrication methods and the approaches used in electrochemical testing in this thesis work was provided, showing that the tracking of the % change in the charge transfer resistance ($\%\Delta R_{CT}$), determined by electrochemical impedance spectroscopy studies, is a reliable method to track the sensor response. Based on this work, it was determined that the TLR4-based sensors, involving ternary SAMs composed of 5 % (v/v) Fc-amide, 30 % (v/v) MUA, and 65 % (v/v) MUA, seem to respond well to HKST lysates, but are also susceptible to signal drift, with the magnitude of drift often being similar in magnitude to that of the sensor signal when tested in different concentrations of HKST lysates. Importantly, sensor drift with time was shown to correlate with a similar rate of loss of the electrochemical response (CV peak charge) of the Fc thiol group within the underlying SAM, which then translates to drift in the mediation CVs and EIS responses measured in $Fe(CN)_6^{4-}$ + 0.2 M PB solutions.

Thus, the focus of the remaining part of the chapter was placed on an investigation of some of the factors that may have led to loss of the redox activity of the Fc thiols within the SAM, without constructing the full sensor layer. While the initial hypothesis was that the loss of the Fc redox peak charge was caused by desorption of only the Fc-amide thiol, with MUA and MUO remaining on the Au surface, this was presumed to be unlikely because the literature does not support this theory of selective desorption [123,153,154] and also as the double layer capacitance did not increase. The likely retention of the Fc thiols on the Au surface was at least partly confirmed by the use of TCEP in the precursor thiol solution, as the addition of this reducing agent should have minimized thiol oxidation, which should have prevented thiolate desorption and resulted in the deposition of SAMs with better packing quality. However, this was not observed.

It was then shown that increasing the concentration of $Fe(CN)_6^{3-}$ resulted in greater drift of R_{CT}, likely caused by the higher rates of reduction of $Fe(CN)_6^{3-}$, in turn leading to higher rates of $Fe(CN)_6^{4-}$ oxidation, which occurs through mediation by Fc^+. These higher currents are thus indicative of significantly higher turnover rates of the Fc to form Fc^+, and thus the SAM is present in its oxidized state (i.e., Fc^+) for a longer period of time. This theory was confirmed by performing an experiment which showed that SAMs that are kept for longer times at the open circuit potential, vs. under positive polarization, are less susceptible to drift, thus pointing the finger at the relative instability of the Fc^+ moiety vs Fc, at least in these 5 mM $Fe(CN)_6^{4-}$ + 0.2 M PB (pH 7.0) test solutions.

In Chapter 5, the focus will thus be on developing methods to overcome the problem of loss of the Fc^+ redox activity which should then also minimize sensor drift. The approaches used in Chapter 5 are based partly on guidance obtained from the literature and on the results obtained from modifying both the SAM composition itself and the test solution conditions.

Chapter five: Overcoming loss of Ferrocenyl-thiolate SAM electrochemistry

5.1 Strategies employed to curtail Fc/Fc^+ redox deactivation

In Chapter 4, TLR4-based biosensors prepared from ternary SAMs (5 % (v/v) Fc-amide, 30 % (v/v) MUA and 65 % (v/v) MUO), shown in Figure 4.1, were demonstrated to be susceptible to quite significant electrochemical drift. This was found to arise from the loss of the Fc-containing thiol electrochemical response under our testing conditions (5 mM $K_4Fe(CN)_6$ + 0.2 M pH 7.0 phosphate buffer (PB)). This was then shown to translate directly to a loss in the currents arising from $Fe(CN)_6^{4-}$ oxidation, mediated by the Fc group on the surface, thus causing a steady increase in the electrode resistance (i.e., R_{CT}) with time, also referred to as drift. Further studies involving varying the time spent at potentials positive of the Fc/Fc^+ redox potential suggested that the Fc^+ form of the Fc-thiol is the likely unstable surface species.

To better understand how to tackle this problem, the literature was consulted. Several previous studies have reported the observed deactivation of Fc-terminated thiols in SAMs and have suggested that a ligand-exchange reaction may occur, causing the replacement of cyclopentadienyl (Cp^-) groups with anions. However, this was reported to occur only in the presence of ions such as Cl^-, Br^-, I^- and OH^- [167–169]. Furthermore, CN^- has been shown to participate in the cyanation of the Cp rings of Fc^+ [168], which would cause a loss of the Fc/Fc^+ redox signal. However, as these aggressive anions are likely only present in trace amounts in the present work, it remains unclear if the ligand-exchange process is occurring or not.

Another explanation provided in the literature for deactivation of Fc/Fc^+ electrochemistry involves ion-pairing of certain anions with Fc^+ (i.e., the complex would be held together without covalent bond formation [170]). For example, it was determined that ClO_4^- forms a 1:1 ion-pair with Fc^+, based on two key pieces of evidence. Firstly, the CV peak potential of the Fc/Fc^+ reaction

in Fc thiolate SAMs decreased by 59 mV per decade increase in [ClO_4^-], which according to the Nernst equation, indicates a 1:1 interaction with the Fc^+ [137,171–173]. Secondly, electrochemical quartz crystal microbalance studies have shown that the monolayer reversibly incorporates ~100 g/1 mole of electrons, which is the ratio expected for the binding of one ClO_4^- ion as one Fc is converted to one Fc^+ [174,175].

In other work, Badia *et al*. utilized peak potential values of Fc-thiolate SAMs to determine and rank other anions that possess the capability to ion-pair with Fc^+, which in decreasing order are PF_6^- > ClO_4^- > BF_4^- > NO_3^- [176]. Valincius *et al.* used Fourier-Transform surface enhanced Raman Spectroscopy to confirm the incorporation of these anions upon oxidation of the monolayer. Creager *et al*. suggested that anions with low solvation energies (in aqueous media) had a greater propensity for ion-pair formation and it was speculated that the low energetic cost required by these anions to shed their hydration shell gave them the incentive to pair with Fc^+ [136].

Badia *et al.* and Ju *et al.* have shown that a significant irreversible loss of the Fc CV redox peaks was also observed when the electrochemistry of Fc-thiolate SAMs was performed in solutions containing SO_4^{2-}, Cl^-, H_3CCOO^-, $H_2PO_4^-$ + HPO_4^{2-}, F^-, and $H_3NSO_3^-$ anions, none of which are expected to form stable ion-pairs with Fc^+ [13,14]. Also, it was shown that the integrated charge of the Fc CV peaks is more stable in electrolytes containing PF_6^-, ClO_4^-, BF_4^-, and NO_3^- ions [166,176,177], ions that have been implicated in ion-pairing. This could mean that the observed deactivation of the Fc/Fc^+ electrochemistry may be a matter of degree, depending on the nature of the anions present [178,179].

It has also been reported that, in oxidizable polar organic solvents, such as dimethyl sulfoxide (DMSO) and dimethylformamide (DMF), Fc^+ can be decomposed by a reaction with

molecular oxygen. In this reaction, an O atom acts as a bridge between two Fc^+ moieties by forming covalent bonds with their Cp rings, resulting in the formation of a dimer. In non-oxidizable solvents, such as acetonitrile, acetone and methylene chloride, the decomposition product is formed with a 50 % yield compared to in DMSO and DMF [180]. Covalently linking electron-donating groups to the Cp rings of Fc has been demonstrated to result in an increased stability of Fc against reaction with molecular oxygen, where UV-Visible spectroscopy showed that this may be due to an increased electron-density in the Fe(III) d-orbitals [181]. However, the current work was carried out only in aqueous solutions, so these earlier results may not be relevant here.

Silicon nitride microcantilevers, coated with Au on the top face, were used to study ion-pair formation between Fc-thiolate SAMs and electrolyte anions [176,178,182,183]. Microcantilevers are systems that bend due to chemical and/or physical events caused by the organic material deposited on the Au interface. In the case of Fc-thiolate SAMs, the oxidation of Fc to Fc^+ generates an expanding stress that bends Au in a convex manner, thus increasing its surface area [178,182]. This was attributed to the alkyl chains becoming more perpendicular and Fc reorienting upon oxidation of Fc to Fc^+ [175,184,185], thus increasing the SAM thickness [176] and the volume occupied by each thiolate molecule [186]. There are two variables that were suggested to influence the magnitude of surface stress, ion-pairing, and clustering of Fc. The change in surface stress, at positive potentials, of $HS(CH_2)_{11}Fc$ microcantilevers in the presence of various anions in decreasing order was: $PF_6^- > ClO_4^- > BF_4^- > NO_3^- > F^-$ (i.e., this is also the order of anions that form strong to weak ion-pairs with Fc^+, as described above), which indicates that formation of strong ion-pair induces a greater change in surface stress of microcantilevers [176]. It was also demonstrated that it was not merely the presence of Fc, but the presence of domains of clustered Fc, that induces maximal change in surface stress [183].

The organization of alkyl sulfate electrolyte anions ($H_3C(CH_2)_{n-1}SO_4^-$) on surfaces of Fc-thiolate SAMs via ion-pair formation was also studied by Badia *et al.* CVs of pure $HS(CH_2)_{11}Fc$ SAMs in the presence of $H_3C(CH_2)_{n-1}SO_4^-$ with n = 8, 10 or 12, present in the electrolyte, display a negative shift in the peak potential with a slope of 54-59 mV/$\log_{10}[H_3C(CH_2)_{n-1}SO_4^-)]$, indicating a 1:1 ion-pair formation with Fc^+, according to the Nernst equation. The authors showed that the n = 12 anion has a 44800 times greater ion-pair formation equilibrium constant than the n = 8 anion, because increasing the hydrophobicity of the anion increases its propensity to form ion-pairs with Fc^+ [170,187].

Murray *et al.* immobilized Au nanoparticles capped with $HS(CH_2)_6Fc$ SAMs (referred to as Monolayer Protected Clusters (MPCs)) on electrodes via ion-pair formation for purposes of charge storage applications [188–191]. In decreasing order, the extent of ion-pairing in CH_2Cl_2 was $NO_3^- > ClO_4^- > F_3CSO_3^- > PF_6^- > C_7H_7SO_3^-$, which is the opposite order of what is observed in aqueous solutions because, in CH_2Cl_2, hydrophobic anions are better solvated than hydrophilic anions [190].

Based on the above discussion, in order to explore the origin of the instability of the Fc thiolates in the SAMs investigated in Chapter 4 and to overcome it, the first direction of research involved examining the electrochemistry of the same ternary SAMs (i.e., 5 % (v/v) Fc-amide, 30 % (v/v) MUA and 65 % (v/v) MUO) as were studied in Chapter 4, but in $NaClO_4$ solutions rather than in PB supporting electrolyte (Section 5.2). Although this strategy has been shown to be successful in stabilizing surface-bound Fc/Fc^+ electrochemistry, ClO_4^- is a known chaotropic agent (molecules that weaken hydrophobic interactions responsible for establishing native protein structures), which can denature proteins and alter their function [19,192]. Also, for biosensor

applications, maintaining a solution at a biological pH level of ca. 7 is important to ensure protein (i.e., TLR4) stability, and thus a buffer should be present.

In the second direction, the electrolyte solution (still PB) was not changed, but rather, the diluent component of the mixed SAM was replaced with thiol molecules containing different terminal groups in an attempt to alter and stabilize the microenvironment of the Fc-moiety of binary Fc-amide SAMs (Section 5.3). It was hypothesized that certain terminal groups of diluent SAMs might restrict the access of harmful anions to Fc^+. However, no notable improved stability was observed.

Finally, a different and more stable Fc-thiol molecule (i.e., FcC_{11}), in which the electron-withdrawing amide-linkage was replaced by an electron-donating methylene linkage, was used to prepare another set of SAMs. This resulted in excellent electrochemical stability, even in the PB solution (Section 5.4). Sauvage *et al.* have demonstrated that increasing the number of electron-donating groups attached to the Cp rings of Fc results in an increased stability of Fc^+ due to the greater electron-density within the Fe(III) d-orbitals [181]. It is also possible that the removal of the amide linkage in FcC_{11} stabilizes the Fc moiety against reactions such as hydrolysis.

Importantly, it is also shown in the last section of this chapter that a TLR4-based sensor, prepared using a ternary SAM but with the Fc thiolate component containing the alkyl linkage instead of the amide, gave a significantly more stable response to its target, Lipopolysaccharides (LPS), than was shown at the start of Chapter 4. This successful result was achieved even in the standard pH 7 PB solution, and under conditions that would have led to a loss in the Fc/Fc^+ electrochemical signal, while using the amide-Fc thiolate. It is important to note that the potential of the working electrode is reported vs. the Ag/AgCl (saturated KCl) reference electrode throughout this chapter.

5.2 Stabilization of Fc/Fc^+ CV activity in $NaClO_4$ solutions

In this section, the same SAMs and electrochemical testing was conducted as performed in Chapter 4. The SAMs, prepared from ethanolic solutions consisting of 5 % (v/v) 1 mM Fc-amide, 30 % (v/v) 1 mM MUA and 65 % (v/v) 1 mM MUO, were CV tested at various times and sweep rates in 0.2 M PB (pH 7.0), and in 0.1, 0.25, 0.5, 0.75, 1 M $NaClO_4$ solutions. $NaClO_4$ was selected due to the strong ion-pairing capability of ClO_4^- with Fc^+, which is expected to stabilize the Fc/Fc^+ electrochemical signal [166,171,177]. As in Chapter 4 (Section 4.3.2), the $\%\Delta\Gamma_{Fc}$ values of the Fc groups over a certain period of time were measured from the electrochemistry, as this parameter gives a good indication of the degree of drift experienced by the SAMs.

Figure 5.1 presents CVs collected at 500 mV/s in 0.2 M PB (panel a) and 1 M $NaClO_4$ (panel b), with the $\%\Delta\Gamma_{Fc}$ values calculated from the Fc redox peak charges at t = 0 min (black trace) and after 120 min of CVs cycled every 20 min (red trace) A summarized set of results obtained in different solutions under otherwise the same conditions is given in Figure 5.2. In this section, drift was measured by collecting CV data in 0.2 M PB, instead of in 0.2 M PB + 5 mM $Fe(CN)_6^{4-}$, to understand the effect of the supporting electrolyte on the stability of the Fc/Fc^+ CV response.

Figure 5.1 clearly shows that the Fc/Fc^+ redox signal remains almost unchanged in the 1 M $NaClO_4$ solution, while in the 0.2 M PB solution, the peak charges drop noticeably. In Figure 5.1b, it may seem that peak charge is larger at t = 120 min than at 0 min, but this only appears to be the case because the peaks have become narrower by 12 mV over time. This actually results in a decrease in the peak charge of ca. 2 %. In this same figure, a positive shift of the peak potential over time is observed, but the reasons for this are not known at this time.

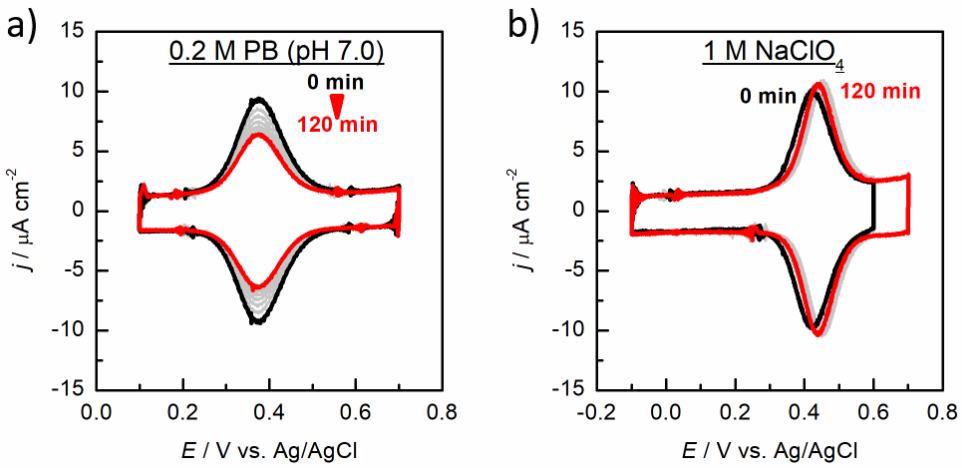

Figure 5.1: CV responses of ternary Fc-amide SAMs (5 % (v/v) 1 mM Fc-amide, 30 % (v/v) 1 mM MUA and 65 % (v/v) 1 mM MUO) collected at t = 0 min (black), 20, 40, 60, 80, and 100 min (light grey), and at t = 120 min (red) in (a) 0.2 M PB (pH 7.0) and (b) 1 M $NaClO_4$ solutions, all at 500 mV/s.

The peak potential (E_p), peak width (ΔE_{fwhm}), and double-layer capacitance (C_{dl}) values measured at t = 0 min from CVs collected in 0.2 M PB, and in 0.1, 0.25, 0.5, 0.75 and 1 M $NaClO_4$ are shown in Table 5.1. The peak potential moves positively in solutions containing higher concentrations of $NaClO_4$, which is opposite of what has been reported in the literature [136,166,171], as ion-pair formation between Fc^+ and ClO_4^- is known to thermodynamically stabilize the Fc^+ group, making it easier to oxidize [166,177]. Both the double-layer capacitance and peak width remain relatively invariant as a function of $NaClO_4$ concentration.

The change in peak charge over 120 min (which is indicative of the stability of Fc^+) of SAMs in 0.2 M PB and in 0.1, 0.25, 0.5, 0.75 and 1 M $NaClO_4$ are shown in Figure 5.2. The general trend in this figure is that loss of Fc/Fc^+ peak charge decreases with increasing ClO_4^- concentration. This is consistent with the literature, where the Fc^+ electrochemistry is more stable in solutions containing 1 M ClO_4^- (due to its ion-pairing capability) than in PB, thus more fully retaining the Fc/Fc^+ CV peak charges [153,165,166,171]. The loss of Fc/Fc^+ stability at lower

ClO_4^- concentrations could be explained by Le Chatelier's principle as decreasing the concentration of ClO_4^- will result in less formation of the ion-pair.

Table 5.1: Peak potential (1st data column), peak width (2nd data column), and double-layer capacitance (3rd data column) of ternary Fc-amide SAMs measured using CVs obtained at 500 mV/s in different solutions.

	Ep / mV vs. Ag/AgCl	ΔE_{fwhm} / mV	C_{dl} at 0.10 V / μF cm^{-2}
0.2 M PB (pH 7.0)	378	117	3.2
0.1 M $NaClO_4$	344	117	2.4
0.25 M $NaClO_4$	372	117	3.3
0.5 M $NaClO_4$	413	118	3.5
0.75 M $NaClO_4$	431	106	2.4
1 M $NaClO_4$	421	110	3.1

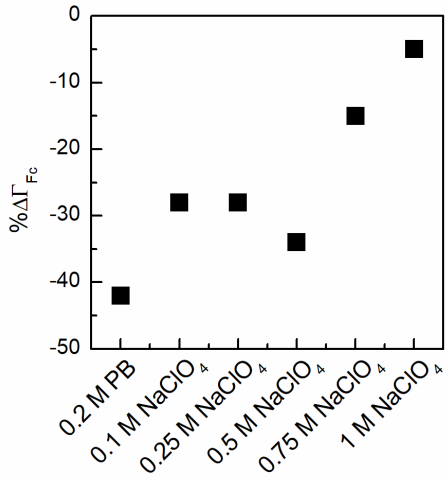

Figure 5.2: Change in Fc/Fc^+ CV peak charge of the same SAMs calculated from CVs collected in different electrolytes over a period of 120 min. The peak charge is assumed to be indicative of the surface coverage of the Fc-amides present in these ternary SAMs. SAMs with a larger negative $\%\Delta\Gamma_{Fc}$ undergo greater drift as compared to SAMs with a smaller $\%\Delta\Gamma_{Fc}$.

However, the pH 7 PB medium is considered to be more biocompatible with proteins than $NaClO_4$, as the ClO_4^- anion is a chaotropic agent (i.e., molecules that disrupt the hydration shell of protein and often as a consequence denature proteins) [19,192] and additionally, the ion-pairing of

Fc^+ with ClO_4^- is likely to hinder the redox mediation role of Fc^+ [177]. Since it was important to keep PB as the working electrolyte, several alternative approaches were examined in order to achieve a stable Fc/Fc^+ redox response, with the first one involving alteration of the terminal group of the diluent SAM (e.g., hydroxyl vs. carboxyl vs. methyl) to modify the local environment around the Fc^+ end group. The goal here is to stabilize the Fc/Fc^+ electrochemistry even in phosphate-containing solutions.

5.3 Fc/Fc^+ activity of Fc-amide binary thiolate SAMs

5.3.1 First few cycles of CV response of Fc-amide binary SAMs in perchlorate solutions

In Section 5.2, the stability of the Fc/Fc^+ peak charge during CV measurements was shown to be excellent in unbuffered perchlorate solutions, presumed to be due to the stabilizing effect of ion-pairing of the perchlorate ion and Fc^+ [153,165,166,171]. However, the SAMs (and the eventual TLR4-based sensor) must be operational in buffered solutions for two reasons. Firstly, the TLR4 immunoprotein is immobilized on the chemically-modified SAMs via a chelating agent, with the bond strength being pH-dependent, as previously described in Sections 4.1, respectively. Secondly, ClO_4^- is a chaotropic agent that may denature the TLR4 immunoprotein [19,192]. Thus, in this section, the electrochemistry was carried out in PB solution, but the SAM itself was altered, with the terminal groups of the diluent SAM varied to determine whether this might help to stabilize the Fc^+ moiety and hence the Fc/Fc^+ electrochemistry. To ensure better control of the microenvironment of the Fc/Fc^+ group, binary SAMs (rather than ternary SAMs) were prepared. This approach was expected to aid in minimizing the Fc-Fc lateral interactions and maximizing the Fc-diluent terminal group interactions. To better understand the stability of Fc^+ as a function

of microenvironment (as controlled by the terminal functional groups of diluent thiols), it was important to ensure that the Fc^+ groups are adjacent to the desired terminal groups but not other Fc groups, which is why we aimed to minimize the Fc-Fc lateral interactions.

Three distinct binary Fc-amide SAMs were prepared using MUO, MUA, and DDT as the diluents, as shown in Figure 5.3a, b, and c, respectively. MUA was chosen because its terminal carboxylate anion (pH > 7) could potentially stabilize the Fc^+ group [121]. DDT (dodecanethiol, $C_{11}SH$) was chosen because its hydrophobic terminal methyl group could potentially restrict the access to destabilizing anions (such as HPO_4^{2-}, $H_2PO_4^-$, CN^- and others discussed in Section 5.1), while MUO was chosen as a control for comparison against MUA and DDT.

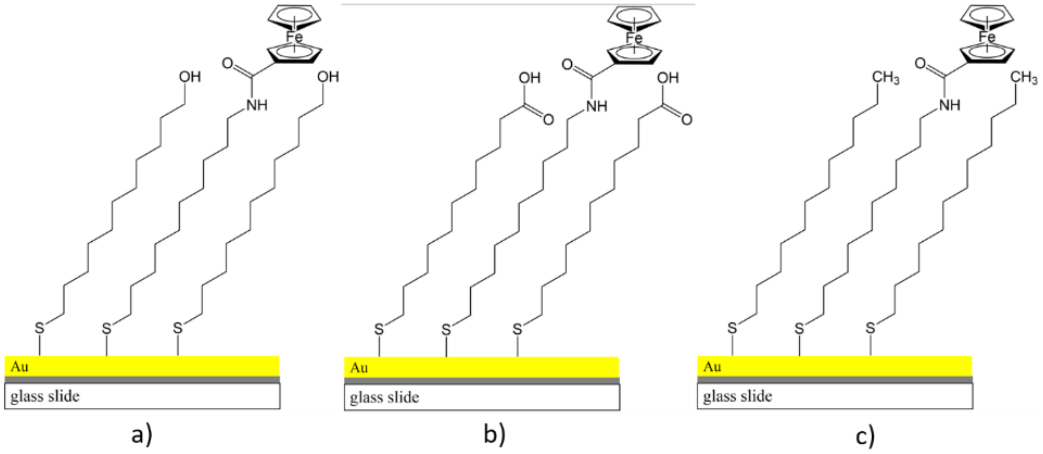

Figure 5.3: Fc-amide binary SAMs with a) 11-mercaptoundecanol (MUO), b) 11-mercaptoundecanoic acid (MUA), and c) 1-dodecanethiol (DDT) as the diluent SAM.

The ethanolic solution compositions of the MUO/Fc-amide, MUA/Fc-amide, and DDT/Fc-amide binary SAMs tested in the majority of this part of the work are shown in Table 5.2. Note that the percent of Fc-amide in the SAM deposition solution was varied from 0.5 – 25 % for the different binary SAMs in an attempt to surface immobilize ~1 % of the redox active molecule, for the reasons stated above (i.e., to minimize the Fc-Fc lateral interactions). This difference between

the solution and surface compositions for each of the binary SAMs is a result of the different affinities and surface binding chemistries that these thiols have shown experimentally [120,137,164,193].

Table 5.2: Typical composition of ethanolic thiol solutions used to prepare binary Fc-amide SAMs tested electrochemically in Section 5.3.

	% (v/v) 1 mM Fc-amide	% (v/v) 1 mM MUO	% (v/v) 1 mM MUA	% (v/v) 1 mM DDT
MUO/Fc-amide	2	98	-	-
MUA/Fc-amide	0.5	-	99.5	-
DDT/Fc-amide	25	-	-	75

The preparation of the desired binary SAMs with similar Fc-amide compositions was confirmed from CVs collected in 1 M $HClO_4$. A strong acid was selected to avoid deactivation of Fc^+ by OH^- present in solution, as observed in the literature [165,167]. Notably, the use of 1 M $HClO_4$ as a supporting electrolyte in the electrochemical testing of Fc-thiolate SAMs on Au is common, giving indistinguishable CV responses in $HClO_4$ and $NaClO_4$ solutions [194,195]. Example 500 mV/s CVs of the MUO/Fc-amide, MUA/Fc-amide, and DDT/Fc-amide binary SAMs are shown in Figure 5.4. The Fc surface coverage, peak width, and peak potential values, as well as the double layer capacitance values of the binary SAMs, are summarized in Table 5.3.

In Table 5.3, the Γ_{Fc} values indicate that ~1 % Fc-amide thiol was immobilized, as desired [130], anticipated to result in minimal Fc-Fc lateral interactions. This is confirmed by the observed ~90 mV CV peak widths (except for DDT), which are expected for the one electron electrochemistry of immobilized redox-active molecules without any perturbation by lateral interactions [114]. The observed similar double layer capacitance values for all three SAMs point to a similar SAM packing quality, as the capacitance is linearly proportional to the dielectric

constant and inverse of the thickness of SAMs [114]. The capacitance values obtained with these SAMs are also similar to those seen for ternary 5 % Fc-amide SAMs (in 0.2 M PB pH 7.0), as shown in Table 4.2.

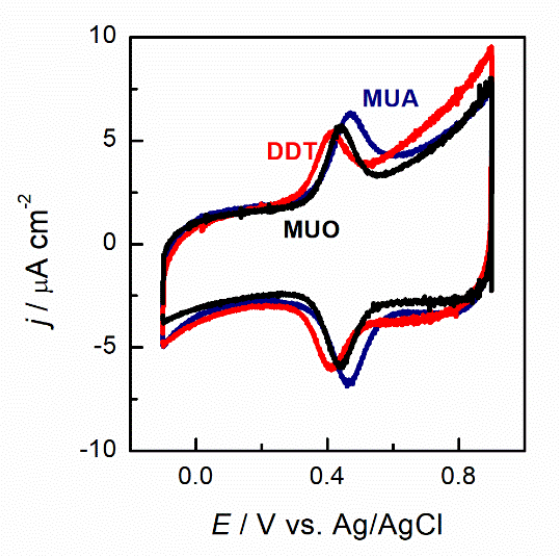

Figure 5.4: A single (early) CV scan of MUO/Fc-amide (black trace), MUA/Fc-amide (red trace) and DDT/Fc-amide (blue trace) binary SAMs collected at 500 mV/s in 1 M $HClO_4$. The Fc thiol surface coverage of these SAMs is estimated as ~1 % (calculated from the CV peak charge).

The CV peak potentials vary notably for these binary SAMs, indicating a change in the microenvironment around the Fc/Fc^+ terminal group and thus in its redox thermodynamics. During the oxidation of Fc to Fc^+, all in the same electrolyte, the dipoles associated with both terminal groups and solvent molecules will reorient to accommodate the Fc^+ cation. Hence, the easier it is for the dipoles to reorient around the cation, the more thermodynamically stable the Fc^+ moiety will be and thus the lower its redox potential should be. Creager *et al.* refer to this ability of the microenvironment to reorient around Fc^+ as interfacial polarity, which is often quantified as the dielectric constant (ε, where larger values mean that the environment has greater polarity). Creager *et al.* determined that the interfacial dielectric constant (ε = 10-50) at the terminal group / electrolyte interface is lower than that of the bulk solution (ε = 78). The same authors demonstrated

that the interfacial ε changes from 26 to 48 as the terminal group of the major component of SAMs is altered from -CH_3 to -OH, and according to the Born equation, this difference in interfacial ε was considered the sole cause of the ~100 mV negative shift in the peak potential seen in the CVs of terminal-Fc/Fc^+ SAMs [135,136]. For our binary SAMs, the ascending order of interfacial polarity is DDT/Fc-amide < MUO/Fc-amide < MUA/Fc-amide), which predictably matches the descending order of the CV peak potentials, (i.e., DDT /Fc-amide > MUO/Fc-amide > MUA/Fc-amide).

Table 5.3: Fc surface coverage (Γ_{Fc}, 1st column), CV peak width (ΔE_{fwhm}, 2nd column), CV peak potential (E_p, 3rd column) and double layer capacitance values (C_{dl}, 4th column) obtained at 0.1 V for MUO/Fc-amide, MUA/Fc-amide, and DDT/Fc-amide binary SAMs from a single (early) CV scan.

	Γ_{Fc}[a] / 10^{-12} mol cm^{-2}	ΔE_{fwhm}[a] / mV	E_p[a] / mV vs. Ag/AgCl	C_{dl}[b] / μF cm^{-2}
MUO/Fc-amide (N = 3)	6.2 ± 1.9	94 ± 2	427 ± 19	4.3 ± 0.9
MUA/Fc-amide (N = 3)	4.9 ± 1.4	101 ± 8	385 ± 21	3.7 ± 0.1
DDT/Fc-amide (N = 3)	6.3 ± 1.5	109	447 ± 29	3.3 ± 1.0

a. Values are obtained from CVs collected in 1 M $HClO_4$ at 500 mV/s.
b. Values are obtained from CVs collected in 1 M $HClO_4$ at 100, 500 and 2000 mV/s.

In the following section, the CVs of these binary SAMs, collected in 0.2 M PB (pH 7.0), are shown, with the potential at which the EIS data were collected (E_{EIS}) being the peak potentials in 0.2 M PB (pH 7.0). It is important to determine the peak potential, as the drift of the electrochemistry of the binary SAMs is measured by collecting EIS data every 20 min for 120 min, which is similar to the method utilized to track the drift of the SAMs examined in Chapter 4.

5.3.2 First few cycles of CV response of Fc-amide binary SAMs in PB solution

The CV responses of MUO/Fc-amide, MUA/Fc-amide, and DDT/Fc-amide SAMs having the identical composition as those studied in Section 5.3.1, collected at 100 mV/s in 0.2 M PB solution, are shown in Figure 5.5. The peak potential and potential at which electrochemical impedance spectroscopy data were collected for the binary SAMs are summarized in Table 5.4.

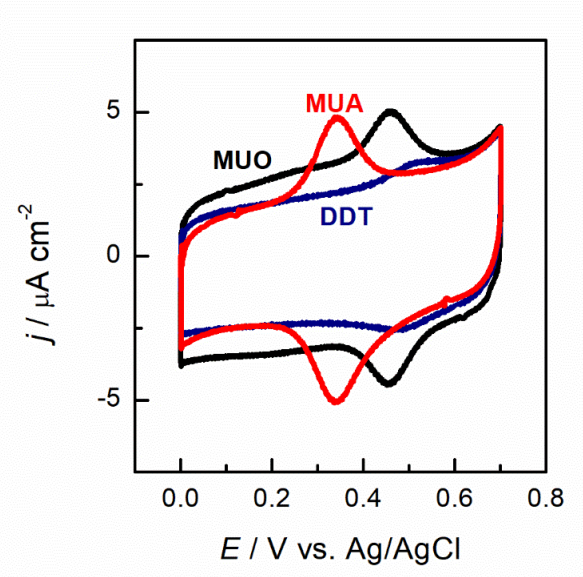

Figure 5.5: A single (early) CV scan of MUO/Fc-amide (black trace), MUA/Fc-amide (red trace) and DDT/Fc-amide (blue trace) binary SAMs collected at 500 mV/s in 0.2 M PB (pH 7.0). These SAMs are prepared using the same respective solution compositions as the Section 5.3.1.

In order to explore the deprotonation of the carboxylic acid functional group in MUA/Fc-amide binary SAMS, CVs were collected in PB at pH values ranging from 6.0-8.2, where PB acts as a buffer. The peak potential values as a function of solution pH were extracted from these CVs and are plotted in Figure 5.6. The pH dependence of Ep studied in this section is only observed for MUA binary SAMs and is not seen for MUO binary SAMs. The pH affects MUA because its pKa is 6-7, which means that the the degree of protonation of this carboxylic acid changes significantly at around these pH values [121]. At higher pH, carboxylic acids increasingly deprotonate to form

carboxylate anions, thereby introducing negative charges around Fc/Fc+, which stabilize the cationic form and manifest as more negative peak potential values. Lennox *et al.* refer to this phenomena as "Neighboring charge effects" [121,196]. Figure 5.6 shows that MUA/Fc-amide SAMs experience a 17 mV negative shift in peak potential as the pH of 0.2 M PB increases from 6.0 to 7.0, which suggests that, at neutral pH, some terminal carboxylic acid groups are deprotonated and negatively charged.

In Section 4.1.2, the criterion for the selection of the polarization potential used during EIS testing was that it should be in the region of the 'foot of the mediation voltammetric wave' (typically ~85 mV cathodic of the peak potential measured in 0.2 M PB). This particular potential was chosen to remain consistent with the criterion utilized for our published sensors [143]. This is assuming that the CV peak width remains constant for the different binary SAMs and for both the binary and ternary SAMs. The peak potential values and the respective EEIS values for the binary Fc-amide SAMs are summarized in Table 5.4.

Table 5.4 shows that the peak potential values of the binary SAMs follow an identical trend to the one discussed in the previous section, with the sequence shown to be DDT/Fc-amide > MUO/Fc-amide > MUA/Fc-amide. An interesting, but predictable, observation from the peak potentials of MUO/Fc-amide and DDT/Fc-amide SAMs is that they are lower in 1 M $HClO_4$ than in the 0.2 M PB pH 7.0 solution (Tables 5.2 and Table 5.3, respectively). This is attributed to the ion-pairing ability of perchlorate anions with Fc^+, resulting in a thermodynamically more stable complex [166]. The MUA/Fc-amide binary SAMs are an exception to this trend because, in 0.2 M

PB (pH 7.0), the carboxylic acid terminal group is most likely deprotonated and the resulting carboxylate anion may provide thermodynamic stability to Fc^+, as is noted in the literature [121].

In order to explore the deprotonation of the carboxylic acid functional group in MUA/Fc-amide binary SAMS, CVs were collected in PB at pH values ranging from 6.0-8.2, where PB acts as a buffer. The peak potential values as a function of solution pH were extracted from these CVs and are plotted in Figure 5.6. The pH dependence of E_p studied in this section is only observed for MUA binary SAMs and is not seen for MUO binary SAMs. The pH affects MUA because its pK_a is 6-7, which means that the the degree of protonation of this carboxylic acid changes significantly at around these pH values [121]. At higher pH, carboxylic acids increasingly deprotonate to form carboxylate anions, thereby introducing negative charges around Fc/Fc^+, which stabilize the cationic form and manifest as more negative peak potential values. Lennox *et al.* refer to this phenomena as "Neighboring charge effects" [121,196]. Figure 5.6 shows that MUA/Fc-amide SAMs experience a 17 mV negative shift in peak potential as the pH of 0.2 M PB increases from 6.0 to 7.0, which suggests that, at neutral pH, some terminal carboxylic acid groups are deprotonated and negatively charged.

In Section 4.1.2, the criterion for the selection of the polarization potential used during EIS testing was that it should be in the region of the 'foot of the mediation voltammetric wave' (typically ~85 mV cathodic of the peak potential measured in 0.2 M PB). This particular potential was chosen to remain consistent with the criterion utilized for our published sensors [143]. This is assuming that the CV peak width remains constant for the different binary SAMs and for both the binary and ternary SAMs. The peak potential values and the respective E_{EIS} values for the binary Fc-amide SAMs are summarized in Table 5.4.

Table 5.4: CV peak potential (E_p, 1st column) obtained for MUO/Fc-amide, MUA/Fc-amide, and DDT/Fc-amide binary SAMs and respective potential at which EIS data are collected (E_{EIS}) from a single (early) CV scan .*

	E_p / mV vs. Ag/AgCl	E_{EIS} / mV vs. Ag/AgCl
MUO/Fc-amide	459 ± 3 (N = 3)	375
MUA/Fc-amide in pH 7.0	344 ± 3 (N = 3)	255
DDT/Fc-amide	520	435
MUA/Fc-amide in pH 6.0	361 ± 2 (N = 3)	274
MUA/Fc-amide in pH 8.2	326 ± 5 (N = 3)	242

* Sample 500 mV/s CVs collected in 0.2 M PB (pH 7.0) from which E_p values are obtained are shown in Figure 5.5.

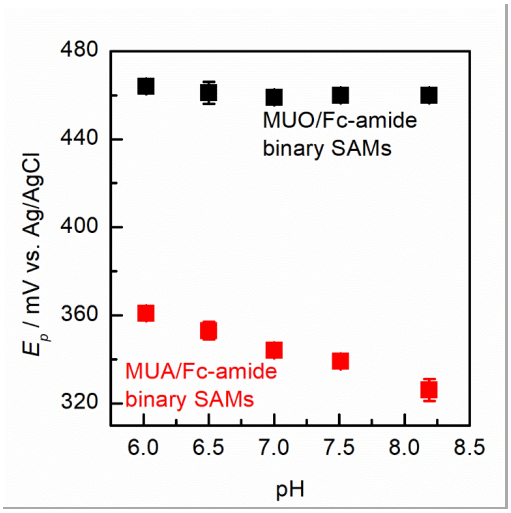

Figure 5.6: Peak potential values (N = 3) of MUO/Fc-amide (black) and MUA/Fc-amide binary SAMs taken from the first CV scan collected in 0.2 M PB at pH 6.0, 6.5, 7.0, 7.5 and 8.2.

5.3.3 Stability of EIS response of binary Fc-amide SAMs

The susceptibility of these Fc-amide binary SAMs to drift (which is directly related to loss of the redox response of the immobilized-Fc groups within the SAM) was determined by collecting EIS data every 20 min for 120 min at the appropriate E_{EIS} values at frequencies from 1 MHz to 0.1 Hz in 5 mM $Fe(CN)_6^{4-}$ + 0.2 M PB, as was also done in Chapter 4 (however, in this section, the

subsequent mediation CVs were not collected) and also in our prior work [18,143]. Typical Nyquist plots of MUO/Fc-amide, MUA/Fc-amide, and DDT/Fc-amide SAMs in 5 mM $Fe(CN)_6^{4-}$ + 0.2 M PB (pH 7.0) are shown in Figure 5.7.

Table 5.5 provides the charge-transfer resistances extracted from the Nyquist plots at t = 0 and 120 min (1st and 2nd columns, respectively), along with the observed drift in R_{CT} over the entire 120 min. Before comparing the drift between the various binary SAMs, it is important to note the differences in the EIS response for the binary and ternary Fc-amide SAMs in Section 4.3. Firstly, the charge-transfer resistance at t = 0 min for the ternary SAMs is ~1/3 of that of the binary SAMs due to a ~3 times higher Fc surface coverage. The exception is the DDT/Fc-amide binary SAMs, which have a much larger resistance than both the MUA/Fc-amide and MUO/Fc-amide binary SAMs, despite having a similar Fc content. Secondly and finally, the drift of the binary SAMs is smaller in magnitude than that observed for the ternary SAMs (with 5 % Fc-amide deposition, as shown in Section 4.2). This is because of the milder electrochemical testing conditions used here, as mediation CVs in 5 mM $Fe(CN)_6^{4-}$ + 0.2 M PB were not collected after EIS data collection, which means that the amount of time Fc is present in its oxidized form (i.e., the form that deactivates) is decreased. Mediation CVs were not carried out because a high anodic potential of 0.7 V may cause the formation of defects in the SAM to a degree that likely depends on the original packing quality of the SAMs [151].

In Table 5.5, when comparing the drift (i.e., $\%\Delta R_{CT}$) seen for the various binary SAMs, no overall trend is observed . This suggests that, despite the effect that the terminal functional groups have on the thermodynamics of Fc/Fc^+ electrochemistry (as shown in both Sections 5.3.1 and 5.3.2), ultimately, these binary SAMs are equally susceptible to unwanted drift in the EIS-determined polarization resistance. This indicates that the alteration of the microenvironment by

the modification of the terminal functional groups surrounding the Fc-amide groups and then testing in 5 mM $Fe(CN)_6^{4-}$ + 0.2 M PB (pH 7.0) solution was an unsuccessful strategy in curbing the drift of R_{CT}.

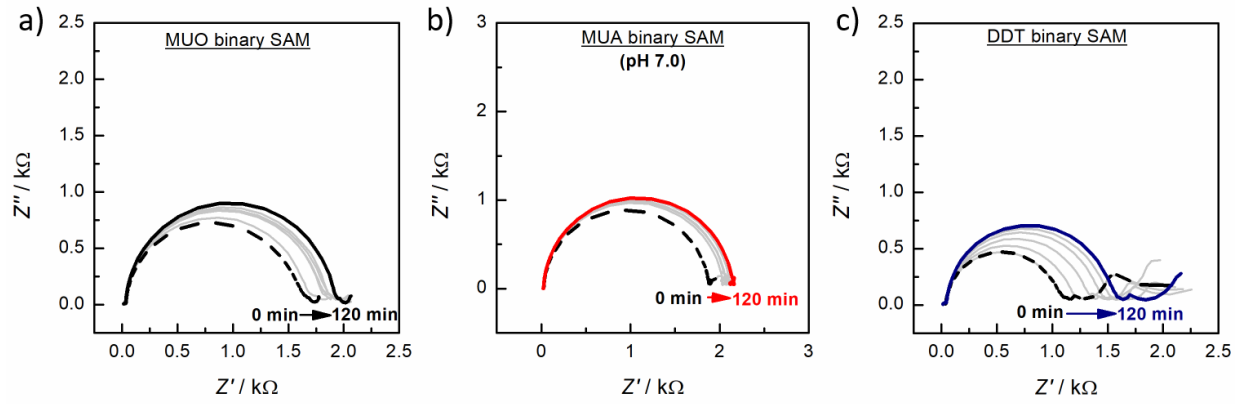

Figure 5.7: EIS response of binary (a) MUO/Fc-amide, (b) MUA/Fc-amide, and (c) DDT/Fc-amide binary SAMs at t = 0 min (black dashed line), drift after 20 - 100 min (grey) and 120 min (black (MUO), red (MUA), and blue (DDT) solid lines) in 5 mM $K_4Fe(CN)_6$ + 0.2 M PB. Data collected every 20 min at 0.375, 0.255, and 0.435 V, respectively, from 1 MHz to 0.1 Hz.

Table 5.5: Charge-transfer resistance and its drift of Fc-amide binary and ternary SAMs in 120 min in PB solution

	$R_{CT,\ 0\ min}$ / Ω	$R_{CT,120\ min}$ / Ω	$\%\Delta R_{CT}$
MUO/Fc-amide (N = 3)	(1.5 ± 0.5) x 10^3	(1.7 ± 0.5) x 10^3	9 ± 6 %
MUA/Fc-amide (N = 3)	(2.2 ± 0.5) x 10^3	(2.3 ± 0.4) x 10^3	5 ± 8 %
DDT/Fc-amide (N = 3)	(4.5 ± 3.0) x 10^3	(5.5 ± 3.7) x 10^3	31 ± 35 %

***** EIS response of SAMs at t = 0 (1st column) and 120 min (2nd column) in 5 mM $K_4Fe(CN)_6$ + 0.2 M PB solution and calculated drift of R_{CT} (3rd column). Data obtained from Nyquist plots in Figure 5.7.

In the following section, a third strategy was employed to attempt to retain the Fc/Fc^+ redox activity, i.e., the full CV peak charge with time of testing while doing this work in the bio-compatible pH 7 phosphate buffer solution. It will be shown that, when the Fc-amide thiol molecule is replaced with a FcC_{11} thiol, i.e., by removing the linking amide group (refer to Figure

5.8), the drift in the Fc/Fc^+ electrochemical response and peak charges was almost eliminated. This will be explained as arising from differences in the electronic properties of these two Fc-containing thiols as well as the nature of the covalent bond connecting Fc to the alkanethiolate SAM. It will also be demonstrated that replacing the amide with an alkyl linkage in the Fc thiol is a potential solution to the drift problem exhibited both by the Fc-containing SAMs themselves and the TLR-based sensors, which rely fully on the presence of a stable Fc electrochemical response.

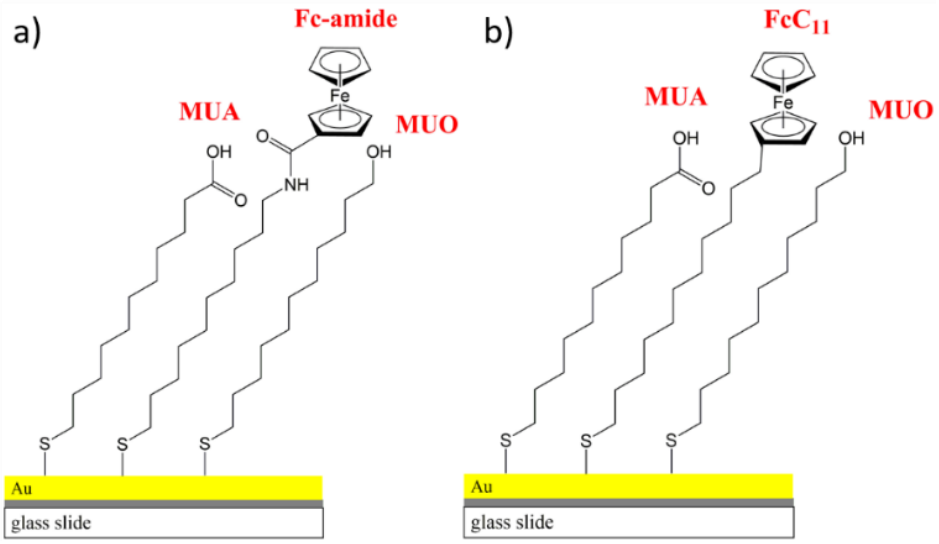

Figure 5.8: Ternary Fc-thiolate SAMs composed of (a) MUA, MUO and Fc-amide, and (b) MUA, MUO and FcC_{11} thiols.

5.4 Stability of immobilized-Fc of ternary Fc-amide vs. ternary FcC_{11} SAMs in PB solution

In Section 5.1, the gradual loss of the Fc/Fc^+ CV charge observed with the ternary Fc-amide-containing SAMs was mitigated by substituting the 0.2 M PB (pH 7.0) electrolyte with 1 M $NaClO_4$, interpreted as indicating that the ion-pairing ability of ClO_4^- stabilizes the Fc^+ group during electrochemical measurements. Conversely, in Section 5.2, it was discovered that Fc^+ could not be stabilized in PB by altering the terminal functional groups of the neighboring (predominant) thiols in the SAMs.

In this section, the substitution of the Fc-component by a different Fc thiol in the ternary SAMs investigated in this thesis work was studied. Specifically, the Fc-amide thiol was replaced with a FcC_{11}, having approximately the same carbon chain length, but without the amide linkage. The approach of replacing an amide group with a methyl linkage group was taken because it was shown by Abraham *et al.* [197], and Batterjee *et al*. [198] that methyl groups on the Cp rings increase the electron density on the Fe(III) center of the Fc^+ group, which results in an improvement in its stability [181]. Moreover, it is also possible that the lack of an amide linkage group in FcC_{11} may prevent the hydrolysis of this group, which would be expected to remove the Fc group from the SAM. Figure 5.8a and b show both the ternary Fc-amide and FcC_{11} thiolate SAMs studied in this section.

Ternary SAMs having the same composition as used in most of Chapter 4 (5 % (v/v) 1 mM Fc thiol molecule, 30 % (v/v) 1 mM MUA and 65 % (v/v) MUO) were prepared using either Fc-amide or FcC_{11} thiols to introduce the Fc group into the SAMs. Their electrochemical responses were then investigated as usual, namely by collecting three CVs at 100, 250, and 500 mV/s (in that order), all in 0.2 M PB (pH 7.0). Typical CVs are shown in Figure 5.9 and the estimated Fc surface coverage (1^{st} column), peak width (2^{nd} column), double-layer capacitance (3^{rd} column) and peak potentials (4^{th} column), extracted from these CVs are shown in Table 5.6.

In Table 5.6, the larger Fc surface coverage seen for the FcC_{11} SAMs compared to the Fc-amide SAMs is most likely due to the larger relative hydrophobicity of the dissolved FcC_{11} thiol molecule in EtOH (due to the lack of an amide group), resulting in a greater thermodynamic drive for its immobilization on the Au substrate [153]. The higher FcC_{11} coverage could also explain the wider Fc/Fc^+ redox peaks seen, as higher surface concentrations of Fc thiols will increase the probability of the presence of repulsive Fc-Fc lateral interactions.

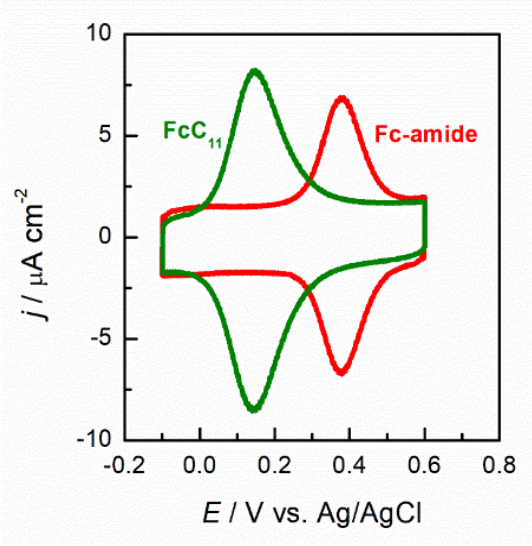

Figure 5.9: CV comparison of ternary Fc-amide (red) and FcC_{11} (green) SAMs collected at 500 mV/s in 0.2 M PB (pH 7.0).

As seen in Figure 5.9 and Table 5.6, the Fc/Fc^+ redox peak potentials for the FcC_{11} SAMs are more negative than those of the Fc-amide SAMs by roughly 230 mV. This is likely due to the electron donating nature of the alkane chain, which would increase the electron density at the Fe(III) center, resulting in enhanced thermodynamic stability of Fe(III) and, by extension, of Fc^+. Similarly, the electron-withdrawing property of the amide functionality of Fc-amide has been shown to move the Fc oxidation peak potential positively [197]. Despite the possibility of conjugation between the amide and Fc Cp rings, the more negative Fc redox potential as a result of the substituent functional group on the Cp ring is considered to arise primarily from inductive effects [198].

A very positive result of the substitution of Fc-amide by FcC_{11} is the observed stability of the Fc redox peaks, as seen in Figure 5.10. The stability was tracked using the same method as in Section 5.1 by collecting three CVs at each of 100, 250, and 500 mV/s (in that order) every 20 min for 120 min in 0.2 M PB (pH 7.0). The $\%\Delta\Gamma_{Fc}$ over 120 min for the Fc-amide and FcC_{11} SAMs is

-23 % and 0 %, respectively, clearly showing that, in otherwise identical microenvironments (similar composition of SAMs and identical electrolyte solution), the Fc redox activity of the FcC_{11} SAMs is significantly more stable than seen for the Fc-amide SAMs, even in PB solutions. This is in agreement with predictions made in earlier literature [181], which have shown that, the higher the electron density in the vicinity of the Fc^+ moiety, e.g., due to substituent inductive effects, the more stable the Fc/Fc^+ redox chemistry should be.

Table 5.6: Fc surface coverage (1st column), peak width (2nd column), double-layer capacitance measured at -0.1 V (3rd column) and peak potential (4th column) of ternary Fc-amide and FcC_{11} SAMs in 0.2 M PB (pH 7.0) solutions.*

	Γ_{Fc} / 10^{-12} mol cm^{-2}	ΔE_{fwhm} / mV	C / µF cm^{-2}	E_p / mV vs. Ag/AgCl
ternary Fc-amide SAMs (N = 1)	12.8	112	2.9	374
ternary FcC_{11} SAMs (N = 1)	21.4	139	2.7	140

*Example CVs, from which these values are extracted, collected in 0.2 M PB (pH 7.0) are shown in Figure 5.9.

Another interpretation of these results is related to the possible hydrolysis of the linking amide group in the earlier Fc-thiolate design, causing the Fc group to be removed from the thiol entirely, thus losing its electrochemistry and seen as drift of the sensor. Amide hydrolysis can involve both acid- and base-catalyzed mechanisms, both of which involve a nucleophilic attack on the carbon of the carbonyl group. It is possible that, when Fc is oxidized to Fc^+, the carbon of the carbonyl group holds a greater partial positive charge, making it more prone to a nucleophilic attack and thus hydrolysis, resulting in the liberation of Fc from the alkanethiolate SAM. Possible acid- and base-catalyzed mechanisms of hydrolysis of Fc-amide are shown in Scheme 5.1a and b, respectively, although it is not certain which of these could occur in pH 7.0 buffered solutions. In

this thesis work, there is no certain evidence favoring either nucleophilic attack of Fc^+ or hydrolysis of Fc-amide as the cause of deactivation of Fc/Fc^+ electrochemistry.

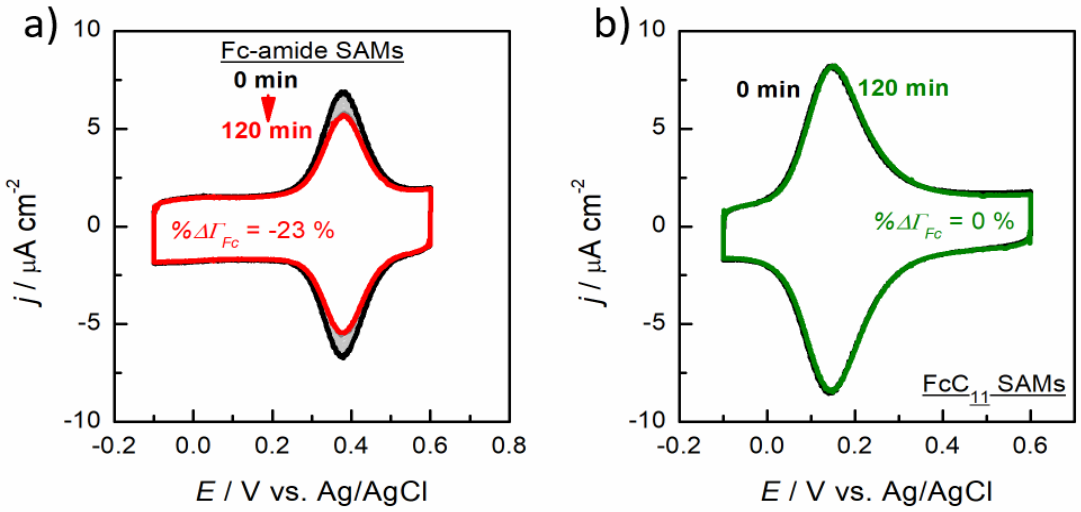

Figure 5.10: Electrochemical response of ternary (a) Fc-amide and (b) FcC_{11} SAMs at t = 0 min (black), 20-100 min (grey), and 120 min (for both Fc-amide (red) and FcC_{11} (green)) collected in 0.2 M PB (pH 7.0) at 500 mV/s.

To verify whether this very good stability of the Fc/Fc^+ electrochemistry of the alkyl-Fc based SAM translates also to a stable SAM for use in the TLR-based sensors, in the next section, TLR4-based sensors were prepared using the FcC_{11} binary SAMs, rather than the Fc-amide SAMs. It will be shown that the sensor response to LPS is now significant more pronounced than its drift, which was the goal of this thesis work.

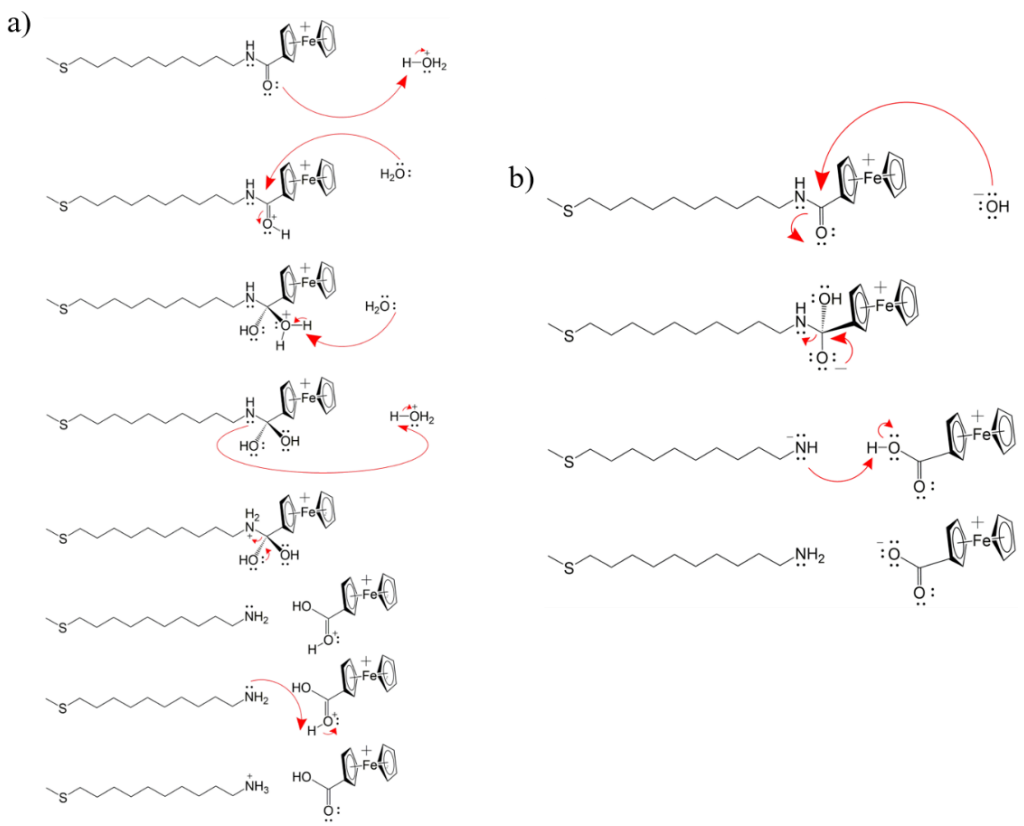

Scheme 5.1: Proposed mechanism of (a) acid- and (b) base-catalyzed hydrolysis of Fc-amide.

5.5 TLR4-based sensor prepared using ternary FcC_{11} SAMs

The data in this section were collected together with Dr. Armando Marenco using SAMs composed of 11-(Ferrocenyl)undecanethiol (FcC_{11}), *N*-[N_{α},N_{α}-Bis(carboxymethyl)-L-lysine]-12-mercaptododecanamide (NTA-thiol) and 11-mercaptoundecanol (MUO). In these SAMs, the role of the FcC_{11} component is to allow the electrochemical mediation of $Fe(CN)_6^{4-}$ oxidation in solution, while the role of the NTA-thiol is to chelate Ni^{2+} and allow for the immobilization of poly-Histidine Tagged TLR4/MD-2, and the role of MUO is to serve as a spacer thiol. The NTA-thiol plays the same role as MUA did in the published sensor work from the Birss group [16,18], which was immobilization of the TLR4 immunoprotein, as described in detail in Section 4.1.1.

The composition of these SAMs was 5 % (v/v) 1 mM FcC_{11}, 30 % (v/v) 1 mM NTA-thiol, and 65 % (v/v) 1 mM MUO, identical to the composition used in the original paper [18], as shown in Figure 5.11.

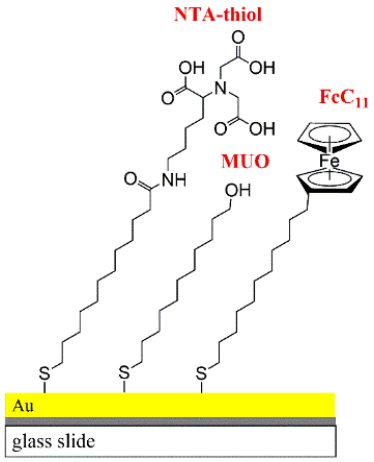

Figure 5.11: Ternary FcC_{11} SAMs composed of 11-(Ferrocenyl)undecanethiol (FcC_{11}), N-[N_{α},N_{α}-Bis(carboxymethyl)-L-lysine]-12-mercaptododecanamide (NTA-thiol) and 11-mercaptoundecanol (MUO).

The electrochemical testing protocol of our sensor involved collecting EIS data at 0.200 V (in the 'foot of the voltammetric mediation wave' region) from 1 MHz to 0.1 Hz, followed by CV studies at 250 and then 500 mV/s. The blank experiment consisted of performing this testing protocol every 20 min for 60 min without exposure to LPS. The response to LPS was then measured by exposure to increasing amounts of LPS every 20 min for 180 min, with concentrations ranging from 0.0128-5000 µg/mL.

The EIS response of the blank and exposure to LPS experiments is shown in Figure 5.12a and b, respectively. Figure 5.12a shows that the drift of these sensors from t = 0 to 60 min is +1 %, which is negligible, while Figure 5.12b shows that the response generated from exposure to 5 mg LPS/mL is + 57 %. Despite the lack of replicates, these preliminary sensor data are very

promising, as the response to LPS is significantly larger than its drift, thus meeting the goal of this chapter.

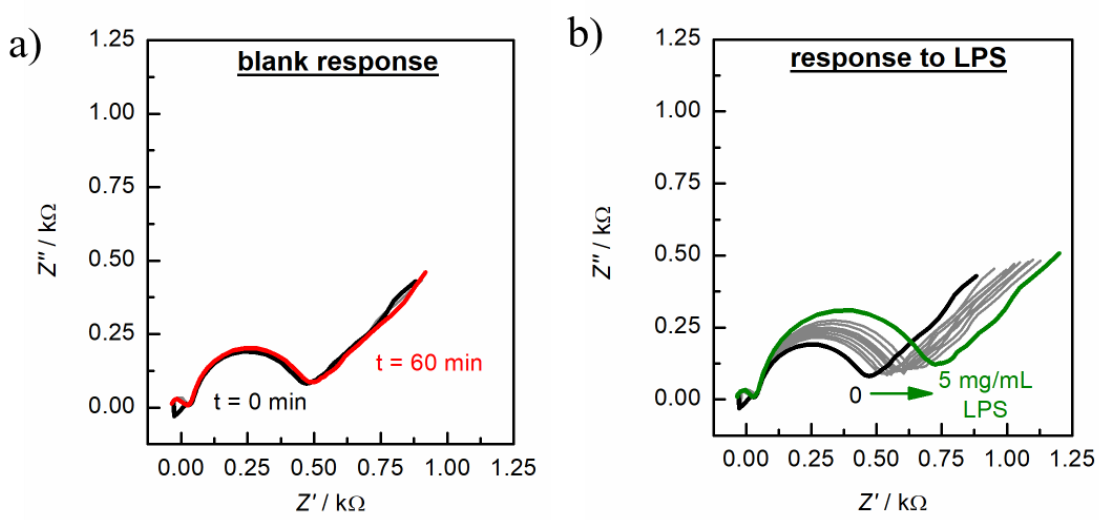

Figure 5.12: Electrochemical signal of a TLR4-based sensor in 5 mM $K_4[Fe(CN)_6]$ + 0.2 M PB (pH 7.0) collected at 0.200 V vs. Ag/AgCl at frequencies ranging from 1 MHz to 0.1 Hz. In (a), drift of this sensor was measured every 20 min from t = 0 (black trace) to 60 min (red trace). In (b), the response is measured prior to the addition of LPS to the surface of the electrode (baseline, black trace) and after the addition of up to a maximum concentration of 5 mg/mL LPS (green trace).

5.6 Summary

In Chapter 5, it was determined that the use of ClO_4^--containing solutions stabilizes the Fc/Fc^+ CV redox peaks, possibly due to its ion-pair forming capability with Fc^+, based on literature reports [166,177–179]. However, the use of high ionic strength ClO_4^--containing electrolytes was not considered a practical solution in minimizing the drift of our TLR4-based sensors as ClO_4^- is a known chaotropic agent, which are chemicals that disrupt the hydration shell of proteins and cause changes in their conformational structure [19,192]. Also, anions capable of forming ion-pairs with Fc^+ have been shown to have the potential to block the activity of the Fc/Fc^+ redox pair to catalyze solution redox reactions [177].

Thus, in another direction, binary MUO/Fc-amide, MUA/Fc-amide and DDT/Fc-amide SAMs were prepared in an attempt to minimize the deactivation of Fc/Fc^+ in 5 mM $Fe(CN)_6^{4-}$ + 0.2 M PB (pH 7.0) solutions. At the time, it was suspected that the presence of either a terminal -CH_3 or -COO^- group may minimize the interactions of Fc^+ with anions that may cause the loss of the Fc/Fc^+ electrochemistry. These binary SAMs were prepared in a manner such that approximately 1 % of the SAMs consisted of the Fc-amide component in order to minimize Fc-Fc lateral interactions. It was determined that changing the terminal group of the diluent SAM altered the thermodynamics of Fc/Fc^+ electrochemistry, but did not help to mitigate drift, as each of the binary SAMs investigated were found to be equally susceptible to a similar magnitude of drift.

The stabilization of Fc/Fc^+ in 0.2 M PB was ultimately achieved by substituting the Fc-amide thiol (of 5 % (v/v) Fc-thiol, 30 % (v/v) MUA and 65 % (v/v) MUO ternary SAMs) with a FcC_{11} thiol. This was attributed to two phenomena. Firstly, methylene linkage groups are electron-donating, which Sauvage *et al.* have shown to stabilize Fc^+ by increasing the electron-density of the d-orbitals of Fe(III) [181]. Secondly, for the amide-Fc thiol, the Fc moiety may be liberated from the surface via the hydrolysis of the amide linkage. As the methylene group should be significantly less prone to this attack, the FcC_{11} thiol should be less prone to deactivation, as seen experimentally. Using this new electroactive thiol component, a TLR4-based sensor was prepared, showing excellent stability and yet a reliable and stable response to LPS.

Chapter Six: Conclusions and future directions

6.1 Conclusions

In this thesis work, Ferrocene (Fc)-containing alkanethiolate Self-Assembled Monolayers (SAMs) with three components, 5 % (v/v) 11-mercaptodecylcarboxamide (Fc-amide), 30 % (v/v) 11-mercaptoundecanoic acid (MUA), and 65 % (v/v) 11-mercaptoundecanol (MUO), deposited on polycrystalline Au films on glass, were used to prepare Toll-like Receptor 4 (TLR4)-based sensors. The purpose of the Fc-amide component was to mediate electrons from the electrolyte to the underlying Au substrate, which decreases the charge-transfer resistance (R_{CT}) by three orders of magnitude to ≤ 1 kΩ, allowing for the potential use of this biosensor in field-deployable systems [18]. This sensor could detect heat-killed *Salmonella Typhimurium* (HKST) lysates from 1-10^5 cells/mL (i.e., the sensor experienced an increase in R_{CT} due to the dimerization of adjacent TLR4 caused by its binding interaction with lipopolysaccharides (LPS) released from Gram-negative bacteria). It was discovered in the present thesis work that a similar magnitude of increase in R_{CT} was experienced by the sensor in the presence as well as in the absence of HKST lysate cells. The primary focus of this thesis work was therefore to determine the cause of drift (Chapter 4) and remedy it so that we have a well-functioning TLR4-based biosensor (Chapter 5).

In Chapter 4, we concluded that the signal drift did not arise from either the linking layers (i.e., the chemical modifications made to the SAM for purpose of protein immobilization) or from the TLR4 immunoprotein, but rather from the underlying ternary SAMs, specifically the redox chemistry of its Fc-amide component. By increasing the proportion of the Fc-amide component in the SAM, it was determined that, despite the greater loss of Fc/Fc^+ redox activity, the double-layer capacitance remained relatively invariant, indicating that electrochemical instability of the Fc moiety, rather than Fc-amide surface desorption, was the likely cause of signal drift. Further

experiments, involving studying the effect of the length of incubation time of the unmodified SAM portion of the sensor at the open circuit potential (OCP), showed that the oxidized form of Fc (i.e., Fc^+) is electrochemically unstable under the conditions originally employed, for example, using pH 7 phosphate buffer (PB) solutions and, in particular, constructing the SAM by including the Fc-amide thiolate SAM component.

The literature on Fc-thiolate SAMs has shown that certain anions, which include $H_2PO_4^-$ and HPO_4^{2-}, comprising the pH 7 PB solutions, can cause irreversible damage to the Fc/Fc^+ electrochemistry [166,177]. There are other anions, for instance ClO_4^-, that form a 1:1 ion-pair with Fc^+, indicated to lead to the stabilization of the Fc/Fc^+ redox chemistry [136,137,171–176]. Therefore, in Chapter 5, electrochemical testing of the Fc-containing SAMs was performed in ClO_4^--containing solutions, instead of pH 7 PB (initially used to ensure biocompatibility with the TLR4 immunoproteins present in the completely assembled sensor), which showed that the deactivation of Fc/Fc^+ was either minimized significantly or eliminated entirely at high concentrations of ClO_4. However, this was considered an inadequate correction to the sensor drift problem because ClO_4^- is a chaotropic agent, defined as a chemical that denatures proteins by disrupting their hydration shell [19,192].

Thus, in subsequent efforts, the drift problem was examined by replacing the Fc-amide thiolate component (where the Fc-moiety is covalently-linked to the alkane chain via an electron-withdrawing amide group) within the ternary SAMs with FcC_{11} (11-(ferrocenyl)undecanethiol, where the Fc-moiety is covalently-linked to the alkane chain via an electron-donating methylene group). These new SAMs were shown in Chapter 5 to be immune to the loss of Fc/Fc^+ redox-activity in 0.2 M PB (pH 7.0). It has been demonstrated in the literature that covalently attaching electron-donating methyl groups to the Cp rings of Fc can increase the electrochemical stability of

Fc^+ [180,181], which might explain the better stability of the Fc/Fc^+ electrochemistry of the FcC_{11}-based SAMs compared to SAMs containing Fc-amide thiolates. Another possible explanation for this phenomenon was that Fc-amide may be prone to hydrolysis that could result in the liberation of Fc from the surface. Ternary SAMs, with one of the components being FcC_{11}, were then used in Chapter 5 to prepare a new TLR4-based sensor, which demonstrated negligible drift and responding well to variable LPS concentrations.

The substitution of Fc-amide with the more electrochemically stable FcC_{11}, in our new generation of ternary SAMs, has two important ramifications for TLR4-based sensors. Firstly, there should be a decrease in the generation of false-positives, and secondly, the sensors can now be used for longer periods of time for field-deployable purposes. The incorporation of an Fc component in the alkanethiolate SAMs is likely a better way to prepare low-interfacial resistance sensors than utilizing di-thiolate SAMs (which has been previously done to prepare such sensors) because the di-thiolate SAMs are known to contain more defects, which should increase non-specific adsorption and result in more problems with false-positives.

6.2 Future directions

(a) The SAM composition could be further modified to optimize the sensor response after TLR attachment. Specifically, the use of hydrophilic MUO as a spacer thiol in the TLR4-based sensor could be altered. According to Whitesides *et al.,* the -OH terminal group SAMs are not completely effective at inhibiting non-specific adsorption [77,78]. This suggests that this sensor may be prone to generating a signal in the presence of molecules that are structurally similar to LPS, such as dipalmitoylphosphatidylcholine, glucose, fructose, maltose, galactose, and mannan oligosaccharides [105,199,200]. This modification could also help to create a better profile of the

interaction between TLR4 and its target ligand to recognize the limitations of this sensor. For example, it would be useful to compare sensor responses prepared with MUO and with a poly(ethylene glycol)-terminated thiol component (considered to be the most effective spacer at inhibiting non-specific adsorption).

Such experiments are commonly referred to as negative control experiments, as TLR4 does not bind to molecules that are structurally similar to LPS (also known as interferents) and thus it would be expected that the TLR4-based sensor would not generate a response in the presence of such interferents. Similarly, another important set of experiments to be conducted are blank experiments (i.e., experiments in which the sample does not contain any molecule that may potentially bind to TLR4) to assess the response of the sensor in the absence of any interferents or LPS.

(b). Similarly, the use of SAMs based on compounds other than alkanethiols should be studied. It is known that alkanethiolate SAMs are unstable as they are prone to desorption at higher temperatures [201] or under illumination by Ultraviolet radiation [202], as compared to N-heterocyclic carbene (NHC) SAMs that can be stable in ambient conditions for up to a month [201]. The greater stability of NHC SAMs should permit long-term storage that would allow for transport of these electrodes, which expands the use of sensors prepared using NHC SAMs for on-site analysis without sacrificing functionality. This is a feature present in commercially-available glucose meters for diabetes management [203].

(c). Most importantly, further studies on the interaction of TLR and LPS could shed important details on their interactions. For example, in the work involved in this thesis, TLR4 was

a Pattern Recognition Receptor immobilized on SAMs to detect a Pathogen-associated molecular pattern called LPS that is present on the cell walls of a broad category of pathogens called Gram-negative bacteria [32–34]. Birss *et al.* have hypothesized that the increase in R_{CT} of their sensor, in the presence of either LPS or HKST lysate cells, is caused by TLR4 dimerization, thus restricting the access of electroactive solution ions to the interface [15,18]. A recent study demonstrated that LPS isolated from varying bacterial strains may induce differing TLR4 responses, i.e., either an agonistic or antagonistic response. For example, LPS from *Escherichia coli* and *Salmonella minnesota* induced an agonistic response that caused the dimerization of TLR4, whereas LPS from *Rhodobacter sphaeroides* induced an antagonistic response that caused TLR4 to remain monomeric [204]. This means that TLR4-based sensors may be unable to detect antagonistic LPS.

Furthermore, another recent study showed that TLR4 only recognizes LPS from the *Enterobacteriaceae* family [205]. Prior to developing future TLR4-based sensors, it would therefore be important to understand differences in the binding interaction between TLR4 and LPS for LPS obtained from different bacterial families and determine how this might influence the sensor response. Most importantly, comparing other broad biorecognition elements could be the basis to further advance the field of deployable biosensors.

(d) Another potential application of our TLR4-based biosensor could be the diagnosis of sepsis. Sepsis is the overreaction of the innate immune system caused by the presence of invasive pathogens and is the leading cause of death in intensive care units. LPS endotoxin is considered the most harmful biomolecule that causes the onset of sepsis symptoms. This sensor may have to be adapted slightly to be able to detect LPS in blood samples [206].

References

[1] S.P. Mohanty, E. Koucianos, Biosensors: A tutorial review, IEEE Potentials. 25 (2006) 35–40. doi:10.1109/MP.2006.1649009.

[2] O. Cenciarelli, A. Malizia, M. Marinelli, S. Pietropaoli, R. Gallo, F. D'Amico, C. Bellecci, R. Fiorito, A. Gucciardino, M. Richetta, P. Gaudio, Evaluation of biohazard management of the Italian national fire brigade, Def. S T Tech. Bull. 6 (2013) 33–41.

[3] T.R. Neal, Proliferation of weapons of mass destruction, Office of technology assessment washington dc, 1993. https://books.google.ca/books?id=8JSaXWcyzx8C.

[4] O. Cenciarelli, S. Rea, M. Carestia, F. D'Amico, A. Malizia, C. Bellecci, P. Gaudio, A. Gucciardino, R. Fiorito, Bioweapons and bioterrorism: A review of history and biological agents, Def. S T Tech. Bull. 6 (2013) 111–129.

[5] J.D. Simon, Biological terrorism: Preparing to meet the threat, J. Am. Med. Assoc. 278 (1997) 428–430. doi:10.1001/jama.278.5.428.

[6] G.M. Ludovici, V. Gabbarini, O. Cenciarelli, A. Malizia, A. Tamburrini, S. Pietropaoli, M. Carestia, M. Gelfusa, A. Sassolini, D. Di Giovanni, L. Palombi, C. Bellecci, P. Gaudio, A review of techniques for the detection of biological warfare agents, Def. S T Tech. Bull. 8 (2015) 17–26.

[7] Overcoming Challenges to Develop Countermeasures Against Aerosolized Bioterrorism Agents: Appropriate Use of Animal Models, National Academies Press, Washington, D.C., 2006. doi:10.17226/11640.

[8] D. Mussis, S.J. Amherst, C. Ecuyer, Biological warfare and bioterrorism: a historical review, 75246 (2004) 400–406.

[9] D.P. Greenwood, T.H. Jeys, B. Johnson, J.M. Richardson, M.P. Shatz, Optical techniques for detecting and identifying biological-warfare agents, Proc. IEEE. 97 (2009) 971–989. doi:10.1109/JPROC.2009.2013564.

[10] E. Švábenská, Systems for detection and identification of biological aerosols, Def. Sci. J. 62 (2012) 404–411. doi:10.14429/dsj.62.1251.

[11] S. Shafazand, R. Doyle, S. Ruoss, A. Weinacker, T.A. Raffin, Inhalational Anthrax, Chest. 116 (1999) 1369–1376. doi:10.1378/chest.116.5.1369.

[12] V. Agranovski, Z. Ristovski, M. Hargreaves, P.. Blackall, L. Morawska, Real-time measurement of bacterial aerosols with the UVAPS: performance evaluation, J. Aerosol Sci. 34 (2003) 301–317. doi:10.1016/S0021-8502(02)00181-7.

[13] M. Cenciarelli, O. Valentina G. Pietropaoli, S. Carestia, Use of Non-Pathogenic Biological Agents as Biological Warfare Simulants for the Development of a Stand-Off Detection System, J. Microb. Biochem. Technol. 06 (2014). doi:10.4172/1948-5948.1000172.

[14] R. Mayall, M. Renaud-young, V. Birss, Development of a TLR-4 electrochemical biosensor and a feasibility study of the Genefluidics Helios System – Final report for contract W7702-145656 / A, (n.d.).

[15] R.M. Mayall, M. Renaud-Young, E. Gawron, S. Luong, S. Creager, V.I. Birss, N.W.C. Chan, V.I. Birss, An electrochemical lipopolysaccharide sensor based on an immobilized Toll-Like Receptor-4, Biosens. Bioelectron. 4 (2017) 794–801. doi:10.1016/j.bios.2016.09.009.

[16] R.M. Mayall, M. Renaud-Young, N.W.C. Chan, V.I. Birss, An electrochemical lipopolysaccharide sensor based on an immobilized Toll-Like Receptor-4, Biosens. Bioelectron. 87 (2017) 794–801. doi:10.1016/j.bios.2016.09.009.
[17] A.J. Bard, L.R. Faulkner, V.S. Bagotsky, Electrochemical Methods Fundamentals of Electrochemistry, 2001.
[18] R.M. Mayall, M. Renaud-young, E. Gawron, S. Luong, S. Creager, V.I. Birss, Enhanced Signal Amplification in a Toll-like Receptor-4 Biosensor Utilizing Ferrocene-Terminated Mixed Monolayers, ACS Sensors. 4 (2018) 143–151. doi:10.1021/acssensors.8b01069.
[19] G. Salvi, P.D.L. Rios, M. Vendruscolo, Effective Interactions Between Chaotropic Agents and Proteins, 499 (2005) 492–499. doi:10.1042/bj1350559.
[20] K.R. Rogers, C.L. Gerlach, Environmental biosensors: A status report, Environ. Sci. Technol. 30 (1996) 486A-491A. doi:10.1021/es962481l.
[21] J. Colomer-Farrarons, P. Ll., A. Ivon, J. Samitier, Portable Bio-Devices: Design of electrochemical instruments from miniaturized to implantable devices, New Perspect. Biosens. Technol. Appl. (2011). doi:10.5772/17212.
[22] C.L. Morgan, D.J. Newman, C.P. Price, Immunosensors: technology and opportunities in laboratory medicine., Clin. Chem. 42 (1996) 193–209. doi:10.1016/j.cpha.2019.03.002.
[23] W. Pang, H. Zhao, E.S. Kim, H. Zhang, H. Yu, X. Hu, Piezoelectric microelectromechanical resonant sensors for chemical and biological detection, Lab Chip. 12 (2012) 29–44. doi:10.1039/C1LC20492K.
[24] A.P.F. Turner, Biosensors: Sense and sensibility, Chem. Soc. Rev. 42 (2013) 3184–3196. doi:10.1039/c3cs35528d.
[25] M. Drahansky, Liveness Detection in Biometrics, in: Adv. Biometric Technol., InTech, 2011: p. 13. doi:10.5772/17205.
[26] E. Abu Irhayem, H. Elzanowska, A.S. Jhas, B. Skrzynecka, V. Birss, Glucose detection based on electrochemically formed Ir oxide films, J. Electroanal. Chem. 538–539 (2002) 153–164. doi:10.1016/S0022-0728(02)01142-7.
[27] A.S. Jhas, H. Elzanowska, B. Sebastian, V. Birss, Electrochimica Acta Dual oxygen and Ir oxide regeneration of glucose oxidase in nanostructured thin film glucose sensors, 55 (2010) 7683–7689. doi:10.1016/j.electacta.2010.03.093.
[28] H.B. Campbell, H. Elzanowska, V.I. Birss, Biosensors and Bioelectronics Towards a reliable and high sensitivity O 2 -independent glucose sensor based on Ir oxide nanoparticles, Biosens. Bioelectron. 42 (2013) 563–569. doi:10.1016/j.bios.2012.11.023.
[29] R.B. Thomson, One small step for the gram stain, one giant leap for clinical microbiology, J. Clin. Microbiol. 54 (2016) 1416–1417. doi:10.1128/JCM.00303-16.
[30] R. Coico, Gram Staining, in: Curr. Protoc. Microbiol., John Wiley & Sons, Inc., Hoboken, NJ, USA, 2005. doi:10.1002/9780471729259.mca03cs00.
[31] P.W. Bruce Alberts, Alexander Johnson, Julian Lewis, Martin Raff, Keith Roberts, Molecular Biology of the Cell, 4th ed., Garland Science, New York, 2002.
[32] C. Whitfield, M. Stephen Trent, Biosynthesis and export of bacterial lipopolysaccharides, Annu. Rev. Biochem. 83 (2014) 99–128. doi:10.1146/annurev-biochem-060713-035600.
[33] P. Sondhi, M.H.U. Maruf, K.J. Stine, Nanomaterials for Biosensing Lipopolysaccharide, Biosensors. 10 (2019) 2. doi:10.3390/bios10010002.
[34] S. Wright, R. Ramos, P. Tobias, R. Ulevitch, J. Mathison, CD14, a receptor for complexes

of lipopolysaccharide (LPS) and LPS binding protein, Science (80-.). 249 (1990) 1431–1433. doi:10.1126/science.1698311.
[35] H.R. Michie, K.R. Manogue, D.R. Spriggs, A. Revhaug, S. O'Dwyer, C.A. Dinarello, A. Cerami, S.M. Wolff, D.W. Wilmore, Detection of Circulating Tumor Necrosis Factor after Endotoxin Administration, N. Engl. J. Med. 318 (1988) 1481–1486. doi:10.1056/NEJM198806093182301.
[36] L. Feng, A. Sivanesan, Z. Lyu, A. Offenhäusser, D. Mayer, Electrochemical current rectification-a novel signal amplification strategy for highly sensitive and selective aptamer-based biosensor, Biosens. Bioelectron. 66 (2015) 62–68. doi:10.1016/j.bios.2014.10.057.
[37] C.R.H. Raetz, Biochemistry of endotoxins, Annu. Rev. Biochem. 59 (1990) 129–170. doi:10.1146/annurev.bi.59.070190.001021.
[38] R.J. Ulevitch, P.S. Tobias, Receptor-Dependent Mechanisms of Cell Stimulation by Bacterial Endotoxin, Annu. Rev. Immunol. 13 (1995) 437–457. doi:10.1146/annurev.iy.13.040195.002253.
[39] N.C. Santos, A.C. Silva, M.A.R.B. Castanho, J. Martins-Silva, C. Saldanha, Evaluation of Lipopolysaccharide aggregation by light scattering spectroscopy, ChemBioChem. 4 (2003) 96–100. doi:10.1002/cbic.200390020.
[40] F. Cochet, F. Peri, The role of carbohydrates in the lipopolysaccharide (LPS)/toll-like receptor 4 (TLR4) Signalling, Int. J. Mol. Sci. 18 (2017). doi:10.3390/ijms18112318.
[41] K.H. Jacobson, I.L. Gunsolus, T.R. Kuech, J.M. Troiano, E.S. Melby, S.E. Lohse, D. Hu, W.B. Chrisler, C.J. Murphy, G. Orr, F.M. Geiger, C.L. Haynes, J.A. Pedersen, Lipopolysaccharide Density and Structure Govern the Extent and Distance of Nanoparticle Interaction with Actual and Model Bacterial Outer Membranes, Environ. Sci. Technol. 49 (2015) 10642–10650. doi:10.1021/acs.est.5b01841.
[42] E.T. Rietschel, T. Kirikae, F.U. Schade, U. Mamat, G. Schmidt, H. Loppnow, A.J. Ulmer, U. Zähringer, U. Seydel, F. Di Padova, M. Schreier, H. Brade, Bacterial endotoxin: molecular relationships of structure to activity and function, FASEB J. 8 (1994) 217–225. doi:10.1096/fasebj.8.2.8119492.
[43] E. Ribi, R.L. Anacker, R. Brown, W.T. Haskins, B. Malmgren, K.C. Milner, J.A. Rudbach, Reaction of endotoxin and surfactants. I. Physical and biological properties of endotoxin treated with sodium deoxycholate., J. Bacteriol. 92 (1966) 1493–509. doi:10.1128/jb.92.5.1493-1509.1966.
[44] J. Reich, F.A. Weyer, H. Tamura, I. Nagaoka, H. Motschmann, Low endotoxin recovery—Masking of naturally occuring endotoxin, Int. J. Mol. Sci. 20 (2019) 1–15. doi:10.3390/ijms20040838.
[45] R. Medzhitov, Recognition of microorganisms and activation of the immune response, Nature. 449 (2007) 819–826. doi:10.1038/nature06246.
[46] C.A. Janeway, R. Medzhitov, Innate immune recognition, Annu. Rev. Immunol. 20 (2002) 197–216. doi:10.1146/annurev.immunol.20.083001.084359.
[47] R. Medzhitov, Toll-like receptors and innate immunity, J. Bacteriol. Virol. 1 (2001) 135–145. doi:10.1038/35100529.
[48] J. Banchereau, R.M. Steinman, Dendritic cells and the control of immunity., Nature. 392 (1998) 245–52. doi:10.1038/32588.

[49] S. Gordon, Pattern recognition receptors: Doubling up for the innate immune response, Cell. 111 (2002) 927–930. doi:10.1016/S0092-8674(02)01201-1.
[50] A.S. McWilliam, S. Napoli, A.M. Marsh, F.L. Pemper, D.J. Nelson, C.L. Pimm, P.A. Stumbles, T.N.C. Wells, P.G. Holt, Dendritic cells are recruited into the airway epithelium during the inflammatory response to a broad spectrum of stimuli, J. Exp. Med. 184 (1996) 2429–2432. doi:10.1084/jem.184.6.2429.
[51] T. Liu, L. Zhang, D. Joo, S.-C. Sun, NF-κB signaling in inflammation, Signal Transduct. Target. Ther. 2 (2017) 17023. doi:10.1038/sigtrans.2017.23.
[52] R. Medzhitov, P. Preston-Hurlburt, C.A. Janeway, A human homologue of the Drosophila toll protein signals activation of adaptive immunity, Nature. 388 (1997) 394–397. doi:10.1038/41131.
[53] K.A. Zarember, P.J. Godowski, Tissue Expression of Human Toll-Like Receptors and Differential Regulation of Toll-Like Receptor mRNAs in Leukocytes in Response to Microbes, Their Products, and Cytokines, J. Immunol. 168 (2002) 554–561. doi:10.4049/jimmunol.168.2.554.
[54] P.M. Chaudhary, C. Ferguson, V. Nguyen, O. Nguyen, H.F. Massa, M. Eby, A. Jasmin, B.J. Trask, L. Hood, P.S. Nelson, Cloning and characterization of two toll/interleukin-1 receptor-like genes TIL3 and TIL4: Evidence for a multi-gene receptor family in humans, Blood. 91 (1998) 4020–4027. doi:10.1182/blood.v91.11.4020.411a44_4020_4027.
[55] P. Prohinar, F. Re, R. Widstrom, D. Zhang, A. Teghanemt, J.P. Weiss, T.L. Gioannini, Specific High Affinity Interactions of Monomeric Endotoxin·Protein Complexes with Toll-like Receptor 4 Ectodomain, J. Biol. Chem. 282 (2007) 1010–1017. doi:10.1074/jbc.M609400200.
[56] H. Schwarz, J. Gornicec, T. Neuper, M.A. Parigiani, M. Wallner, A. Duschl, J. Horejs-Hoeck, Biological Activity of Masked Endotoxin, Sci. Rep. 7 (2017) 44750. doi:10.1038/srep44750.
[57] J. Reich, P. Lang, H. Grallert, H. Motschmann, Masking of endotoxin in surfactant samples: Effects on Limulus-based detection systems, Biologicals. 44 (2016) 417–422. doi:10.1016/j.biologicals.2016.04.012.
[58] C.L. Krüger, M.-T. Zeuner, G.S. Cottrell, D. Widera, M. Heilemann, Quantitative single-molecule imaging of TLR4 reveals ligand-specific receptor dimerization., Sci. Signal. 10 (2017) eaan1308. doi:10.1126/scisignal.aan1308.
[59] A. Ulman, Formation and Structure of Self-Assembled Monolayers, Chem. Rev. 96 (1996) 1533–1554. doi:10.1021/cr9502357.
[60] A.H. Pakiari, Z. Jamshidi, Nature and Strength of M−S Bonds (M = Au, Ag, and Cu) in Binary Alloy Gold Clusters, J. Phys. Chem. A. 114 (2010) 9212–9221. doi:10.1021/jp100423b.
[61] J.C. Love, L.A. Estroff, J.K. Kriebel, R.G. Nuzzo, G.M. Whitesides, Self-Assembled Monolayers of Thiolates on Metals as a Form of Nanotechnology, Chem. Rev. 105 (2005) 1103–1170. doi:10.1021/cr0300789.
[62] H.A. Abdulbari, E.A.M. Basheer, Electrochemical Biosensors: Electrode Development, Materials, Design, and Fabrication, ChemBioEng Rev. 4 (2017) 92–105. doi:10.1002/cben.201600009.
[63] R.G. Nuzzo, B.R. Zegarski, L.H. DuBois, Fundamental Studies of the Chemisorption of

Organosulfur Compounds on Au(111). Implications for Molecular Self-Assembly on Gold Surfaces, J. Am. Chem. Soc. 109 (1987) 733–740. doi:10.1021/ja00237a017.
[64] A. Ulman, Formation and structure of self-assembled monolayers, Chem. Rev. 96 (1996) 1533–1554. doi:10.1021/cr9502357.
[65] F. Schreiber, Structure and growth of self-assembling monolayers, Prog. Surf. Sci. 65 (2000) 151–257. doi:10.1016/S0079-6816(00)00024-1.
[66] C. Vericat, M.E. Vela, R.C. Salvarezza, Self-assembled monolayers of alkanethiols on Au(111): surface structures, defects and dynamics, Phys. Chem. Chem. Phys. 7 (2005) 3258. doi:10.1039/b505903h.
[67] Q. Guo, F. Li, Self-assembled alkanethiol monolayers on gold surfaces: Resolving the complex structure at the interface by STM, Phys. Chem. Chem. Phys. 16 (2014) 19074–19090. doi:10.1039/c4cp00596a.
[68] R. Yamada, H. Wano, K. Uosaki, Effect of Temperature on Structure of the Self-Assembled Monolayer of Decanethiol on Au(111) Surface, Langmuir. 16 (2000) 5523–5525. doi:10.1021/la991394e.
[69] A. Badia, L. Cuccia, L. Demers, F. Morin, R.B. Lennox, Structure and Dynamics in Alkanethiolate Monolayers Self-Assembled on Gold Nanoparticles: A DSC, FT-IR, and Deuterium NMR Study, J. Am. Chem. Soc. 119 (1997) 2682–2692. doi:10.1021/ja963571t.
[70] F. Bensebaa, T.H. Ellis, Thermal Treatment of n -Alkanethiolate Monolayers on Gold , As Observed by Infrared Spectroscopy, 7463 (1998) 2361–2367. doi:10.1021/la9711589.
[71] R.G. Nuzzo, E.M. Korenic, L.H. Dubois, Studies of the temperature-dependent phase behavior of long chain n -alkyl thiol monolayers on gold, J. Chem. Phys. 93 (1990) 767–773. doi:10.1063/1.459528.
[72] N. Prathima, M. Harini, N. Rai, R.H. Chandrashekara, K.G. Ayappa, S. Sampath, S.K. Biswas, Thermal Study of Accumulation of Conformational Disorders in the Self-Assembled Monolayers of C 8 and C 18 Alkanethiols on the Au(111) Surface, Langmuir. 21 (2005) 2364–2374. doi:10.1021/la048654z.
[73] J. Hautman, M.L. Klein, Simulation of a monolayer of alkyl thiol chains, J. Chem. Phys. 91 (1989) 4994–5001. doi:10.1063/1.457621.
[74] P. Fenter, P. Eisenberger, K.S. Liang, Chain-length dependence of the structures and phases of CH 3 (CH 2) n − 1 SH self-assembled on Au(111), Phys. Rev. Lett. 70 (1993) 2447–2450. doi:10.1103/PhysRevLett.70.2447.
[75] E. Delamarche, B. Michel, H.A. Biebuyck, C. Gerber, Golden interfaces: The Surface of Self-Assembled Monolayers, Adv. Mater. 8 (1996) 719–729. doi:10.1002/adma.19960080903.
[76] E. Ostuni, B.A. Grzybowski, M. Mrksich, C.S. Roberts, G.M. Whitesides, Adsorption of Proteins to Hydrophobic Sites on Mixed Self-Assembled Monolayers †, Langmuir. 19 (2003) 1861–1872. doi:10.1021/la020649c.
[77] E. Ostuni, R.G. Chapman, R.E. Holmlin, S. Takayama, G.M. Whitesides, A Survey of Structure−Property Relationships of Surfaces that Resist the Adsorption of Protein, Langmuir. 17 (2001) 5605–5620. doi:10.1021/la010384m.
[78] K. Prime, G. Whitesides, Self-assembled organic monolayers: model systems for studying adsorption of proteins at surfaces, Science (80-.). 252 (1991) 1164–1167.

doi:10.1126/science.252.5009.1164.
[79] M. Mrksich, G.B. Sigal, G.M. Whitesides, Surface Plasmon Resonance Permits in Situ Measurement of Protein Adsorption on Self-Assembled Monolayers of Alkanethiolates on Gold, Langmuir. 11 (1995) 4383–4385. doi:10.1021/la00011a034.
[80] P. Harder, M. Grunze, R. Dahint, G.M. Whitesides, P.E. Laibinis, Molecular Conformation in Oligo(ethylene glycol)-Terminated Self-Assembled Monolayers on Gold and Silver Surfaces Determines Their Ability To Resist Protein Adsorption, J. Phys. Chem. B. 102 (1998) 426–436. doi:10.1021/jp972635z.
[81] E. Kang, J.W. Park, S.J. McClellan, J.M. Kim, D.P. Holland, G.U. Lee, E.I. Franses, K. Park, D.H. Thompson, Specific adsorption of histidine-tagged proteins on silica surfaces modified with Ni2+/NTA-derivatized poly(ethylene glycol), Langmuir. 23 (2007) 6281–6288. doi:10.1021/la063719e.
[82] R.M. Nyquist, A.S. Eberhardt, L.A. Silks, Z. Li, X. Yang, B.I. Swanson, Characterization of Self-Assembled Monolayers for Biosensor Applications, Langmuir. 16 (2000) 1793–1800. doi:10.1021/la990018r.
[83] C.A. Wolfe, D.S. Hage, Studies on the rate and control of antibody oxidation by periodate., Anal. Biochem. 231 (1995) 123–30. doi:10.1006/abio.1995.1511.
[84] B. Lu, M.R. Smyth, R. O'Kennedy, Oriented immobilization of antibodies and its applications in immunoassays and immunosensors., Analyst. 121 (1996) 29R-32R. doi:10.1039/an996210029r.
[85] F.-J. Schmitt, L. Häussling, H. Ringsdorf, W. Knoll, Surface plasmon studies of specific recognition reactions at self-assembled monolayers on gold, Thin Solid Films. 210–211 (1992) 815–817. doi:10.1016/0040-6090(92)90412-5.
[86] L. Haeussling, H. Ringsdorf, F.J. Schmitt, W. Knoll, Biotin-functionalized self-assembled monolayers on gold: surface plasmon optical studies of specific recognition reactions, Langmuir. 7 (1991) 1837–1840. doi:10.1021/la00057a001.
[87] R.C. Ebersole, J.A. Miller, J.R. Moran, M.D. Ward, Spontaneously formed functionally active avidin monolayers on metal surfaces: a strategy for immobilizing biological reagents and design of piezoelectric biosensors, J. Am. Chem. Soc. 112 (1990) 3239–3241. doi:10.1021/ja00164a070.
[88] T. Hoshi, J. Anzai, T. Osa, Electrochemical deposition of avidin on the surface of a platinum electrode for enzyme sensor applications, Anal. Chim. Acta. 289 (1994) 321–327. doi:10.1016/0003-2670(94)90008-X.
[89] S. Löfås, B. Johnsson, Å. Edström, A. Hansson, G. Lindquist, R.-M.M. Hillgren, L. Stigh, Methods for site controlled coupling to carboxymethyldextran surfaces in surface plasmon resonance sensors, Biosens. Bioelectron. 10 (1995) 813–822. doi:10.1016/0956-5663(95)99220-F.
[90] T. Wink, S.J. van Zuilen, A. Bult, W.P. van Bennekom, Self-assembled Monolayers for Biosensors, Analyst. 122 (1997) 43R-50R. doi:10.1039/a606964i.
[91] M. Collinson, E.F. Bowden, M.J. Tarlov, Voltammetry of covalently immobilized cytochrome c on self-assembled monolayer electrodes, Langmuir. 8 (1992) 1247–1250. doi:10.1021/la00041a004.
[92] K.M. Millan, S.R. Mikkelsen, Sequence-selective biosensor for DNA based on electroactive hybridization indicators, Anal. Chem. 65 (1993) 2317–2323.

doi:10.1021/ac00065a025.
[93] S. Löfås, B. Johnsson, A novel hydrogel matrix on gold surfaces in surface plasmon resonance sensors for fast and efficient covalent immobilization of ligands, J. Chem. Soc., Chem. Commun. (1990) 1526–1528. doi:10.1039/C39900001526.
[94] G.B. Sigal, C. Bamdad, A. Barberis, J. Strominger, G.M. Whitesides, A Self-Assembled Monolayer for the Binding and Study of Histidine-Tagged Proteins by Surface Plasmon Resonance, Anal. Chem. 68 (1996) 490–497. doi:10.1021/ac9504023.
[95] I.-H. Cho, E.-H. Paek, H. Lee, J.Y. Kang, T.S. Kim, S.-H. Paek, Site-directed biotinylation of antibodies for controlled immobilization on solid surfaces, Anal. Biochem. 365 (2007) 14–23. doi:10.1016/j.ab.2007.02.028.
[96] S. Löfås, B. Johnsson, K. Tegendal, I. Rönnberg, Dextran modified gold surfaces for surface plasmon resonance sensors: immunoreactivity of immobilized antibodies and antibody-surface interaction studies, Colloids Surfaces B Biointerfaces. 1 (1993) 83–89. doi:10.1016/0927-7765(93)80038-Z.
[97] A. Eivazihollagh, H. Edlund, M. Norgren, J. Bäckström, Metal-Chelate Complexes in Alkaline Solution : On Recovery Techniques and Cellulose-based Hybrid Material Synthesis, 2018. http://urn.kb.se/resolve?urn=urn:nbn:se:miun:diva-33975.
[98] C.W.P. donald voet, Judith G. Voet, Fundamentals of Biochemistry: Life at the Molecular Level, John Wiley & Sons, Inc., 2013.
[99] E. Hochuli, H. Döbeli, A. Schacher, New metal chelate adsorbent selective for proteins and peptides containing neighbouring histidine residues, J. Chromatogr. A. 411 (1987) 177–184. doi:10.1016/S0021-9673(00)93969-4.
[100] R. Gentz, C.H. Chen, C.A. Rosen, Bioassay for trans-activation using purified human immunodeficiency virus tat-encoded protein: trans-activation requires mRNA synthesis., Proc. Natl. Acad. Sci. 86 (1989) 821–824. doi:10.1073/pnas.86.3.821.
[101] K. Amini, N.W.C. Chan, H.-B.H.-B. Kraatz, Toll-like receptor 3 modified Au electrodes: An investigation into the interaction of TLR3 immobilized on Au surfaces with poly(I:C), Anal. Methods. 6 (2014) 3322–3328. doi:10.1039/c4ay00369a.
[102] A.L. Blasius, B. Beutler, Intracellular Toll-like Receptors, Immunity. 32 (2010) 305–315. doi:10.1016/j.immuni.2010.03.012.
[103] L. Alexopoulou, A.C. Holt, R. Medzhitov, R.A. Flavell, Recognition of double-stranded RNA and activation of NF-κB by Toll-like receptor 3, Nature. 413 (2001) 732–738. doi:10.1038/35099560.
[104] Z. She, K. Topping, M.H. Shamsi, N. Wang, N.W.C. Chan, H.B. Kraatz, Investigation of the utility of complementary electrochemical detection techniques to examine the in vitro affinity of bacterial flagellins for a toll-like receptor 5 biosensor, Anal. Chem. 87 (2015) 4218–4224. doi:10.1021/ac5042439.
[105] D. Lin, K.D. Harris, N.W.C. Chan, A.B. Jemere, Nanostructured indium tin oxide electrodes immobilized with toll-like receptor proteins for label-free electrochemical detection of pathogen markers, Sensors Actuators, B Chem. 257 (2018) 324–330. doi:10.1016/j.snb.2017.10.140.
[106] Samuel Baron, ed., Medical Microbiology, 4th ed., Galveston, Texas, 1996.
[107] S. Akira, K. Takeda, T. Kaisho, Toll-like receptors: critical proteins linking innate and acquired immunity, Nat. Immunol. 2 (2001) 675–680. doi:10.1038/90609.

[108] T. Zhao, W. Zhou, H.-B. Kraatz, K. Topping, S. Ahmadi, A. Kamal, T. Ma, Z. She, Detection of the Lipopeptide Pam3CSK4 Using a Hybridized Toll-like Receptor Electrochemical Sensor, Anal. Chem. 89 (2017) 4882–4888. doi:10.1021/acs.analchem.6b04799.
[109] J. McLeod, C. Park, A. Cunningham, L. O'Donnell, R.S. Brown, F. Kelly, Z. She, Developing a toll-like receptor biosensor for Gram-positive bacterial detection and its storage strategies, Analyst. 145 (2020) 6024–6031. doi:10.1039/D0AN01050B.
[110] T.Y. Yeo, J.S. Choi, B.K. Lee, B.S. Kim, H.I. Yoon, H.Y. Lee, Y.W. Cho, Electrochemical endotoxin sensors based on TLR4/MD-2 complexes immobilized on gold electrodes, Biosens. Bioelectron. 28 (2011) 139–145. doi:10.1016/j.bios.2011.07.010.
[111] P. Guardado-Calvo, Python script to calculate and draw a minimal bounding box for a given protein, 2016. doi:10.13140/RG.2.2.17806.77127.
[112] H.M. Kim, B.S. Park, J.-I. Kim, S.E. Kim, J. Lee, S.C. Oh, P. Enkhbayar, N. Matsushima, H. Lee, O.J. Yoo, J.-O. Lee, Crystal Structure of the TLR4-MD-2 Complex with Bound Endotoxin Antagonist Eritoran, Cell. 130 (2007) 906–917. doi:10.1016/j.cell.2007.08.002.
[113] K. Amini, I.I. Ebralidze, N.W.C. Chan, H.B. Kraatz, Characterization of TLR4/MD-2-modified Au sensor surfaces towards the detection of molecular signatures of bacteria, Anal. Methods. 8 (2016) 7623–7631. doi:10.1039/c6ay01978a.
[114] A.L. Eckermann, D.J. Feld, J.A. Shaw, T.J. Meade, Electrochemistry of redox-active self-assembled monolayers, Coord. Chem. Rev. 254 (2010) 1769–1802. doi:10.1016/j.ccr.2009.12.023.
[115] N. Nerngchamnong, D. Thompson, L. Cao, L. Yuan, L. Jiang, M. Roemer, C.A. Nijhuis, Nonideal Electrochemical Behavior of Ferrocenyl-Alkanethiolate SAMs Maps the Microenvironment of the Redox Unit, J. Phys. Chem. C. 119 (2015) 21978–21991. doi:10.1021/acs.jpcc.5b05137.
[116] C.D. Bain, J. Evall, G.M. Whitesides, Formation of monolayers by the coadsorption of thiols on gold: variation in the head group, tail group, and solvent, J. Am. Chem. Soc. 111 (1989) 7155–7164. doi:10.1021/ja00200a039.
[117] J.P. Folkers, P.E. Laibinis, G.M. Whitesides, J. Deutch, Phase behavior of two-component self-assembled monolayers of alkanethiolates on gold, J. Phys. Chem. 98 (1994) 563–571. doi:10.1021/j100053a035.
[118] C.D. Bain, G.M. Whitesides, Formation of monolayers by the coadsorption of thiols on gold: variation in the length of the alkyl chain, J. Am. Chem. Soc. 111 (1989) 7164–7175. doi:10.1021/ja00200a040.
[119] C.D. Bain, G.M. Whitesides, Formation of two-component surfaces by the spontaneous assembly of monolayers on gold from solutions containing mixtures of organic thiols, J. Am. Chem. Soc. 110 (1988) 6560–6561. doi:10.1021/ja00227a044.
[120] C.D. Bain, G.M. Whitesides, Correlations between wettability and structure in monolayers of alkanethiols adsorbed on gold, J. Am. Chem. Soc. 110 (1988) 3665–3666. doi:10.1021/ja00219a055.
[121] L.Y.S. Lee, T.C. Sutherland, S. Rucareanu, R.B. Lennox, Ferrocenylalkylthiolates as a probe of heterogeneity in binary self-assembled monolayers on gold, Langmuir. 22 (2006) 4438–4444. doi:10.1021/la053317r.
[122] L.Y.S. Lee, R.B. Lennox, Ferrocenylalkylthiolate labeling of defects in alkylthiol self-

assembled monolayers on gold, Phys. Chem. Chem. Phys. 9 (2007) 1013–1020. doi:10.1039/b613598f.
[123] L.Y.S. Lee, R.B. Lennox, Electrochemical desorption of n-alkylthiol SAMs on polycrystalline gold: Studies using a ferrocenylalkylthiol probe, Langmuir. 23 (2007) 292–296. doi:10.1021/la061684c.
[124] K. Weber, L. Hockett, S. Creager, Long-Range Electronic Coupling between Ferrocene and Gold in Alkanethiolate-based Monolayers on Electrodes, J. Phys. Chem. B. 101 (1997) 8286–8291. doi:10.1021/jp9717103.
[125] C.E.D. Chidsey, Free Energy and Temperature Dependence of Electron Transfer at the Metal-Electrolyte Interface, Science (80-.). 251 (1991) 919–922. doi:10.1126/science.251.4996.919.
[126] L. Tender, M.T. Carter, R.W. Murray, Cyclic Voltammetric Analysis of Ferrocene Alkanethiol Monolayer Electrode Kinetics Based on Marcus Theory, Anal. Chem. 66 (1994) 3173–3181. doi:10.1021/ac00091a028.
[127] J.N. Richardson, S.R. Peck, L.S. Curtin, L.M. Tender, R.H. Terrill, M.T. Carter, R.W. Murray, G.K. Rowe, S.E. Creager, Electron-Transfer Kinetics of Self-Assembled Ferrocene Octanethiol Monolayers on Gold and Silver Electrodes from 115 to 170 K, J. Phys. Chem. 99 (1995) 766–772. doi:10.1021/j100002a046.
[128] M.T. Carter, G.K. Rowe, J.N. Richardson, L.M. Tender, R.H. Terrill, R.W. Murray, Distance Dependence of the Low-Temperature Electron Transfer Kinetics of (Ferrocenylcarboxy)-Terminated Alkanethiol Monolayers, J. Am. Chem. Soc. 117 (1995) 2896–2899. doi:10.1021/ja00115a022.
[129] J.N. Richardson, G.K. Rowe, M.T. Carter, L.M. Tender, L.S. Curtin, S.R. Peck, R.W. Murray, Electron transfer kinetics of self-assembled ferrocene (C12)Alkanethiol monolayers on gold electrodes from 125 K to 175 K, Electrochim. Acta. 40 (1995) 1331–1338. doi:10.1016/0013-4686(95)00068-P.
[130] C.E.D. Chidsey, C.R. Bertozzi, T.M. Putvinski, A.M. Mujsce, Coadsorption of ferrocene-terminated and unsubstituted alkanethiols on gold: Electroactive self-assembled monolayers, J. Am. Chem. Soc. 112 (1990) 4301–4306. doi:10.1021/ja00167a028.
[131] L.A. Hockett, S.E. Creager, Redox Kinetics for Ferrocene Groups Immobilized in Impermeable and Permeable Self-Assembled Monolayers, Langmuir. 11 (1995) 2318–2321. doi:10.1021/la00006a077.
[132] C.A. Nijhuis, W.F. Reus, J.R. Barber, M.D. Dickey, G.M. Whitesides, Charge Transport and Rectification in Arrays of SAM-Based Tunneling Junctions, Nano Lett. 10 (2010) 3611–3619. doi:10.1021/nl101918m.
[133] C.A. Nijhuis, W.F. Reus, G.M. Whitesides, Mechanism of Rectification in Tunneling Junctions Based on Molecules with Asymmetric Potential Drops, J. Am. Chem. Soc. 132 (2010) 18386–18401. doi:10.1021/ja108311j.
[134] J.J. Sumner, K.S. Weber, L. a Hockett, S.E. Creager, Long-range heterogeneous electron transfer between ferrocene and gold mediated by n-alkane and N-alkyl-carboxamide bridges, J. Phys. Chem. B. 104 (2000) 7449–7454. doi:10.1021/jp000992v.
[135] S.E. Creager, G.K. Rowe, Solvent and double-layer effects on redox reactions in self-assembled monolayers of ferrocenyl-alkanethiolates on gold, J. Electroanal. Chem. 420 (1997) 291–299. doi:10.1016/S0022-0728(96)04785-7.

[136] G.K. Rowe, S.E. Creager, Interfacial solvation and double-layer effects on redox reactions in organized assemblies, J. Phys. Chem. 98 (1994) 5500–5507. doi:10.1021/j100072a017.
[137] S.E. Creager, G.K. Rowe, Redox properties of ferrocenylalkane thiols coadsorbed with linear n-alkanethiols on polycrystalline bulk gold electrodes, Anal. Chim. Acta. 246 (1991) 233–239. doi:10.1016/S0003-2670(00)80680-7.
[138] J.J. Sumner, S.E. Creager, Redox kinetics in monolayers on electrodes: Electron transfer is sluggish for ferrocene groups buried within the monolayer interior, J. Phys. Chem. B. 105 (2001) 8739–8745. doi:10.1021/jp011229j.
[139] K.S. Alleman, K. Weber, S.E. Creager, Electrochemical Rectification at a Monolayer-Modified Electrode, J. Phys. Chem. 100 (1996) 17050–17058. doi:10.1021/jp962193b.
[140] R.M. Mayall, V.I. Birss, S.E. Creager, Digital Simulation and Experimental Validation of Redox Mediation at an Electroactive Monolayer-Coated Electrode, J. Electrochem. Soc. 167 (2020) 046512. doi:10.1149/1945-7111/ab77a3.
[141] E. Boubour, R.B. Lennox, Insulating Properties of Self-Assembled Monolayers Monitored by Impedance Spectroscopy, (2000) 4222–4228. doi:10.1021/la991328c.
[142] D.D. Agonafer, E. Chainani, M.E. Oruc, K.S. Lee, M.A. Shannon, Study of insulating properties of alkanethiol self-assembled monolayers formed under prolonged incubation using electrochemical impedance spectroscopy, J. Nanotechnol. Eng. Med. 3 (2012) 1–8. doi:10.1115/1.4007698.
[143] R.M. Mayall, Electrochemical Biosensors Based on Thiol and N-Heterocyclic Carbene Self-Assembled Monolayers, (2019). doi:10.1017/CBO9781107415324.004.
[144] F. Lisdat, D. Schäfer, The use of electrochemical impedance spectroscopy for biosensing, (2008) 1555–1567. doi:10.1007/s00216-008-1970-7.
[145] Intro to electrochemical impedance - Petr Vanysek.pdf, (n.d.).
[146] K.A. Groat, S.E. Creager, Self-assembled monolayers in organic solvents: electrochemistry at alkanethiolate-coated gold in propylene carbonate, Langmuir. 9 (1993) 3668–3675. doi:10.1021/la00036a051.
[147] M. Lukaszewski, M. Soszko, A. Czerwiński, Electrochemical methods of real surface area determination of noble metal electrodes - an overview, Int. J. Electrochem. Sci. 11 (2016) 4442–4469. doi:10.20964/2016.06.71.
[148] R.C.D. G H Jeffrey, J Basset, J Mendham, Vogel's textbook of quantitative analysis, 5th ed., London, 1989.
[149] C onfiguration M anual, (n.d.).
[150] K. Amini, I.I. Ebralidze, N.W.C. Chan, H.B. Kraatz, Characterization of TLR4/MD-2-modified Au sensor surfaces towards the detection of molecular signatures of bacteria, Anal. Methods. 8 (2016) 7623–7631. doi:10.1039/c6ay01978a.
[151] E. Boubour, R.B. Lennox, Potential-induced defects in n-alkanethiol self-assembled monolayers monitored by impedance spectroscopy, J. Phys. Chem. B. 104 (2000) 9004–9010. doi:10.1021/jp000151o.
[152] H. Sahalov, B. O'Brien, K.J. Stebe, K. Hristova, P.C. Searson, Influence of applied potential on the impedance of alkanethiol SAMs, Langmuir. 23 (2007) 9681–9685. doi:10.1021/la701398u.
[153] M.M. Walczak, D.D. Popenoe, R.S. Deinhammer, B.D. Lamp, C. Chung, M.D. Porter, Reductive Desorption of Alkanethiolate Monolayers at Gold: A Measure of Surface

Coverage, Langmuir. 7 (1991) 2687–2693. doi:10.1021/la00059a048.
[154] M.M. Walczak, C.A. Alves, B.D. Lamp, M.D. Porter, Electrochemical and X-ray photoelectron spectroscopic evidence for differences in the binding sites of alkanethiolate monolayers chemisorbed at gold, J. Electroanal. Chem. 396 (1995) 103–114. doi:10.1016/0022-0728(95)04056-T.
[155] L. Jiang, L. Yuan, L. Cao, C.A. Nijhuis, Controlling leakage currents: The role of the binding group and purity of the precursors for self-assembled monolayers in the performance of molecular diodes, J. Am. Chem. Soc. 136 (2014) 1982–1991. doi:10.1021/ja411116n.
[156] J. Huang, J.C. Hemminger, Photooxidation of thiols in self-assembled monolayers on gold, J. Am. Chem. Soc. 115 (1993) 3342–3343. doi:10.1021/ja00061a048.
[157] C. Vericat, M.E. Vela, G. Corthey, E. Pensa, E. Cortés, M.H. Fonticelli, F. Ibañez, G.E. Benitez, P. Carro, R.C. Salvarezza, Self-assembled monolayers of thiolates on metals: A review article on sulfur-metal chemistry and surface structures, RSC Adv. 4 (2014) 27730–27754. doi:10.1039/c4ra04659e.
[158] R.G. Nuzzo, F.A. Fusco, D.L. Allara, Spontaneously Organized Molecular Assemblies. 3. Preparation and Properties of Solution Adsorbed Monolayers of Organic Disulfides on Gold Surfaces, J. Am. Chem. Soc. 109 (1987) 2358–2368. doi:10.1021/ja00242a020.
[159] R.G. Nuzzo, D.L. Allara, Adsorption of Bifunctional Organic Disulfides on Gold Surfaces, J. Am. Chem. Soc. 105 (1983) 4481–4483. doi:10.1021/ja00351a063.
[160] U.T. Rüegg, J. Rudinger, Reductive Cleavage of Cystine Disulfides with Tributylphosphine, Methods Enzymol. 47 (1977) 111–116. doi:10.1016/0076-6879(77)47012-5.
[161] J.R. Winther, C. Thorpe, Quantification of thiols and disulfides, Biochim. Biophys. Acta - Gen. Subj. 1840 (2014) 838–846. doi:10.1016/j.bbagen.2013.03.031.
[162] Y. Xu, F. Li, Z. Yu, G. Zhang, Y. Song, H. Yan, A dual-probe surface-co-immobilization-based electrochemical sensor for highly sensitive and tunable specific detection of a designated DNA, Sensors Actuators, B Chem. 239 (2017) 786–794. doi:10.1016/j.snb.2016.08.078.
[163] J.P. Folkers, P.E. Laibinis, G.M. Whitesides, J. Deutch, Phase behavior of two-component self-assembled monolayers of alkanethiolates on gold, J. Phys. Chem. 98 (1994) 563–571. doi:10.1021/j100053a035.
[164] C.D. BAIN, G.M. WHITESIDES, Molecular-Level Control over Surface Order in Self-Assembled Monolayer Films of Thiols on Gold, Science (80-.). 240 (1988) 62–63. doi:10.1126/science.240.4848.62.
[165] R. Breuer, M. Schmittel, Redox-stable SAMs in water (pH 0-12) from 1,1′-biferrocenylene- terminated thiols on gold, Organometallics. 31 (2012) 6642–6651. doi:10.1021/om300718k.
[166] H. Ju, D. Leech, Effect of electrolytes on the electrochemical behaviour of 11-(ferrocenylcarbonyloxy)undecanethiol SAMs on gold disk electrodes, Phys. Chem. Chem. Phys. 1 (1999) 1549–1554. doi:10.1039/a809754b.
[167] R. Prins, A.R. Korswagen, A.G.T.G. Kortbeek, Decomposition of the ferricenium cation by nucleophilic reagents, J. Organomet. Chem. 39 (1972) 335–344. doi:10.1016/S0022-328X(00)80459-3.

[168] L.N. Nekrasov, L.P. Yur'eva, Electrochemical approach to direct homogeneous chemical cyanation of ferricenium salts: The complexing of system components, Russ. J. Electrochem. 36 (2000) 299–307. doi:10.1007/BF02827974.
[169] J. Holeček, K. Handlíř, J. Klikorka, N.D. Bang, Decomposition of ferricenium cation in alkaline medium, Collect. Czechoslov. Chem. Commun. 44 (1979) 1379–1387. doi:10.1135/cccc19791379.
[170] L.L. Norman, A. Badia, Electrochemical Surface Plasmon Resonance Investigation of Dodecyl Sulfate Adsorption to Electroactive Self-Assembled Monolayers via Ion-Pairing Interactions, Langmuir. 23 (2007) 10198–10208. doi:10.1021/la7006028.
[171] G.K. Rowe, S.E. Creager, Redox and Ion-Pairing Thermodynamics in Self-Assembled Monolayers, Langmuir. 7 (1991) 2307–2312. doi:10.1021/la00058a055.
[172] K. Uosaki, Y. Sato, H. Kita, Electrochemical characteristics of a gold electrode modified with a self-assembled monolayer of ferrocenylalkanethiols, Langmuir. 7 (1991) 1510–1514. doi:10.1021/la00055a038.
[173] Y. Yokota, T. Yamada, M. Kawai, Ion-Pair Formation between Ferrocene-Terminated Self-Assembled Monolayers and Counteranions Studied by Force Measurements, J. Phys. Chem. C. 115 (2011) 6775–6781. doi:10.1021/jp2001404.
[174] K. Shimazu, I. Yagi, Y. Sato, K. Uosaki, Electrochemical quartz crystal microbalance studies of self-assembled monolayers of 11-ferrocenyl-1-undecanethiol: Structure-dependent ion-pairing and solvent uptake, J. Electroanal. Chem. 372 (1994) 117–124. doi:10.1016/0022-0728(94)03296-3.
[175] S. Ye, T. Haba, Y. Sato, K. Shimazu, K. Uosaki, Coverage dependent behavior of redox reaction induced structure change and mass transport at an 11-ferrocenyl-1-undecanethiol self-assembled monolayer on a gold electrode studied by an in situ IRRAS–EQCM combined system, Phys. Chem. Chem. Phys. 1 (1999) 3653–3659. doi:10.1039/a902952d.
[176] L.L. Norman, A. Badia, Microcantilevers Modified with Ferrocene-Terminated Self-Assembled Monolayers: Effect of Molecular Structure and Electrolyte Anion on the Redox-Induced Surface Stress, J. Phys. Chem. C. 115 (2011) 1985–1995. doi:10.1021/jp108284w.
[177] G. Valincius, G. Niaura, B. Kazakevičiene, Z. Talaikyte, M. Kažemekaite, E. Butkus, V. Razumas, Anion effect on mediated electron transfer through ferrocene-terminated self-assembled monolayers, Langmuir. 20 (2004) 6631–6638. doi:10.1021/la0364800.
[178] F. Quist, V. Tabard-Cossa, A. Badia, Nanomechanical Cantilever Motion Generated by a Surface-Confined Redox Reaction, J. Phys. Chem. B. 107 (2003) 10691–10695. doi:10.1021/jp0355915.
[179] N.L. Abbott, G.M. Whitesides, Potential-Dependent Wetting of Aqueous Solutions on Self-Assembled Monolayers Formed from 15-(Ferrocenylcarbonyl)pentadecanethiol on Gold, Langmuir. 10 (1994) 1493–1497. doi:10.1021/la00017a029.
[180] J.P. Hurvois, C. Moinet, Reactivity of ferrocenium cations with molecular oxygen in polar organic solvents: Decomposition, redox reactions and stabilization, J. Organomet. Chem. 690 (2005) 1829–1839. doi:10.1016/j.jorganchem.2005.02.009.
[181] A. Paul, R. Borrelli, H. Bouyanfif, S. Gottis, F. Sauvage, Tunable Redox Potential, Optical Properties, and Enhanced Stability of Modified Ferrocene-Based Complexes, ACS Omega. 4 (2019) 14780–14789. doi:10.1021/acsomega.9b01341.

[182] L.L. Norman, A. Badia, Redox Actuation of a Microcantilever Driven by a Self-Assembled Ferrocenylundecanethiolate Monolayer: An Investigation of the Origin of the Micromechanical Motion and Surface Stress, J. Am. Chem. Soc. 131 (2009) 2328–2337. doi:10.1021/ja808400s.
[183] E.R. Dionne, V. Toader, A. Badia, Microcantilevers Bend to the Pressure of Clustered Redox Centers, Langmuir. 30 (2014) 742–752. doi:10.1021/la403551c.
[184] A.S. Viana, A.H. Jones, L.M. Abrantes, M. Kalaji, Redox induced orientational changes in a series of short chain ferrocenyl alkyl thiols self-assembled on gold(111) electrodes, J. Electroanal. Chem. 500 (2001) 290–298. doi:10.1016/S0022-0728(00)00422-8.
[185] S. Ye, Y. Sato, K. Uosaki, Redox-Induced Orientation Change of a Self-Assembled Monolayer of 11-Ferrocenyl-1-undecanethiol on a Gold Electrode Studied by in Situ FT-IRRAS, Langmuir. 13 (1997) 3157–3161. doi:10.1021/la9700432.
[186] M.T. Cruanes, H.G. Drickamer, L.R. Faulkner, Characterization of Charge Transfer Processes in Self-Assembled Monolayers by High-Pressure Electrochemical Techniques, Langmuir. 11 (1995) 4089–4097. doi:10.1021/la00010a074.
[187] E.R. Dionne, T. Sultana, L.L. Norman, V. Toader, A. Badia, Redox-Induced Ion Pairing of Anionic Surfactants with Ferrocene-Terminated Self-Assembled Monolayers: Faradaic Electrochemistry and Surfactant Aggregation at the Monolayer/Liquid Interface, J. Am. Chem. Soc. 135 (2013) 17457–17468. doi:10.1021/ja408512q.
[188] R.L. Wolfe, R. Balasubramanian, J.B. Tracy, R.W. Murray, Fully Ferrocenated Hexanethiolate Monolayer-Protected Gold Clusters, Langmuir. 23 (2007) 2247–2254. doi:10.1021/la0624081.
[189] R.L. Stiles, R. Balasubramanian, S.W. Feldberg, R.W. Murray, Anion-Induced Adsorption of Ferrocenated Nanoparticles, J. Am. Chem. Soc. 130 (2008) 1856–1865. doi:10.1021/ja074161f.
[190] R. Sardar, C.A. Beasley, R.W. Murray, Ferrocenated Au Nanoparticle Monolayer Adsorption on Self-Assembled Monolayer-Coated Electrodes, Anal. Chem. 81 (2009) 6960–6965. doi:10.1021/ac9010364.
[191] C.A. Beasley, R.W. Murray, Voltammetry and Redox Charge Storage Capacity of Ferrocene-Functionalized Silica Nanoparticles, Langmuir. 25 (2009) 10370–10375. doi:10.1021/la901050t.
[192] J. Wilcockson, The use of sodium perchlorate in deproteinization during the preparation of nucleic acids, Biochem. J. 135 (1973) 559–561. doi:10.1042/bj1350559.
[193] C.D. Bain, J. Evall, G.M. Whitesides, Formation of monolayers by the coadsorption of thiols on gold: Variation in the head group, tail group, and solvent, J. Am. Chem. Soc. 111 (1989) 7155–7164. doi:10.1021/ja00200a039.
[194] K. Hu, Z. Chai, J.K. Whitesell, A.J. Bard, In situ monitoring of diffuse double layer structure changes of electrochemically addressable self-assembled monolayers with an atomic force microscope, Langmuir. 15 (1999) 3343–3347. doi:10.1021/la9813937.
[195] J. Redepenning, J.M. Flood, Influence of electrolyte activity on formal potentials measured for ferrocenylhexanethiol monolayers on gold: Indistinguishable responses in aqueous solutions of HClO4 and NaClO4, Langmuir. 12 (1996) 508–512. doi:10.1021/la950715t.
[196] M.W.J. Beulen, F.C.J.M. van Veggel, D.N. Reinhoudt, Coupling of acid–base and redox

functions in mixed sulfide monolayers on gold, Chem. Commun. (1999) 503–504. doi:10.1039/a809790i.
[197] M.N. Ates, C.J. Allen, S. Mukerjee, K.M. Abraham, Electronic Effects of Substituents on Redox Shuttles for Overcharge Protection of Li-ion Batteries, J. Electrochem. Soc. 159 (2012) A1057–A1064. doi:10.1149/2.064207jes.
[198] S.M. Batterjee, M.I. Marzouk, M.E. Aazab, M.A. El-Hashash, The electrochemistry of some ferrocene derivatives: Redox potential and substituent effects, Appl. Organomet. Chem. 17 (2003) 291–297. doi:10.1002/aoc.414.
[199] T.Y. Yeo, J.S. Choi, B.K. Lee, B.S. Kim, H.I. Yoon, H.Y. Lee, Y.W. Cho, Electrochemical endotoxin sensors based on TLR4/MD-2 complexes immobilized on gold electrodes, Biosens. Bioelectron. 28 (2011) 139–145. doi:10.1016/j.bios.2011.07.010.
[200] L. Ma, N. Sun, Y. Meng, C. Tu, X. Cao, Y. Wei, L. Chu, A. Diao, Harnessing the affinity of magnetic nanoparticles toward dye-labeled DNA and developing it as an universal aptasensor revealed by lipopolysaccharide detection, Anal. Chim. Acta. 1036 (2018) 107–114. doi:10.1016/j.aca.2018.06.060.
[201] C.M. Crudden, J.H. Horton, I.I. Ebralidze, O. V Zenkina, A.B. Mclean, B. Drevniok, Z. She, H. Kraatz, N.J. Mosey, T. Seki, E.C. Keske, J.D. Leake, A. Rousina-webb, G. Wu, Ultra stable self-assembled monolayers of N-heterocyclic carbenes on gold, 6 (2014). doi:10.1038/nchem.1891.
[202] S.-W. Tam-Chang, H.A. Biebuyck, G.M. Whitesides, N. Jeon, R.G. Nuzzo, Self-Assembled Monolayers on Gold Generated from Alkanethiols with the Structure RNHCOCH2SH, Langmuir. 11 (1995) 4371–4382. doi:10.1021/la00011a033.
[203] A. Heller, B. Feldman, Electrochemical glucose sensors and their applications in diabetes management, Chem. Rev. 108 (2008) 2482–2505. doi:10.1021/cr068069y.
[204] C.L. Krüger, M.-T. Zeuner, G.S. Cottrell, D. Widera, M. Heilemann, Quantitative single-molecule imaging of TLR4 reveals ligand-specific receptor dimerization., Sci. Signal. 10 (2017) eaan1308. doi:10.1126/scisignal.aan1308.
[205] M. Hirschfeld, J.J. Weis, V. Toshchakov, C. a Salkowski, M.J. Cody, D.C. Ward, N. Qureshi, S.M. Michalek, S.N. Vogel, Signaling by toll-like receptor 2 and 4 agonists results in differential gene expression in murine macrophages., Infect. Immun. 69 (2001) 1477–82. doi:10.1128/IAI.69.3.1477-1482.2001.
[206] S.M. Opal, Endotoxins and Other Sepsis Triggers, in: Endotoxemia Endotoxin Shock, KARGER, Basel, 2010: pp. 14–24. doi:10.1159/000315915.
[207] M. Jerabek-Willemsen, T. André, R. Wanner, H.M. Roth, S. Duhr, P. Baaske, D. Breitsprecher, MicroScale Thermophoresis: Interaction analysis and beyond, J. Mol. Struct. 1077 (2014) 101–113. doi:10.1016/j.molstruc.2014.03.009.
[208] M. Jerabek-Willemsen, C.J. Wienken, D. Braun, P. Baaske, S. Duhr, Molecular Interaction Studies Using Microscale Thermophoresis, Assay Drug Dev. Technol. 9 (2011) 342–353. doi:10.1089/adt.2011.0380.

Appendix: Efforts to Determine the Biophysical Interactions between Toll-like Receptor 4/Myeloid Differentiation Factor 2 and Lipopolysaccharides

MicroScale Thermophoresis (MST) was used in the present work in an effort to determine the physical interactions between the immunoprotein (TLR4) and its respective ligand (LPS), with the ultimate goal being to better understand our sensor response and to potentially increase the sensitivity of the sensor so that drift would be less of a problem. This is accomplished by quantifying the dissociation constant (K_d) of the complex-formation reaction, as shown in Reaction A1.1 and Equation A1.1 [207].

The experimental work was accomplished by incubating the fluorophore-tagged immunoprotein and its ligand in a glass capillary tube and then monitoring changes in the fluorescence intensity at a fixed location within the capillary tube. This change is due to a combination of changes in the photophysical properties of the dye and the diffusion of the biomolecule away from the point in the capillary tube where IR radiation is applied (for purposes of a generating temperature gradient of 2-6 K that induces diffusion of the immunoprotein) for up to a few seconds. This elevated temperature causes a depletion of solvated immunoproteins due to a phenomenon referred to as thermal diffusion or thermophoresis [208], with the diffusion coefficient being related to the complex-solvent interface [208]. It is expected that the complex-solvent interfacial properties will change after the TLR4 immunoprotein binds to LPS.

$$\text{TLR4/MD-2} + \text{LPS} \rightarrow \text{TLR4/MD-2/LPS} \qquad \text{Reaction A1.1}$$

$$K_d = \frac{[TLR4/MD-2][LPS]}{[TLR4/MD-2/LPS]}$$ Equation A1.1

The Thermophoresis instrument measures two variables. The first variable is the fluorescence emission intensity measured prior to IR-laser irradiation. The second variables in the change in fluorescence intensity measured after 20 s of IR-laser irradiation, which is referred to as F_{norm}. Within 1 s of irradiation, the normally observed decrease in emission intensity is attributed to photophysical properties (i.e., absorption, lifetime, quantum yield, etc.) of the fluorophore. The thermophoretic effect, which is dependent on multiple fundamental properties of the fluorophore-tagged biomolecule (i.e., hydration shell, size and surface charge), becomes dominant after ~1 s of irradiation [208].

In this work, 5 mM tris-Nitrilotriacetic acid (NTA) dye was used to label 10 nM of the Toll-like Receptor 4/Myeloid Differentiation Factor 2 (TLR4/MD-2) via its poly-Histidine Tag. The TLR4/MD-2 binding interaction with Lipopolysaccharide (LPS) was observed by performing a titration experiment using capillary tubes containing LPS concentrations from 5.9 nM to 0.2 mM. Control experiments were performed identically but in the absence of TLR4/MD-2. These samples were incubated with LPS for 60 min prior to collecting the data.

Figure A.1a and b show the increase in fluorescence emission intensity and decrease in F_{norm} observed for both sets of samples (i.e., samples containing fluorophore-tagged TLR4/MD-2 and samples containing just the fluorophore) as a function of increasing LPS concentration. In the both the case of fluorescence emission intensity and F_{norm}, Δ values of 0 is assigned to the sample containing the smallest concentration of LPS. The specific cause of these trends remains elusive,

but they were attributed to both the changes in the photophysical properties of the dye and thermal diffusion of the fluorophore correlating with greater LPS concentrations. Samples containing fluorophore-tagged TLR4/MD-2 display a greater magnitude of change (in both Δ emission intensity and ΔF_{norm}) than seen in the control experiments (i.e., in the absence of TLR4/MD-2) for reasons that are also not fully known yet.

Dissociation constants obtained from these experiments are displayed in Table A.1, showing that the values for the interaction between dye and LPS is lower than that of fluorophore-tagged TLR4/MD-2 and LPS, indicating that the former binding affinity is stronger than the latter. These data do suggest that TLR4/MD-2 does bind to LPS, as expected. Similar experiments were performed for incubation times from 0 min to 24 h and at temperatures from 25 to 44 ^{o}C, also showing that the dye binds to LPS with a similar or greater binding affinity.

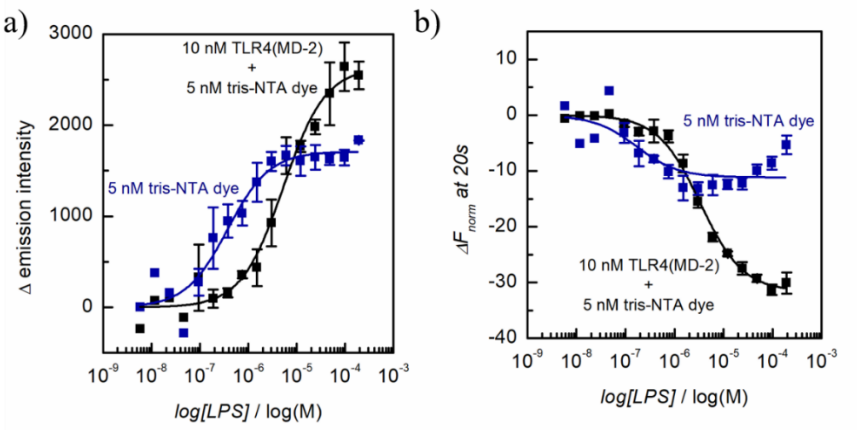

Figure A.1: (a) Emission intensity and (b) changes in emission intensity after 20 s IR-Laser irradiation gathered from three independent experiments and the sigmoidal curve fit of the fluorophore-tagged TLR4/MD-2 (black) and fluorophore (blue) interaction with LPS. Measurements were collected after 1 h incubation of LPS with either 10 nM TLR4/MD-2 and 5 nM dye or 5 nM dye at T = 25 ^{o}C.

The implication of these preliminary results is that the fluorophore dye selected for this work (red-tris NTA dye) is binding to LPS with a slightly higher affinity than to TLR4/MD-2, at

least under the conditions of this work, thus making the results obtained difficult to interpret. Specifically, the MST data suggest that the $K_{d,}$ of the TLR4/MD-2 binding interaction with LPS is five orders of magnitude higher than the one reported in the literature (i.e., the binding affinity calculated from our MST experiments are significantly lower than reported in the literature) [55], which seems unlikely. Thus, in future work, an alternative dye should be employed.

Table A.1: Dissociation constants obtained from sigmoidal curve fits of the data shown in Figure A.1. Experimental conditions are given in the figure caption.

	K_d obtained from fitting ΔF_{norm} at 20 s data / µM	K_d obtained from fitting Δ emission intensity data / µM
10 nM TLR4/MD-2 + 5 nM dye	3.38 ± 0.32	5.27 ± 0.99
5 nM dye	0.16 ± 0.16	0.37 ± 0.12